Stony Brook University

Computational Conformal Geometry and it's Applications

A Dissertation presented

by

Rui Shi

to

The Graduate School

in Partial Fulfillment of the

Requirements

for the Degree of

Doctor of Philosophy

in

Computer Science

Stony Brook University

December 2014

Stony Brook University

The Graduate School

Rui Shi

We, the dissertation committe for the above candidate for the

Doctor of Philosophy degree, hereby recommend

acceptance of this dissertation

Xianfeng Gu - Dissertation Advisor
Associate Professor, Computer Science Department

Jie Gao - Chairperson of Defense
Associate Professor, Computer Science Department

Jing Chen
Assistant Professor, Computer Science Department

Feng Luo - Out Member
Professor, Department of Mathematics, Rutgers University

This dissertation is accepted by the Graduate School

Charles Taber
Dean of the Graduate School

Abstract of the Dissertation

Computational Conformal Geometry and it's Applications

by

Rui Shi

Doctor of Philosophy

in

Computer Science

Stony Brook University

2014

Abstract

Conformal geometry has deep roots in pure mathematics, combining complex analysis, Riemann surface theory, algebraic geometry, differential geometry and algebraic topology. Computational conformal geometry plays an important role in digital geometry processing. Recently, theory of discrete conformal geometry and algorithms of computational conformal geometry have been developed[50]. A series of practical algorithms are presented to compute conformal mapping, which has been broadly applied in a lot of practical fields, including computer graphics, medical imaging, wireless sensor networks, visualization, and so on. In this thesis proposal, we address three applications of computational conformal geometry in medical imaging, wireless sensor networks and computer graphics respectively.

Firstly, automatic computation of surface correspondence via harmonicmap is an active research field in computer vision. It may help document and understand physical and biological phenomena and also has broad applications in biometrics, medical imaging and motion capture. Although numerous studies have been devoted to harmonic map research, limited progress has been made to compute a diffeomorphic harmonic map on general topology surfaces with landmark constraints. This work conquer this problem by changing the Riemannian metric on the target surface to a hyperbolic metric, so that the harmonic mapping is guaranteed to be a diffeomorphism under landmark constraints. The computational algorithms are based on the Ricci flow and nonlinear heat diffusion methods. The approach is general and robust. We apply our algorithm to study constrained surface registration problem which applied

to both medical and computer vision applications. Experimental results demonstrate that, by changing the Riemannian metric, the registrations are always diffeomorphic, and achieve relative high performance when evaluated with some popular surface registration evaluation standards.

Secondly, in a wireless sensor network, random walk on a graph is a Markov chain and thus is memoryless as the next node to visit depends only on the current node and not on the sequence of events that preceded it. With these properties, random walk and its many variations have been used in network routing to randomize the traffic pattern and hide the location of the data sources. We show a myth in common understanding of the memoryless property of a random walk applied for protecting source location privacy in a wireless sensor network. In particular, if one monitors only the network boundary and records the first boundary node hit by a random walk, this distribution can be related to the location of the source node. For the scenario of a single data source, a very simple algorithm which integrates along the network boundary would reveal the location of the source. We also develop a generic algorithm to reconstruct the source locations for various sources that have simple descriptions (e.g., k source locations, sources on a line segment, sources in a disk). This represents a new type of traffic analysis attack for invading sensor data location privacy and essentially re-opens the problem for further examination.

Finally, in medical imaging, we propose a new colon flattening algorithm that is efficient, shape-preserving, and robust to topological noise. Unlike previous approaches, which require a mandatory topological denoising to remove fake handles, our algorithm directly flattens the colon surface without any denoising. In our method, we replace the original Euclidean metric of the colon surface with a heat diffusion metric that is insensitive to topological noise. Using this heat diffusion metric, we then solve a Laplacian equation followed by an integration step to compute the final flattening. We demonstrate that our method is shape-preserving and the shape of the polyps are well preserved. The flattened colon also provides an efficient way to enhance the navigation and inspection in virtual colonoscopy. We further show how the existing colon registration pipeline is made more robust by using our colon flattening. We have tested our method on several colon wall surfaces and the experimental results demonstrate the robustness and the efficiency of our method.

To my parents, as well as all that helped and cared about me.

Contents

List of Figures

Acknowledgements

I'd like to thank my parents for their support and suffer of missing. I'd like to thank my advisor professor Xianfeng Gu, for his patience advising, precious help on both academy and personal life. I learned a lot of great ideas as well as wisdoms about life. A young PhD need a great advisor to get mature, and I'm lucky enough to get one. I'd like to thank professor Jie Gao, for her generous help and guide to her research field; I'd like to thank professor Yalin Wang, for his kindly help on the collaboration works; I'd like to thank professor Wei Zeng for her advising and help on my early years of research; I'd like to thank all of my labmates for their accompany; I'd like to thank all my lovely friends for their help, spiritually and materially. I could not make it without you.

Publications

Published:

- Rui Shi, Wei Zeng, Zhengyu Su, Hanna Damasio, Zhonglin Lu, Yalin Wang, Shing-Tung Yau, Xianfeng Gu: Hyperbolic Harmonic Mapping for Constrained Brain Surface Registration. *CVPR 2013: 2531-2538*

- Rui Shi, Mayank Goswami, Jie Gao, Xianfeng Gu: Is random walk truly memoryless - Traffic analysis and source location privacy under random walks. *INFOCOM 2013: 3021-3029*

- Rui Shi, Wei Zeng, Zhengyu Su, Yalin Wang, Hanna Damasio, Zhonglin Lu, Shing-Tung Yau, Xianfeng Gu: Hyperbolic Harmonic Brain Surface Registration with Curvature-Based Landmark Matching. *IPMI 2013: 159-170*

- Rui Shi, Wei Zeng, Jerome Zhengrong Liang, Xianfeng David Gu: Efficient Topological Cleaning for Visual Colon Surface Flattening. *Abdominal Imaging 2012: 20-29*

- Rui Shi; Hongbin Zhu; Gu, D.X.; Liang, J.Z.: Efficient colon wall flattening by improved conformal mapping methodologies for computed tomography colonography, *NSS/MIC 2011 IEEE*

- Wei Zeng, Rui Shi, Yalin Wang, Shing-Tung Yau, Xianfeng Gu: Teichmller Shape Descriptor and Its Application to Alzheimer's Disease Study. *International Journal of Computer Vision 105(2): 155-170 (2013)*

- Krishna Chaitanya Gurijala, Rui Shi, Wei Zeng, Xianfeng Gu, Arie E. Kaufman: Colon Flattening Using Heat Diffusion Riemannian Metric. *IEEE Trans. Vis. Comput. Graph. 19(12): 2848-2857 (2013)*

- Zhengyu Su, Wei Zeng, Rui Shi, Yalin Wang, Jian Sun, Xianfeng Gu: Area Preserving Brain Mapping. *CVPR 2013: 2235-2242*

- Mingchen Gao, Rui Shi, Shaoting Zhang, Wei Zeng, Zhen Qian, Xianfeng David Gu, Dimitris N. Metaxas, Leon Axel: High resolution cardiac shape registration using Ricci flow. *ISBI 2013: 488-491*

- Hao Peng, Rui Shi, Shi-Qing Xin, Xianfeng Gu: Global Colon Geometric Structure Analysis Based on Geodesics and Conformal Flattening. *Abdominal Imaging 2013: 107-116*

- Huafeng Wang, Lihong Li, Hao Han, Rui Shi, Bowen Song, Hao Peng, Yan Liu, Xianfeng Gu, Yunhong Wang, Zhengrong Liang: A 2.5D Colon Wall Flattening Model for CT-Based Virtual Colonoscopy. *MLMI 2013: 203-210*

- Wei Zeng, Rui Shi, Xianfeng David Gu: Global Surface Remeshing Using Symmetric Delaunay Triangulation in Uniformization Spaces. *ISVD 2011: 160-169*

Submitted:

- Shi, Rui; Zeng, Wei; Su, Zhengyu; Damasio, Hanna; Lu, Zhonglin; Wang, Yalin; Yau, Shing-Tung; Gu, Xianfeng: Hyperbolic Harmonic Mapping for Surface Registration. *Submitted to IEEE TPAMI*

- Su, Zhengyu; Wang, Yalin; Shi, Rui; Zeng, Wei; Sun, Jian; Luo, Feng; Gu, Xianfeng: Optimal Mass Transport for Shape Analysis. *Submitted to IEEE TPAMI*

1 Introduction

Computational conformal geometry [50] is an emerging inter-disciplinary field, which applies algebraic topology, differential geometry [32] and Riemann surface theories [34] in many engineering fields such as geometric modeling [44][56], computer graphics [109], computer vision [152], medical imaging[1], wireless sensor networks [112], visualization [77], scientific computation and many other engineering fields.

Recently, with the rapid development of three dimensional digital scanning technology, computer aided geometric design, bio-informatics and medical imaging, the needs for effective methods for digital geometric processing become urgent.

The fundamental reason for conformal geometry to be so useful lies in the following facts: Conformal geometry studies the conformal structure. All surfaces in daily life have a natural conformal structure. Therefore, the conformal geometric algorithms are very general. Conformal structure of a general surface is more flexible than Riemannian metric structure and more rigid than topological structure. It can handles large deformations, which Riemannian geometry can not efficiently handle; it preserves a lot of geometric information during the deformation, whereas, topological methods lose too much information. Conformal maps are easy to control. For example, the conformal maps between two simply connected closed surfaces form a six dimensional space, therefore by fixing three points, the mapping is uniquely determined. This fact makes conformal geometric method very valuable for surface matching and comparison. Computational conformal geometry builds a connection between pure mathematics and computational algorithms, and gives a solution to the problem of mapping 3D surfaces to 2D ones, and minimizing the distortion during the process. Computational conformal geometry also studies the relationship between curvature and metric, which gives us insights about the conformal structure and shape space of surfaces, and enables us to design metrics to satisfy specific requirements. In such a way, applications of computational conformal geometry are extended to the fields related to metric design.

In this proposal, we first review the mathematical background of computational conformal geometry in Section 2. Then in Section 3, we explain in details the computational algorithms. In section 4, we introduce the application in computer vision: Hyperbolic Harmonic Surface Registration. In section 5, applications in wireless sensor network: Traffic Analysis and Source Location Privacy under Random Walks. In section 6, applications in medical imaging: Colon Flattening Using Heat Diffusion Riemannian Metric. Finally we conclude the proposal with a sketch of the future plan.

2 Theoretical Background

Many applications require to process and map a 3D surface to a planar domain. Generally speaking, such mapping will have distortions, since the geometric structures of a 3D surface and the plane usually have some differences. There are many metrics to measure the distortion of a mapping between two surfaces. These two are essential and important: angle distortion and area distortion. A mapping which preserves both angle and area between two surfaces preserves the Gaussian curvature [76], and is called a isometric mapping. Conformal mapping, or angle preserving mapping, is the one that minimizes angle distortion. It has many good properties and can be applied in many research and engineering areas.

Conformal geometry studies the conformal structure of general surfaces, and computational conformal geometry aims at using computational algorithms to calculate the conformal structure, and the conformal mapping between surfaces. In order to understand those algorithms, we first introduce many mathematical definitions and theorems, and study elementary algebraic topology, differential geometry, and Riemann surface theories. In this section, we will briefly review the mathematical background of conformal geometry, which includes algebraic topology, differential geometry, Riemann Surface theory and surface Ricci flow theory.

2.1 Algebraic Topology

Algebraic topology uses algebraic methods to study topological problems. Basically, special groups are associated with a space, and the topological properties of the space are reflected by the structures of the groups. A fundamental problem in topology is to determine whether two spaces are topologically equivalent. That is, we wish to know if one space can be morphed into the other without having to puncture it. The key idea of homology and cohomology is to define invariants (i.e., quantities that cannot change by continuous deformation) that characterize topological spaces. That is to say, they are tools of defining proper *equivalence classes*. It is extremely difficult to find the invariants for homeomorphism, but we are able to find other weaker ones, such as homotopy, homology and cohomology groups. Compared to homopoty groups, homology and cohomology groups contain less information, but are much easier to compute since they are abelian.

2.1.1 Homology Groups

In this part, we review the concept of simplicial complex, chain group and homology group.

Definition 2.1 (Simplex)**.** *Suppose $k+1$ points $\{v_0, v_1, \cdots, v_k\}$ are in general positions in $\mathbb{R}^n, n \geq k+1$, the standard simplex $[v_0, v_1, \cdots, v_k]$ is the minimal convex set including all of them,*

$$\sigma = [v_0, v_1, \cdots, v_k] = \{x \in \mathbb{R}^n | x = \sum_{i=0}^{k} \lambda_i v_i, \sum_{i=0}^{k} \lambda_i = 1, \lambda_i \geq 0\},$$

we call $v_0, v_1, \cdots, v_k$ are the vertices of the simplex σ. Suppose $\tau \subset \sigma$ is also a simplex, then we say τ is a facet of σ.

Definition 2.2 (Simplicial Complex)**.** *A simplicial conplex Σ is a union of simplices, such that*

1. *If a simplex σ belongs to K, then all its facets also belong to Σ.*
2. *If $\sigma_1, \sigma_2 \subset K, \sigma_1 \cap \sigma_2 \neq \emptyset$, then the intersection of σ_1 and σ_2 is also a common face.*

Definition 2.3 (Chain Group)**.** *A q-chain is a linear combination of all q-simplexes in M,*

$$\sum_i \lambda_i \sigma_i, \lambda_i \in \mathbb{Z}.$$

The set $C_q(M)$ of q-chains in M forms an abelian group with addition defined by

$$\sum \alpha_j \sigma_j + \sum \beta_j \sigma_j = \sum (\alpha_j + \beta_j)\sigma_j.$$

The zero element is $\sum 0\sigma_j$ and the inverse of $\sum \alpha_j \sigma_j$ is $\sum(-\alpha_j)\sigma_j$. $C_q(M)$ is called the q-demensional chain group of M.

Definition 2.4 (Boundary Operator)**.** *The q-dimensional boundary operator is a homomorphism,*

$$\partial_q : C_q \to C_{q-1},$$

such that

$$\partial_q[v_0, v_1, \cdots, v_q] = \sum_i (-1)^i [v_0, v_1, \cdots, v_{i-1}, v_{i+1}, \cdots, v_q],$$

and

$$\partial_q \sum_i \alpha_i \sigma_i = \sum_i \alpha_i \partial_q \sigma_i, \alpha_i \in \mathbb{Z}.$$

The central idea of homology is to study the difference between the closed curves and the boundary curves. A *cycle* is simply a closed k-chain, *i.e.*, a linear combination of k-simplices so that the boundary of this chain is the empty set. Any set of vertices is a closed chain; also are any set of one dimensional loops. Equivalently, a k-cycle is any k-chain that belongs to $\ker \partial k$, by definition.

With the concept of k-cycle, we can define equivalence classes in homology. We will say that a k-cycle is homologous to another k-cycle (i.e., in the same equivalence class as the other) when these two chains differ by a boundary of a $(k+1)$-chain (i.e., by an exact chain). By definition, this exact chain is the image of ∂_{k+1}, i.e., $\operatorname{img} \partial_{k+1}$.

Definition 2.5 (Homology Groups)**.** *The homology groups $\{H_k\}_{k=0..n}$ of a chain complex based on ∂ are defined as the following quotient spaces:*

$$H_k = \frac{\ker \partial_k}{\operatorname{img} \partial_{k+1}}.$$

Here $\ker \partial_k$ is the k-dimensional closed chain group and $\operatorname{img} \partial_{k+1}$ is the k-dimensional boundary group.

For surfaces S, the group bases of $H_1(S)$ are all the closed loops that cannot shrink to a point without leaving the surface. In Figure 1, the homology group bases are $\{a_1, b_1, a_2, b_2\}$.

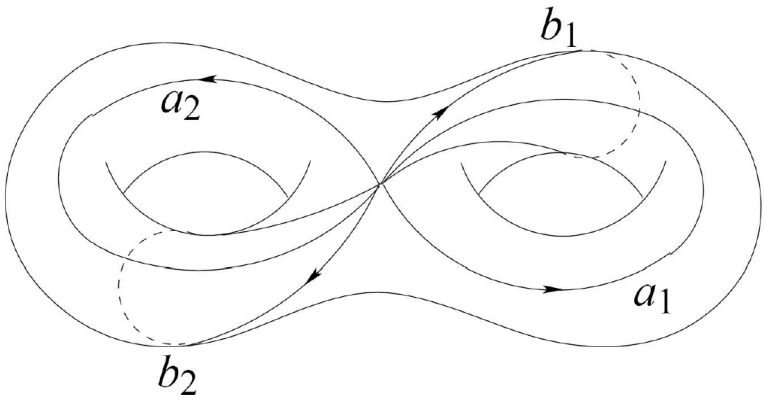

Figure 1: Homology group bases of a genus-2 surface.

Two k-chains c_k^1, c_k^2 are homologous if they bound a $(k+1)$-chain c_{k+1},

$$c_k^1 - c_k^2 = \partial_{k+1} c_{k+1}.$$

2.1.2 Cohomology Groups

Homology is more geometric and easier to be visualized or imaged, while cohomology is more analytic and easier to compute and manipulate. There are many kinds of cohomology, e.g., singular cohomology, de Rham cohomology, Čech cohomology, etc [55]. All of them are the dual of homology in some way. Among them, de Rham cohomology is most widely used. The de Rham cohomology groups are defined by taking the formal definition in the homology, replacing all occurrences of chain by cochain, of ∂ by d, and reverse the direction of the operator between spaces – this will also define equivalence classes. Here d is the exterior differentiation operator which will be explained later in Section 2.2.1.

Definition 2.6 (de Rham Cohomology Group)**.** *Suppose M is a differential manifold. The m-th de Rham cohomology is defined as*

$$H^m(M) = \frac{\ker d^m}{\operatorname{img} d^{m-1}}.$$

From Theorem 2.9, we know $H^m(M)$ is the dual space of $H_m(M)$.

2.1.3 Surface Topological Classification

Surface classification is the first step in calculating conformal structure, because different algorithms apply to different topologies as stated in Section 3. Topology considers the global properties of a space. We can imagine the surface is made of rubber. We can stretch, compress but not tear the surface, and consider those preserved properties. Based on homology and cohomology, we could classify the surfaces by their topologies.

Orientability: Intuitively, if a closed surface is embedded in $\mathbb{R}^3$, then it separates $\mathbb{R}^3$ into two parts. One is finite, called the interior; the other is infinite, called the exterior. We say a surface is *orientable*, if we can differentiate its inside from its outside. The most common non-orientable surface is the Möbius band, which is formed by joining the ends of a rectangle with a twist (see Figure 2). Orientablility is an important topological property. General surfaces are the boundary of volumes; therefore it naturally has two sides, inside and outside. In the rest of the report, we mainly study the orientable surfaces embedded in $\mathbb{R}^3$, and assume all the surfaces are of this kind.

Genus: The *genus* of a connected, orientable surface is an integer representing the maximum number of cuttings along closed simple curves without rendering the resultant manifold disconnected. It is equal to the number of handles on it, which is the major topological invariant, and can be retrieved by calculating the homology group bases.

Boundary: Surfaces without boundaries are closed, which a surface with boundaries is called an open surface. The number of boundaries is also a topological invariant.

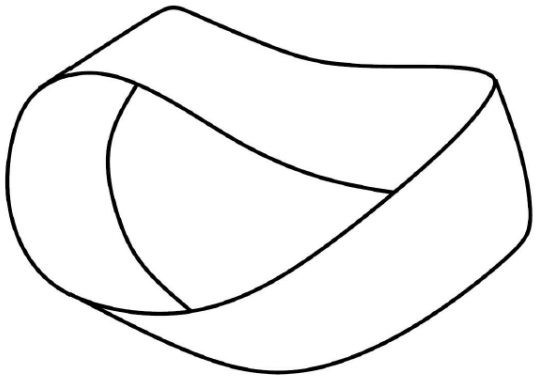

Figure 2: A Möbius band is a non-orientable surface with one boundary

Simple surfaces can be glued together to form a more complicated one. Basically, we can remove a small topological disk from each surface, and glue the two left pieces along their boundaries of the removed disks.

Definition 2.7 (Connected Sum)**.** *The connected sum $S_1 \# S_2$ is formed by deleting the interior of disks $D_i \subset S_i$ and attaching the resulting punctured surfaces $S_i - D_i$ to each other by a homeomorphism*

$$h : \partial D_1 \to \partial D_2,$$

where ∂D_i represents the boundary of D_i, so

$$S_1 \# S_2 = (S_1 - D_1) \cup_h (S_2 - D_2).$$

All surfaces can be decomposed to the connected sum of simple surfaces. The building blocks are *tori* for orientable surfaces, and the *crosscaps* for unorientable surfaces.

Theorem 2.8 (Classification Theorem for Surfaces)**.** *Any closed connected surface is homeomorphic to exactly one of the following surfaces: a sphere, a finite connected sum of tori, or a sphere with a finite number of disjoint discs removed and with crosscaps glued in their place. The sphere and connected sums of tori are orientable surfaces, whereas surfaces with crosscaps are unorientable.*

2.2 Differential Geometry

Differential geometry is a mathematical discipline that uses the methods of differential and integral calculus, as well as linear and multilinear algebra, to study problems in geometry [33]. The theory of plane and space curves of surfaces in the three-dimensional Euclidean space formed the basis for its initial development in the eighteenth and nineteenth century. Since the late nineteenth century, differential geometry has grown into a field concerned more generally with geometric structures on differentiable manifolds. In this introduction, we focus on Stokes Theorem, Hodge Theorem and Gauss-Bonnet Theorem.

2.2.1 Differential Forms

Differential forms are the first essential concept in differential geometry. There are many ways to define differential forms and their integration on manifolds. We may refer to [122] for a detailed introduction. Briefly speaking, a *differential form* of degree k, or (differential) k-form, on a smooth manifold M is a smooth section of the kth exterior power of the cotangent bundle of M. The set of all k-forms on M is a vector space commonly denoted $\Omega_k(M)$.

Differential forms of degree k are integrated over k dimensional chains. If $k = 0$, this is just evaluation of functions at points. Other values of $k = 1, 2, 3, \cdot$ correspond to line integrals, surface integrals, volume integrals etc.

Let

$$\omega = \sum a_{i_1,\ldots,i_k}(x)\, dx^{i_1} \wedge \cdots \wedge dx^{i_k}$$

be a differential form and S a differentiable k-manifold over which we wish to integrate, where S has the parameterization

$$S(u) = (x^1(u), \ldots, x^n(u))$$

for u in the parameter domain D. Then defines the integral of the differential form over S is defined [110] as

$$\int_S \omega = \int_D \sum a_{i_1,\ldots,i_k}(S(u)) \frac{\partial(x^{i_1}, \ldots, x^{i_k})}{\partial(u^1, \ldots, u^k)}\, du^1 \ldots du^k$$

where

$$\frac{\partial(x^{i_1}, \ldots, x^{i_k})}{\partial(u^1, \ldots, u^k)}$$

is the determinant of the Jacobian. The Jacobian exists because S is differentiable.

The fundamental relationship between the exterior derivative and integration is given by the following theorem.

Theorem 2.9 (Stokes Theorem)**.** *If ω is an $(n-1)$-form with compact support on M, and ∂M denotes the boundary of M with its induced orientation, then*

$$\int_M d\omega = \oint_{\partial M} \omega.$$

2.2.2 Hodge Theorem

Definition 2.10 (Hodge Star Operator)**.** *The Hodge star operator * is a linear map *: $\Omega^k(M) \to \Omega^{n-k}(M)$, defined as*

$$^*(dx_{i_1} \wedge dx_{i_2} \wedge dx_{i_k}) = (-1)^\sigma dx_{i_{k+1}} \wedge dx_{i_{k+2}} \wedge dx_{i_n}.$$

Here $\sigma = (i_1, i_2, \cdots, i_n)$ is a permutation of $(1, 2, \cdots, n)$.

Definition 2.11 (Codifferential Operator)**.** *The codifferential operator $\delta : \Omega^k(M) \to \Omega^{n-k}(M)$ is defined as*

$$\delta = (-1)^{k+1+k(n-k)*} d^*.$$

Definition 2.12 (Laplace Operator)**.** *The Lapalce operator $\Delta : \Omega^k(M) \to \Omega^k(M)$ is defined as*

$$\Delta = \delta d + d\delta.$$

If ω is a k-form, and $\Delta\omega = 0$, then ω is called a *k-harmonic form*. All of the k-harmonic forms form a group, defined as $H^k_\Delta(M)$.

Theorem 2.13 (Hodge Decomposition Theorem)**.**

$$\Omega^k(M) = E \oplus E^* \oplus H_\Delta.$$

Here $E = \{d\eta | \eta \in \Omega^{k-1}(M)\}$*, and* $E^* = \{{}^*d\eta | \eta \in \Omega^{k-1}(M)\}$

From Hodge theorem, we get each cohomologous class has a unique harmonic form as its representative.

2.2.3 First Fundamental Form

A *Riemannian metric* on a manifold M^n assigns, in a differentiable fashion, a positive definite inner product $\langle , \rangle$ in each tangent space M_p^n. A manifold with a Riemannian metric is called a Riemannian manifold.

In terms of coordinate basis $e_i = \partial_i := \partial/\partial x^i$, we then have the differentiable matrices (the "metric tensor")

$$g_{ij}(x) = \langle \frac{\partial}{\partial x^i}, \frac{\partial}{\partial x^j} \rangle.$$

Using the Riemannian metric we can define measures on the manifold. Suppose a regular surface S in R^3 is parameterized as $r(u, v)$.

Definition 2.14 (First Fundamental Form)**.** *The first fundamental form is defined as*

$$I = ds^2 = \langle dr, dr \rangle = \begin{pmatrix} du & dv \end{pmatrix} \begin{pmatrix} E(u,v) & F(u,v) \\ F(u,v) & G(u,v) \end{pmatrix} \begin{pmatrix} du \\ dv \end{pmatrix}$$

where

$$E = \langle r_u, r_u \rangle, F = \langle r_u, r_v \rangle, G = \langle r_v, r_v \rangle.$$

We often use symbol g to denote the inner product matrix of the first fundamental form. Therefore, we can also write

$$ds^2 \equiv \langle dr, dr \rangle_g = \sum g_{\alpha\beta} dx^\alpha dx^\beta.$$

Considering the parametric surface $n(u, v)$, we have

Definition 2.15 (Second fundamental Form)**.** *The second fundamental form is defined as*

$$II = -\langle dr, dn \rangle = \begin{pmatrix} du & dv \end{pmatrix} \begin{pmatrix} L(u,v) & M(u,v) \\ M(u,v) & N(u,v) \end{pmatrix} \begin{pmatrix} du \\ dv \end{pmatrix}$$

where

$$L = -\langle r_u, n_u \rangle, M = -\langle r_u, n_v \rangle = -\langle r_v, n_u \rangle, N = -\langle r_v, n_v \rangle.$$

Definition 2.16 (Gaussian Curvature)**.** *Gaussian curvature of a surface in* $\mathbb{R}^3$ *can be expressed as the ratio of the determinants of the second and first fundamental forms:*

$$K = \frac{\det II}{\det I} = \frac{LN - M^2}{EG - F^2}$$

Gauss's Theorema Egregium shows Gaussian curvature is intrinsic.

Theorem 2.17 (Gauss's Theorema Egregium)**.** *The Gaussian curvature is solely determined by the first fundamental form.*

The following theorem [24] is fundamental for calculating conformal mappings.

Theorem 2.18 (Isothermal Coordinates)**.** *For any point on the surface, there exists a neighborhood, which can be conformally mapped to a planar domain, namely, we can find* (u, v) *coordinates for a neighborhood of the surface, the first fundamental form is*

$$I = \lambda^2(u, v)(du^2 + dv^2)$$

The Gauss-Bonnet theorem or Gauss-Bonnet formula below in differential geometry is an important statement about surfaces which connects their geometry (in the sense of curvature) to their topology (in the sense of the Euler characteristic). It is named after Carl Friedrich Gauss who was aware of a version of the theorem but never published it, and Pierre Ossian Bonnet who published a special case in 1848 [23].

Theorem 2.19 (Gauss-Bonnet Theorem)**.** *For a compact oriented surface* M *with Riemannian metric* g*,*

$$\chi(M) = \frac{1}{2\pi} \int_M K d\mu,$$

where K *is the gaussian curvature of* g*,* $d\mu$ *is the area form with respect to* g*, and* $\chi(M)$ *is the Euler characteristic of* M*.*

The Euler characteristic of a closed orientable surface M can be calculated from its genus g as

$$\chi(M) = 2 - 2g$$

2.3 Conformal Structure and Riemann Surface

Based on the concepts and theorems of differential geometry, in this part, we introduce conformal structure and Riemann Surface theories, and uncover the relationship between holomorphic functions and conformal mappings.

2.3.1 Conformal Structure

Computational conformal geometry is a branch of computer science that studies the conformal structure of surfaces, and conformal mappings between them. It introduces deep and beautiful theory from pure continuous mathematics, and tries to find the discrete counterparts of them, which can be applied in designing computational conformal geometry algorithms. Here we introduce the basic concepts which are necessary in understanding the whole literature.

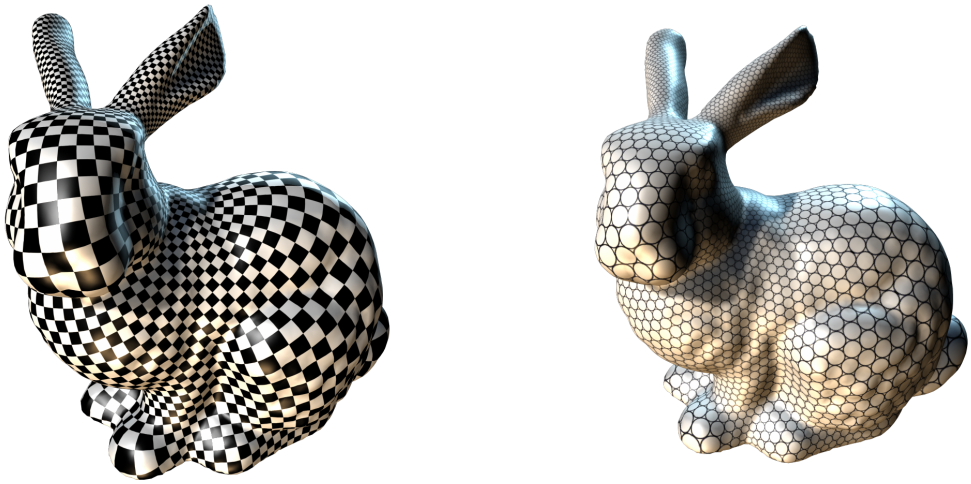

Figure 3: Conformal structure.

Definition 2.20 (Homeomorphism)**.** *Suppose M and N are two topological spaces. A continuous map $f : M \to N$ is called a homeomorphism between M and N, if f is invertible and $f^{-1} : N \to M$ is also continuous.*

Definition 2.21 (n-Manifold)**.** *A n-manifold is a topological space Σ covered by a set of open sets $\{U_\alpha\}$. For each U_α there is a homeomorphism $\phi_\alpha : U_\alpha \to \mathbb{R}^n$ that maps U_α to the Euclidean space $\mathbb{R}^n$. (U_α, ϕ_α) is called a local chart of Σ, the set of all charts $\{(U_\alpha, \phi_\alpha)\}$ form the atlas of Σ. Suppose $U_\alpha \cap U_\beta \neq \phi$, then $\phi_{\alpha\beta} = \phi_\beta \circ \phi_\alpha^{-1}$ is a transition map.*

Intuitively, a *manifold* is a topological space that is locally Euclidean (i.e., around every point, there is a neighborhood that is topologically the same as the open unit ball in $\mathbb{R}^n$). See Figure 4 for a 2-manifold example.

Definition 2.22 ((X, G) Atlas)**.** *Suppose X is a topological space, G is a transformation group of X. A manifold Σ with an atlas $\{(U_\alpha, \phi_\alpha)\}$ is an (X, G) atlas if $\phi_\alpha(U_\alpha) \subset X$ for all $\phi_\alpha(U_\alpha)$ and $\phi_{\alpha\beta} \in G$ for all $\phi_{\alpha\beta}$.*

One manifold may have infinite (X, G) atlases, therefore the equivalence (or compatibility) has to be defined among these atlases.

Definition 2.23 (Equivalent (X, G) Atlas)**.** . *Two (X, G) atlases of σ are equivalent if their union is still an (X, G) atlas of σ.*

A *geometric structure* could be defined as the union of all equivalent atlases.

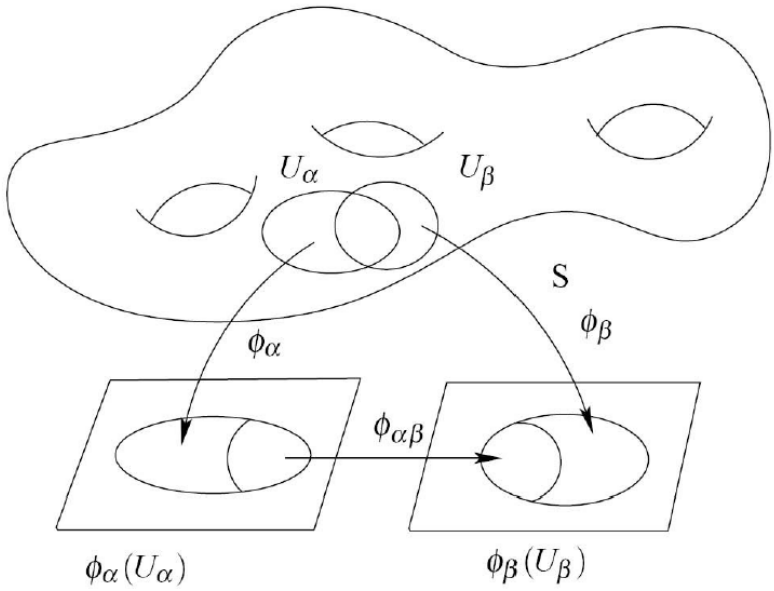

Figure 4: A 2-manifold

Definition 2.24 ((X, G) Structure)**.** *An (X, G) structure of a manifold σ is an equivalent class of its (X, G) atlas.*

Intuitively, X is the local image of each chart of Σ, and chart transition functions belong to group G.

Different domain X and different transformation group G will give us different geometric structure (X, G). Given a geometric structure (X, G), there are certain manifolds admitting such a structure.

Conformal structure is a special (X, G) structure where X is the complex plane $\mathbb{C}$ and G is the conformal mapping (i.e. holomorphic functions) group.

Given a 2-manifold M with an atlas (U_α, ϕ_α), if all chart transition functions

$$\phi_{\alpha\beta} : \phi_\alpha(U_\alpha \cap U_\beta) \to \phi_\beta(U_\alpha \cap U_\beta)$$

are conformal, then the atlas is called a *conformal atlas*, and M is called a *conformal manifold* (see Figure 4).

Two conformal atlases are equivalent if their union is still an conformal atlas. All the equivalent conformal atlases form a *conformal structure* of the manifold. According to Riemann surface theory [105] , all oriented surfaces have conformal structure, regardless of what topology the surface has.

In the literature of computer science community, there are fewer papers directly talking about constructing conformal structure than some closely relevant problems, namely *con-*

formal mappings and *conformal parameterizations*. A *conformal mapping* for 2-manifolds is a mapping from one 2-manifold M to another one M' such that it keeps the angle of intersection of every pair of intersecting arcs on M unchanged after the mapping. Conformal mappings are also called angle-preserving mappings. It can be defined more precisely in the following way:

Definition 2.25 (Conformal Mapping)**.** *A mapping from one 2-manifold M to another one M' is conformal if and only if it only scales the first fundamental form, i.e.,*

$$I' = \eta(u^1, u^2)I$$

where η is a non-zero scalar function which is called the conformal factor *and measures the area distortion, I and I' are the first fundamental form coefficient matrix for M and M' respectively.*

Given any two surfaces with similar topology it is possible to compute a one-to-one and onto mapping between them. The problem of computing such a mapping is referred to as *parameterization*. The image surface that the original surface is mapped to is typically referred to as the *parameter domain*. Usually, the parameter domain is the Euclidean plain. A *conformal parameterizations* of a 2-manifold is a special conformal mapping that maps (part of) the given 2-manifold M into the planar domain $\mathbb{R}^2$. We can see that a conformal structure requires any $\phi_{\alpha\beta}$ is conformal mapping (see Figure 4). On the other hand, conformal parameterizations using one-form methods also provide a way to construct conformal structure.

In the following subsections, we shall briefly review the theoretical base of conformal geometry. We will first introduce homology and cohomology, which are the core concepts of algebraic topology and the key to classify surfaces, or even higher dimensional manifolds. Then we will discuss surface differential geometry, including exterior differential calculus, harmonic forms, Hodge theorem, first fundamental form and Gauss-Bonnet theorem. These concepts and theorems are frequently used in describing computational conformal geometry algorithms. Based on differential geometry knowledge, we will explain complex analysis and Riemann surface theories. That will lead us to holomorphic one-forms, which play an essential role in one of the three categories of the algorithms to calculate conformal mappings. Finally, we will survey harmonic maps and surface curvature flow. These two techniques will give us the intuition of the other two categories of algorithms.

2.3.2 Holomorphic Functions

We can introduce the differential form in the complex domain as

$$dz = dx + idy$$

$$d\bar{z} = dx - idy$$

$$\frac{\partial}{\partial z} = \frac{1}{2}(\frac{\partial}{\partial x} - i\frac{\partial}{\partial y})$$
$$\frac{\partial}{\partial \overline{z}} = \frac{1}{2}(\frac{\partial}{\partial x} + i\frac{\partial}{\partial y})$$

Then we can define holomorphic functions.

Definition 2.26 (Holomorphic Function)**.** *A function $f : (x, y) \to (u, v)$ is holomorphic or complex analytic, if it satisfies the following Cauchy-Riemann equation:*

$$\begin{cases} \frac{\partial u}{\partial x} = \frac{\partial v}{\partial y} \\ \frac{\partial u}{\partial y} = -\frac{\partial v}{\partial x} \end{cases}$$

If $f = u + iv$ is holomorphic, then

$$\frac{\partial f}{\partial \overline{z}} = 0$$

Furthermore, it is easy to verify that both u and v are harmonic. We say that u and v are *conjugate* if $u + iv$ satisfies the Cauchy-Riemann equation. If a holomorphic function f is bijective and f^{-1} is holomorphic, then f is *biholomorphic*, or a *conformal mapping*. Therefore, conformal mappings between two planar domains can be represented as holomorphic functions.

Recall that an atlas is a collection of local charts $\{(U_\alpha, \phi_\alpha)\}$, the union of which cover the surface. An atlas is a *conformal atlas* if all its transition functions are biholomorphic. Two conformal atlases are equivalent if their union is still a conformal atlas. Each equivalence class of conformal atlases is called a *conformal structure* of the surface. A surface with a conformal structure is called a *Riemann surface*.

Definition 2.27 (Riemann Surface)**.** *A Riemann Surface represents a two dimensional manifold M with an atlas $\{(U_\alpha, z_\alpha)\}$, such that $\{(U_\alpha)\}$ is an open covering, $M \subset \cup U_\alpha$; $z_\alpha : U\alpha \to \mathbb{C}$ is a homeomorphism from an open set $U_\alpha \subset M$ to an open set on $\mathbb{C}$, $z_\alpha(U\alpha)$. If $U_\alpha \cap U_\beta \neq \emptyset$, then*

$$z_\beta \circ z_\alpha^{-1} : z_\alpha(U_\alpha \cap U_\beta) \to z_\beta(U_\alpha \cap U_\beta)$$

is biholomorphic, or a conformal mapping.

After defining the conformal mapping between two planar domains, we are ready to investigate and re-define the conformal mapping between two Riemann surfaces in a complex analysis way.

Definition 2.28 (Conformal Mapping)**.** *Suppose (S_1, A_1) and (S_2, A_2) are two Riemann surfaces, A_i's are their conformal structures. Suppose (U_α, ϕ_α) is a local chart of A_1, (V_β, ψ_β) is a local chart of A_2. $\phi : S_1 \to S_2$ is a conformal mapping if and only if*

$$\psi_\beta \circ \phi \circ \phi_\alpha^{-1} : \phi_\alpha(U_\alpha) \to \psi_\beta(V_\beta)$$

is biholomorphic.

As shown in Figure 5, let $\gamma_1, \gamma_2 : [0,1] \to S_1$ be two arbitrary curves on S_1, intersecting at the point p, the angle between the two tangent vectors $\frac{d\gamma_1}{dt}(p)$ and $\frac{d\gamma_2}{dt}(p)$ equal to θ. Therefore $\phi \circ \gamma_1(t)$ and $\phi \circ \gamma_2(t)$ are two curves on S_2, intersecting at $\phi(p)$. Then their intersection angle also equals to θ. A conformal mapping preserves angles.

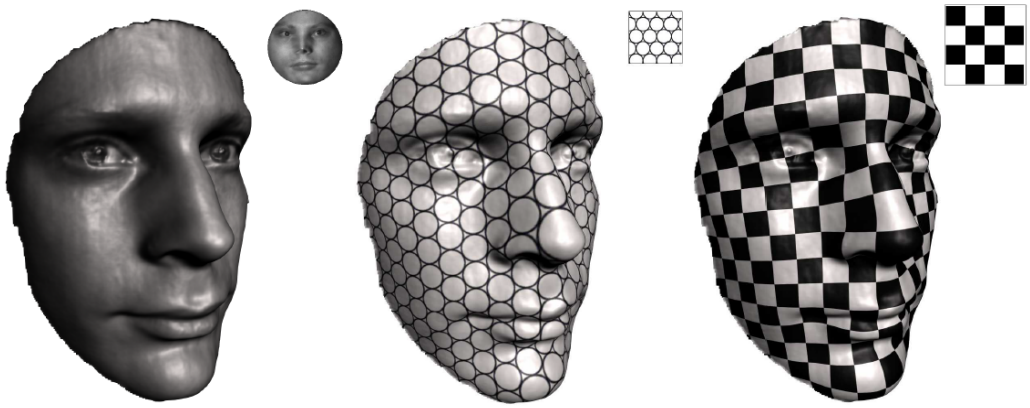

Figure 5: Conformal mappings preserve angles.

If a Riemann surface S has a Riemannian metric g, then we say its conformal structure is *compatible* with the metric, if local representation of the metric on a chart (U_α, ϕ_α)

$$g = e^{2u} dz_\alpha d\bar{z}_\alpha,$$

where z_α is the local complex parameter. We also call such local complex parameter as *isothermal coordinates*. The *Laplace-Beltrami* operator Δ on an isothermal coordinates has a simple representation

$$\Delta = \frac{1}{e^{2u(x_\alpha, y_\alpha)}} \left(\frac{\partial^2}{\partial x_\alpha^2} + \frac{\partial^2}{\partial y_\alpha^2} \right).$$

All metric surfaces are Riemann surfaces and with isothermal coordinates. Therefore conformal geometric concepts and methods are general to all surfaces in real life.

2.3.3 Holomorphic One Forms

We have defined harmonic functions and harmonic forms in the setting of Riemannian manifolds. A *harmonic form* ω satisfies the following condition

$$d\omega = 0, \delta\omega = 0.$$

Now, we study harmonic forms on Riemann Surfaces.

Definition 2.29 (Holomorphic 1-form)**.** *A holomorphic 1-form is a pair of harmonic 1-forms, the imaginary part is conjugate to the real part:*

$$\tau = \omega + \sqrt{-1}^*\omega.$$

On the conformal atlas, τ has local representation on (U_α, ϕ_α) with local parameter z_α,

$$\tau = f_\alpha(z_\alpha)dz_\alpha,$$

where f_α is a holomorphic function. On another chart (U_β, ϕ_β) with local parameter z_β, $\tau = f_\beta dz_\beta$, such that

$$f_\alpha \frac{dz_\alpha}{dz_\beta} = f_\beta.$$

Hodge theorem claims that each cohomologous class has a unique harmonic 1-form. Therefore the group of all harmonic 1-forms is isomorphic to the first cohomology group $H^1(S, \mathbb{R})$. Also, the group of all holomorphic 1-forms is isomorphic to $H^1(S, \mathbb{R})$.

2.3.4 Riemann Mapping and Uniformization Theorem

In this part, we introduce two important theorem, which induces the existence of conformal structures on surfaces.

Theorem 2.30 (Riemann Mapping)**.** *Suppose $D \subset \mathbb{C}$ is a simply connected domain on the complex plane, the boundary ∂D has more than one point, $z_0 \in D$ is an arbitrary interior point. Then there exists a unique holomorphic mapping $\theta : D \to \Delta$ from D to the unist disk Δ, such that $\theta(z_0) = 0$ and $\theta'(z_0) > 0$.*

Simply speaking, this theorem says that a conformal mapping from a disk-like region to a unit disk always exists.

Theorem 2.31 (Uniformization)**.** *A simply connected Riemann surface is conformally equivalent to one of the following three canonical Riemann surfaces:*

1. *Exteded complex plane $\overline{\mathbb{C}} = \mathbb{C} \cup \infty$;*
2. *Complex plane $\mathbb{C}$;*
3. *Unit disk $\Delta = \{z \in \mathbb{C} || z| < 1\}$.*

This theorem says that any Riemann surface has a natural Riemannian metric with constant Gauss curvature, namely, spherical metric, Euclidean metric or hyperbolic metric (see Figure 6). This also proves the fact stated in the introduction (Section 1).

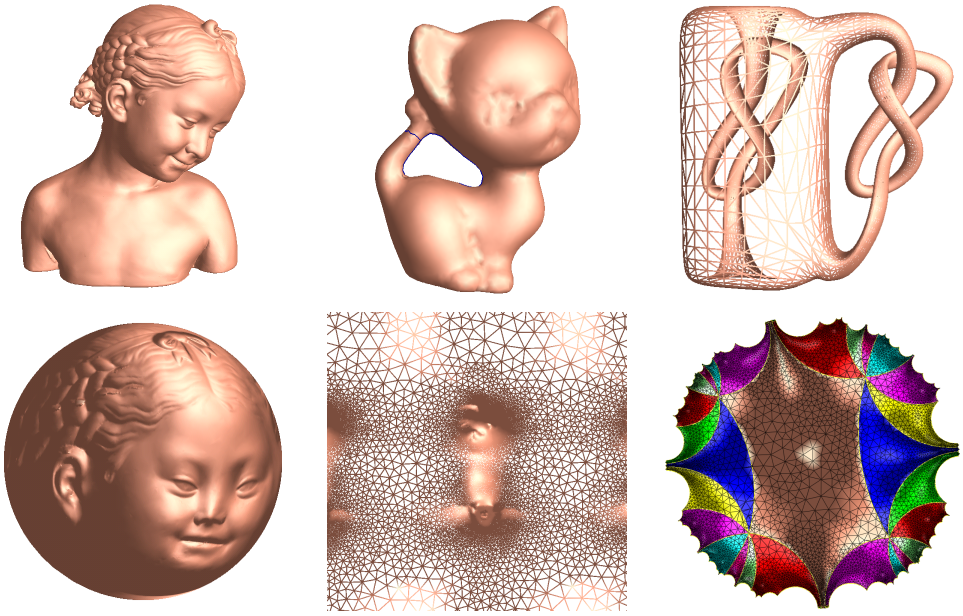

Figure 6: Surface uniformization theorem.

2.4 Surface Curvature Flow

Definition 2.32 (Isothermal Coordinates[121])**.** *Let S be a smooth surface with a Riemannian metric* $\mathbf{g}$*. Isothermal coordinates (u, v) for* $\mathbf{g}$ *satisfy*

$$\mathbf{g} = e^{2\lambda(u,v)}(du^2 + dv^2).$$

Locally, isothermal coordinates always exist. The Gaussian curvature[108] of the surface is given by

$$K(u, v) = -\Delta_{\mathbf{g}}\lambda, \tag{2.1}$$

where $\Delta_{\mathbf{g}} = e^{-2\lambda(u,v)}(\frac{\partial^2}{\partial u^2} + \frac{\partial^2}{\partial v^2})$ is the Laplace-Beltrami operator induced by $\mathbf{g}$. Although the Gaussian curvature is intrinsic to the Riemannian metric, the total Gaussian curvature is a topological invariant:

Theorem 2.33. *The total Gaussian curvature of a closed metric surface is*

$$\int_S K dA = 2\pi\chi(S),$$

where $\chi(S)$ is the Euler number of the surface[32].

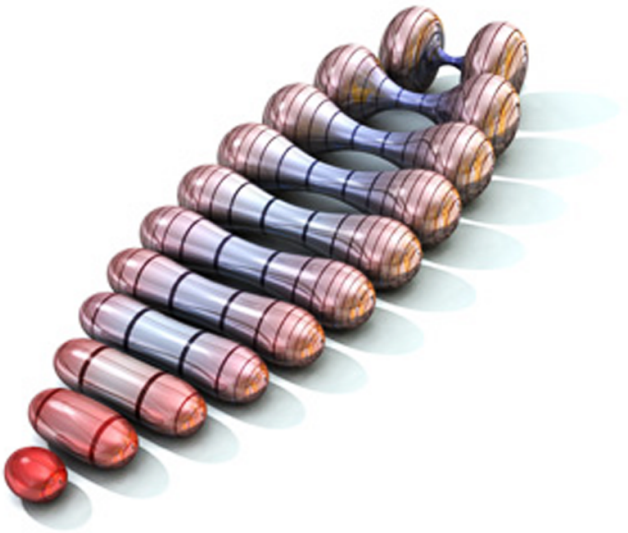

Figure 7: Surface Ricci Flow.

Suppose $\mathbf{g}_1$ and $\mathbf{g}_2$ are two conformal Riemannian metrics on the smooth surface S, such that

$$\mathbf{g}_2 = e^{2\lambda}\mathbf{g}_1.$$

Let the Gaussian curvatures of $\mathbf{g}_1$ and $\mathbf{g}_2$ be K_1 and K_2 respectively. Then they satisfy the following *Yamabe equation*

$$K_2 = \frac{1}{e^{2\lambda}}(K_1 - \Delta_{\mathbf{g}_1}\lambda).$$

Suppose the metric $\mathbf{g} = (g_{ij})$ in local coordinate. Hamilton introduced the Ricci flow as

$$\frac{dg_{ij}}{dt} = -Kg_{ij}.$$

For surface case, Ricci flow is equivalent to Yamabe flow[42][90]. During the flow, the Gaussian curvature will evolve according to a heat diffusion process.

Theorem 2.34. *Suppose S is a closed surface with a Riemannian metric. If the total area is preserved, the surface Ricci flow will converge to a Riemannian metric of constant Gaussian curvature[26][54].*

This gives another approach to prove the Poincaré uniformization theorem. As shown in Figure 6, all closed surfaces can be conformally deformed to one of the three canonical spaces: the sphere $\mathbb{S}^2$, the Euclidean plane $\mathbb{E}^2$, or the hyperbolic space $\mathbb{H}^2$.

3 Computational Algorithms

3.1 Algebraic Topology

Fundamental Group Generators The method of computing fundamental group generators is straightforward. Suppose the surface is represented as discrete triangle mesh M.

1. Choose a base vertex v_0, use breadth first search based on Dijkstra's method to compute a spanning tree T of all vertices.

2. Compute the dual mesh $\bar{M}$ of the original mesh. Compute the *cut graph*

$$G = \{\bar{e} \notin T | e \in M\}, \tag{3.1}$$

   where $\bar{e}$ is the edge in $\bar{M}$ dual to e.

3. Compute the weight of each edge $\bar{e} \in G$. Suppose the boundary vertices of e are $\partial e = v_2 - v_1$, then in the spanning tree T, there are unique paths from v_k to the root v_0, denoted as γ_k, $k = 1, 2$. The weight of edge $\bar{e}$ is defined as

$$w(\bar{e}) = l(\gamma_1) + l(\gamma_2) + l(e),$$

   where $l(\gamma_k)$ is the length of the path γ_k, $l(e)$ is the length of the edge e.

4. Compute a maximal spanning tree T_G of G using the above weight.

5. Remove T_G from G, there will be $2g$ edges left

$$G - T_G = \{\bar{e}_1, \bar{e}_2, \cdots, \bar{e}_{2g}\},$$

6. $T \cup e_k$ includes a unique loop, use the same notation as γ_k, then $\{\gamma_1, \gamma_2, \cdots, \gamma_{2g}\}$ form a set of fundamental group generators.

Fuchs Group Generators For a genus one mesh, we have obtained the flat metric with zero curvatures everywhere by running Ricci flow. We cut the mesh along the fundamental group generators $\{a, b\}$ obtained in the first step, the resulting mesh is fundamental domain $\bar{M}$. Then we isometrically embed face by face onto the plane, until we flatten the whole fundamental domain onto the plane. We denote the flattening mapping as $\phi : \bar{M} \to \mathbb{R}^2$. There is a unique planar translation α, which maps $\phi(a)$ to $\phi(a^{-1})$. Similarly, there is a unique planar translation β, which maps $\phi(b^{-1})$ to $\phi(b)$. Then $\{\alpha, \beta\}$ form the basis of the Deck transformation group of the universal covering $\tilde{M}$ of M.

For a high genus mesh $g > 1$, the hyperbolic metric is obtained by Ricci flow. Then we slice the surface open along the cut graph G (see formula 3.1) to get a fundamental domain $\bar{M}$. Then we isometrically flatten face by face onto the Poincaré disk, to map the whole

fundamental domain to the hyperbolic plane, $\phi : \bar{M} \to \mathbb{H}^2$. Let the fundamental group generators are $\{a_1, b_1, a_2, b_2, \cdots, a_g, b_g\}$, which are loops in the cut graph G, then these loops and their inverses are boundary segments on $\bar{M}$. There exists a unique Möbius transformation α_k, which maps $\phi(a_k)$ to $\phi(a_k^{-1})$, and a unique β_k, which maps $\phi(b_k)$ to $\phi(b_k^{-1})$. These hyperbolic rigid motions $\{\alpha_1, \beta_1, \alpha_2, \beta_2, \cdots, \alpha_g, \beta_g\}$ form a set of generators of the Fuchs group.

Finite Portion of the Universal Covering Space For surfaces with genus greater than zero, once the fundamental domain and the Deck transformation group generators have been calculated, we can tessellate the canonical space.

For genus one case, the whole plane $\mathbb{R}^2$ can be tessellated by the fundamental domains, translated by Deck transformations,

$$\mathbb{R}^2 = \bigcup_{\alpha \in Deck(\tilde{M})} \alpha \circ \phi(\bar{M}).$$

We choose a small set of Deck transformations, $\Gamma = \{a^i b^j\}$, where i, j are integers, $-2 \leq i, j \leq 2$. Then the finite portion is given by

$$\tilde{M} := \bigcup_{\alpha \in \Gamma} \alpha \circ \phi(\bar{M}).$$

For high genus surface, the whole hyperbolic plane $\mathbb{H}^2$ can be tessellated by the fundamental domains, transformed by Fuchs group elements,

$$\mathbb{H}^2 = \bigcup_{\alpha \in Fuchs(M)} \alpha \circ \phi(\bar{M}).$$

We select a small set of Fuchs transformations, $\Gamma = \{\gamma_1^i \gamma_2^j\}$, where $\gamma_1, \gamma_2 \in \{\alpha_k, \beta_k, k = 1, 2 \cdots, g\}$, i, j are integers, $-2 \leq i, j \leq 2$. Then the finite portion of the universal covering space is given by

$$\tilde{M} = \bigcup_{\alpha \in \Gamma} \alpha \circ \phi(\bar{M}).$$

According to surface uniformization theorem and the above steps of computation, any arbitrary Riemann surface can be mapped to one of three canonical domains. As shown in Figure 6, genus zero surfaces in the left are mapped to unit sphere, the universal covering space is the unit sphere itself. Genus one surfaces in the middle are mapped to a parallelogram, the universal covering space is the whole plane; the rigid motions are Deck transformations (i.e., translations). High genus surfaces in the right can be mapped to a hyperbolic polygon, the universal covering space is the Poincaré disk; the rigid motions are Fuchs transformations (i.e., Möbius transformations); the patches in different colors denote different periods.

3.2 Discrete Differential Geometry

Discrete exterior forms, and discrete exterior calculus are discrete versions of the concepts of differential geometry. Here we list some important definitions and operators, which can be directly applied in designing Computational Conformal Geometry algorithms. A detailed introduction and proof of convergence to the smooth case can be found in [57].

Definition 3.1 (Cochain)**.** *k-cochain ω is the dual of a k-chain, that is to say, $\omega : C \to \mathbb{R}$ is a linear mapping that takes k-chains to $\mathbb{R}$.*

A k-cochain ω operates on a k-chain c to give a scalar in R. Since a chain is a linear combination of simplices, a cochain returns a linear combination of the values of that cochain on each simplex involved.

Definition 3.2 (Coboundary Operator)**.** *The operator d, or the coboundary operator can be discretized using Theorem 2.9. d applies to an arbitrary form ω is evaluated on an arbitrary simplex σ as follows:*

$$\int_{\sigma} d\omega = \int_{\partial\sigma} \omega.$$

Generally speaking,

$$\int_{\sum_i c_i\sigma_i} d\omega = \int_{\partial(\sum_i c_i\sigma_i)} \omega = \int_{\sum_i c_i\partial\omega_i} \omega = \sum_i c_i \int_{\partial\sigma_i} \omega$$

Cochains and the coboundary operator are discrete analogs to differential forms and the differential operator, respectively.

Definition 3.3 (Discrete Wedge Product)**.** *Suppose $\{d_0, d_1, d_2\}$ are the oriented edges of a triangle T, their lengths are $\{l_0, l_1, l_2\}$, and the area of T is s, then the discrete wedge product $\wedge$ is defined as*

$$\int_T \omega \wedge \tau = \frac{1}{6} \begin{pmatrix} \omega(d_0) & \omega(d_1) & \omega(d_2) \\ \tau(d_0) & \tau(d_1) & \tau(d_2) \\ 1 & 1 & 1 \end{pmatrix}$$

Definition 3.4 (Discrete Star Wedge Product)**.** *The discrete star wedge product on meshes is defined as*

$$\int_T \omega^* \wedge \tau = UMV^T,$$

where

$$M = \frac{1}{24s} \begin{pmatrix} -4l_0^2 & l_0^2 + l_1^2 - l_2^2 & l_0^2 + l_2^2 - l_1^2 \\ l_1^2 + l_0^2 - l_2^2 & -4l_1^2 & l_1^2 + l_2^2 - l_0^2 \\ l_2^2 + l_0^2 - l_1^2 & l_2^2 + l_1^2 - l_0^2 & -4l_2^2 \end{pmatrix}$$

and

$$U = (\omega(d_0), \omega(d_1), \omega(d_2))V = (\tau(d_0), \tau(d_1), \tau(d_2)).$$

Definition 3.5 (Discrete Hodge Star)**.** *Once we know a set of basis of Harmonic forms* $\{\omega_1, \omega_2, \omega_3, \ldots, \omega_{2g}\}$*, suppose* $\star\omega = \sum_{i=1}^{2g} \lambda_i \omega_i$*, we can found out* λ_i*'s by solving the following linear system*

$$\int_M \omega_i \wedge \star\omega = \int \omega_i \star \wedge\omega, i = 1, 2, \ldots, 2g,$$

which reduces to solving a linear equation in the discrete setting,

$$W\Lambda = B.$$

Here W *has entries* $w_{ij} = \sum_{T\in M} \int_T \omega_i \wedge \omega_j$*,* Λ *has entries* λ_i*, and* B *has entries* $b_i = \sum_{T\in M} \int_T \omega_i \star \wedge\omega$*.*

Definition 3.6 (Discrete Laplace Operator)**.** *Suppose* M *is a triangular mesh. The piecewise Laplacian is a linear operator acting on a 0-form on the mesh* f *(0-form) to get another 0-form:*

$$\Delta f(v_i) = \sum_{[v_i, v_j]\in M} k_{ij}(f(v_j) - f(v_i)).$$

Here k_{ij} *is calculated by cotangent formula: if* e_{ij} *is an interior edge adjacent to two faces, and* α, β *are the angles against it, then* $k_{ij} = \frac{1}{2}(\cot\alpha + \cot\beta)$*; if it is a boundary edge, then* $k_{ij} = \frac{1}{2}\cot\alpha$ *(the definition of* α *is similar to the previous case).*

Definition 3.7 (Discrete Gaussian Curvature)**.** *The discrete Gaussian curvature* K_i *on a vertex* $v_i \in \Sigma$ *can be computed from the angle deficit,*

$$K_i = \begin{cases} 2\pi - \sum_{f_{ijk}\in F} \theta_i^{jk}, & v_i \notin \partial\Sigma \\ \pi - \sum_{f_{ijk}\in F} \theta_i^{jk}, & v_i \in \partial\Sigma \end{cases}$$

where θ_i^{jk} *represents the corner angle attached to vertex* v_i *in the face* f_{ijk}*, and* $\partial\Sigma$ *represents the boundary of the mesh. The discrete Gaussian curvatures are determined by the discrete metrics.*

Theorem 3.8 (Discrete Gauss-Bonnet Theorem)**.** *The Gauss-Bonnet theorem states that the total curvature is a topological invariant. It still holds on meshes as follows.*

$$\sum_{v_i\in V} K_i + \lambda \sum_{f_i\in F} A_i = 2\pi\chi(M),$$

where A_i *denotes the area of face* f_i*, and* λ *represents the constant curvature for the background geometry;* $+1$ *for the spherical geometry,* 0 *for the Euclidean geometry, and* -1 *for the hyperbolic geometry.*

3.3 Discrete Harmonic Mappings

Harmonic maps can be computed using heat flow method. For example, we want to compute a harmonic map from a genus zero closed surface to the unit sphere $\phi : S \to \mathbb{S}^2$. We can initialize the map by the canonical Gauss map, then minimize the harmonic energy by the heat flow. First we compute the Laplacian of the map $\Delta\phi : S \to \mathbb{R}^3$. Then we compute the tangential component of the Laplacian. Suppose $p \in S$, then $\phi(p) \in \mathbb{S}^2$.

$$\Delta^{\perp}\phi(p) =< \Delta^{\perp}\phi(p), \phi(p) > \phi(p),$$

The tangential component of the laplacian is given by

$$\Delta^{\parallel}\phi(p) = \Delta\phi(p) - \Delta^{\perp}\phi(p).$$

The heat flow is defined as

$$\frac{d\phi(p,t)}{dt} = -\Delta^{\parallel}\phi(p).$$

Because the harmonic map is not unique (they differ by a Möbius transformation on the sphere), special normalization condition needs to be added during the flow. The following is a common condition,

$$\int_S \phi(p)ds = 0.$$

For genus zero closed surface, harmonic maps are conformal.

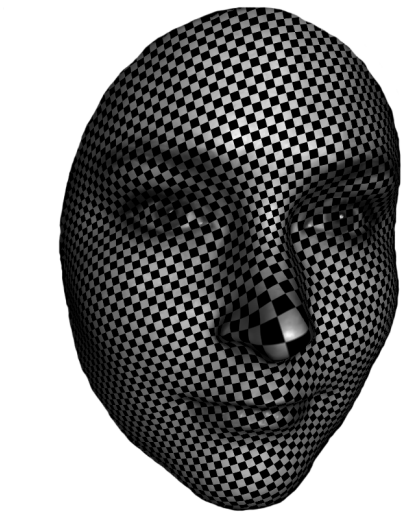

Figure 8: Harmonic mapping.

3.4 Discrete Holomorphic One Form

To calculate the discrete holomorphic one forms on surfaces, we need to consider homology basis, cohomology basis, harmonic 1-form basis in order. The computational algorithm for holomorphic 1-forms is as the following: first a cohomology group basis is constructed using algebraic topological methods; then cohomology basis are diffused to be harmonic forms using the heat flow method; finally the conjugate of harmonic forms are computed to form the holomorphic 1-forms.

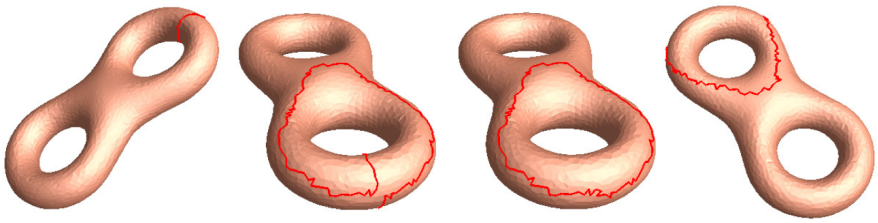

Figure 9: Computing homology group basis.

Homology Basis Given a surface S embedded in $\mathbb{R}^3$, we first compute its fundamental group generators. We compute its CW-cell decomposition

$$S_0 \subset S_1 \subset S_2 = S,$$

where $S_k = S_{k-1} \cup D_k^1 \cup D_k^2 \cdots \cup D_k^n$, where D_k^i are k-dimensional cells (disks), such that the boundaries of these cells are on S_{k-1},

$$\partial D_k^i \subset S_{k-1}.$$

Then the fundamental group of S_1 is isomorphic to the fundamental group of S. Then we compute a spanning tree of S_0 in S_1, the complement of T in S_1 are disconnected 1-cells, denoted as $e_1, e_2, \cdots e_k$, then the union of T and e_i has a unique loop γ_i. All such loops $\{\gamma_1, \gamma_2, \cdots, \gamma_{2g}\}$ form a basis for the fundamental group $\pi_1(S)$. These loops also form the basis of the first homology basis $H_1(S, \mathbb{Z})$. Figure 3.4 shows the homology group generators of a genus two surface.

Cohomology Basis Let γ_k be a base loop for $H_1(S, \mathbb{Z})$, then we slice S along γ_k to get an open surface S_k, such that the boundary of S_k is given by

$$\partial S_k = \gamma_k^+ - \gamma_k^-,$$

$\gamma_k^+, \gamma_k^{-1}$ are the two boundary loops on S_k. Then we randomly construct a function $h_k : S_k \to \mathbb{R}$, such that

$$h_k(p) = 1, \forall p \in \gamma_k^+;\ h_k(p) = 0, \forall p \in \gamma_k^-;$$

and $h_k(p)$ is random for all interior points on S_k. Then dh_k is an exact 1-form on S_k. Because of the consistency along the boundaries, dh_k is also a closed 1-form on S. We denote τ_k as dh_k on S. Then $\{\tau_1, \tau_2, \cdots, \tau_{2g}\}$ form a basis for $H^1(S, \mathbb{R})$.

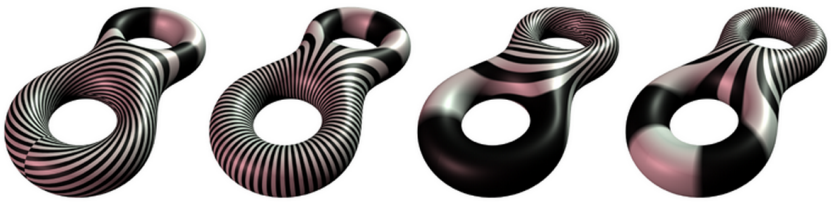

Figure 10: Computing harmonic 1-form group basis.

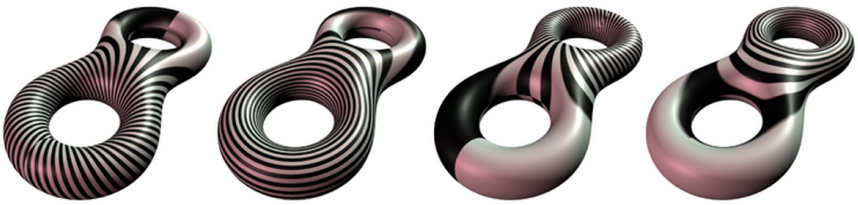

Figure 11: Computing harmonic 1-form group basis.

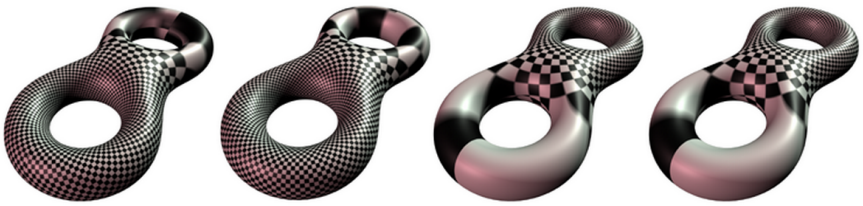

Figure 12: Computing harmonic 1-form group basis.

Harmonic 1-form Basis According to Hodge theory, for each closed 1-form τ_k, there exists a 0-form $g_k : S \to \mathbb{R}$, such that $\tau_k + dg_k$ is a harmonic 1-form. g_k can be obtained by solving the following equation

$$d * (\tau_k + dg_k) = 0.$$

We denote the harmonic 1-form as $\omega_k = \tau_k + dg_k$. Figure 24 shows the harmonic group generators of a genus two surface.

Holomorphic 1-form can be constructed by harmonic 1-form and its conjugate $\omega_k + \sqrt{-1}^* \omega_k$. Then $\{\omega_1 + {}^*\omega_1, \omega_2 + {}^*\omega_2, \cdots, \omega_{2g} + {}^*\omega_{2g}\}$ form a basis for holomorphic 1-form group. Figure 3.4 shows the holomorphic 1-form group basis for the genus two surface.

With the basic definitions above, we are ready to introduce the algorithm of computing conformal structure for surfaces[135][114]. Suppose S is a surface embedded in the Euclidean space R^3, as we have shown, its first fundamental form is called the Riemannian metric, which is represented as a tensor $g = (g_{ij})$. A metric defines an inner product for the tangent vectors. A tangent vector can be represented as $TM = a(u, v)\frac{\partial}{\partial u} + b(u, v)\frac{\partial}{\partial v}$.

According to Riemann surface theory, conformal gradient fields $\omega + \sqrt{(-1)} * \omega$ have the following properties:

- ***closedness*** ω and $*\omega$ are closed, meaning the curlix of ω and $*\omega$ are both zero.
- ***harmonity*** ω and $*\omega$ are harmonic, meaning that the Laplacian of both ω and $*\omega$ are zero.
- ***duality*** The cohomology class of ω and $*\omega$ can be determined by the values of their integration along the homology basis e_i Ł.
- ***conjugacy*** $*\omega$ is orthogonal to ω everywhere.

According to Hodge theory [137], given $2g$ real numbers $c_1, c_2, \ldots, c_{2g}$, there is a unique real gradient field ω with the first three properties, because each cohomology class has a unique harmonic gradient field ω. These properties for ω can be formulated as the following equations:

$$\begin{cases} d\omega = 0 \\ \Delta\omega = 0 \\ \int_{e_i} \omega = c_i, i = 1, 2, ...2g \end{cases} \tag{3.2}$$

The equations $\int_{e_i} \omega = c_i, i = 1, 2, \ldots, 2g$ restricts the cohomology class of ω. The conjugacy property can be formulated as

$$\star\omega = \overrightarrow{n} \times \omega \tag{3.3}$$

where $\overrightarrow{n}$ is the normal field on the surface, $\times$ is the cross product in R^3. This equation holds everywhere on the surface.

According to [48][46][66], The closedness property $d\omega = 0$ means the integration of ω along any simple closed curve (which bounds a topological disk) is zero. Then for each face $[u, v, w]$, the equation for closedness can be approximated by the following linear equation:

$$\omega(\partial[u, v, w]) = \omega[u, v] + \omega[v, w] + \omega[w, u] = 0 \tag{3.4}$$

The harmonity property $\Delta w = 0$ can be formulated using the well known cotangent weighting coefficients. For any vertex u, the Laplacian of ω on u is zero, hence the equation for harmonity can be formulated as:

$$\Delta\omega(u) = \sum_{[u,v]\in M} k_{u,v}\omega[u, v] = 0 \tag{3.5}$$

$$k_{u,v} = -\frac{1}{2}(\cot\alpha + \cot\beta) \tag{3.6}$$

where α, β are the angles against the edge $[u, v]$.

The duality property $\int_{e_i} \omega = c_i$ can be implemented simply by summing up all the forms on the edge $e_i = \sum_{j=1}^{n}[u_{j-1}, u_j]$ where $u_0 = u_n$,

$$\int_{e_i} \omega = \sum_{j=1}^{n} \omega[u_{j-1}, u_j] = c_j. \tag{3.7}$$

Once we have computed ω, we can compute $\star\omega$ by using the discrete Hodge star operator, which is defined as follows. Suppose $\{d_0, d_1, d_2\}$ are the oriented edges of a triangle T, their lengths are $\{l_0, l_1, l_2\}$, and the area of T is s, then the discrete wedge product $\wedge$ is defined as

$$\int_T \omega \wedge \tau = \frac{1}{6}\begin{pmatrix} \omega(d_0) & \omega(d_1) & \omega(d_2) \\ \tau(d_0) & \tau(d_1) & \tau(d_2) \\ 1 & 1 & 1 \end{pmatrix} \tag{3.8}$$

The star wedge product $\star\wedge$ of $\wedge$ and τ on smooth surfaces is defined as follows:

$$\int_M \omega^* \wedge \tau = \int_M \omega \wedge^* \tau = \int_M \omega \times^* \tau \cdot \overrightarrow{n}, \tag{3.9}$$

where ${}^*\tau$ is obtained by rotating τ about the normal $\overrightarrow{n}$ on the tangent plane at each point of M. The discrete star wedge product on meshes is defined as

$$\int_T \omega^* \wedge \tau = UMV^T, \tag{3.10}$$

where

$$M = \frac{1}{24s}\begin{pmatrix} -4l_0^2 & l_0^2+l_1^2-l_2^2 & l_0^2+l_2^2-l_1^2 \\ l_1^2+l_0^2-l_2^2 & -4l_1^2 & l_1^2+l_2^2-l_0^2 \\ l_2^2+l_0^2-l_1^2 & l_2^2+l_1^2-l_0^2 & -4l_2^2 \end{pmatrix} \tag{3.11}$$

and

$$U = (\omega(d_0), \omega(d_1), \omega(d_2)) \tag{3.12}$$

$$V = (\tau(d_0), \tau(d_1), \tau(d_2)). \tag{3.13}$$

Therefore, once we know a set of basis of Harmonic forms $\{\omega_1, \omega_2, \omega_3, \ldots, \omega_{2g}\}$, suppose $\star\omega = \sum_{i=1}^{2g} \lambda_i \omega_i$, we can found out λ_i's by solving the following linear system

$$\int_M \omega_i \wedge \star\omega = \int \omega_i \star \wedge\omega, i = 1, 2, \ldots, 2g, \tag{3.14}$$

which reduces to solving a linear equation in the discrete setting,

$$W\Lambda = B. \tag{3.15}$$

Here W has entries $w_{ij} = \sum_{T\in M} \int_T \omega_i \wedge \omega_j$, Λ has entries λ_i, and B has entries $b_i = \sum_{T\in M} \int_T \omega_i \star \wedge\omega$.

Now we can summarize the discrete conformal mapping algorithm in algorithm 1:

3.5 Discrete Surface Ricci Flow

Background Geometry In engineering field, it is always assumed that a mesh Σ is embedded in the three dimensional Euclidean space $\mathbb{R}^3$, and therefore each face is Euclidean. In this case, we say the mesh is with Euclidean background geometry. The angles and edge lengths of each face satisfy the Euclidean cosine law.

Similarly, we can assume that a mesh is embedded in the three dimensional sphere $\mathbb{S}^3$ or hyperbolic space $\mathbb{H}^3$, then each face is a spherical or a hyperbolic triangle. We say the mesh is with spherical or hyperbolic background geometry. The angles and the edge lengths of each face satisfy the spherical or hyperbolic cosine law.

Algorithm 1 Discrete Conformal Mapping Algorithm.

Input: Surfaces M.

Output: The conformal parameterization U of M.

1. Compute the Harmonic 1-Form basis for M by solving linear system 9.
2. Compute the Conjugate Harmonic 1-Form basis for M by solving linear system 22.
3. Combine the Harmonic 1-Form basis and Conjugate Harmonic 1-Form basis we get a conformal structure U of surface M.

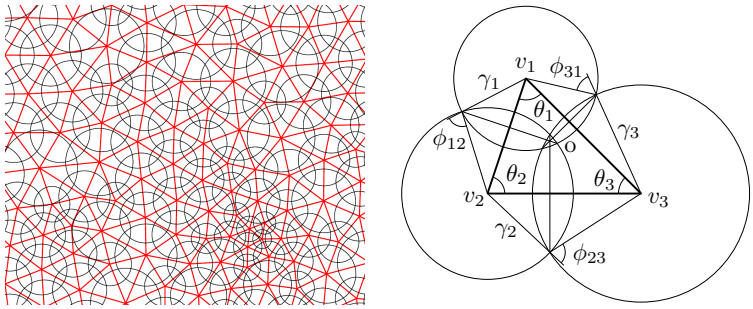

(a) (b)

Figure 13: Circle Packing Metric. (a) Flat circle packing metric (b) Circle packing metric on a triangle.

Discrete Riemannian Metric A discrete Riemannian metric on a mesh Σ is a piecewise constant metric with cone singularities. A metric on a mesh with Euclidean metric is a discrete Euclidean metric with cone singularities. Each vertex is a cone singularity. Similarly, a metric on a mesh with spherical background geometry is a discrete spherical metric with cone singularities; a metric on a mesh with hyperbolic background geometry is a discrete hyperbolic metric with cone singularities.

The edge lengths of a mesh Σ are sufficient to define a discrete Riemannian metric,

$$l : E \to \mathbb{R}^+,$$

as long as, for each face f_{ijk}, the edge lengths satisfy the triangle inequality: $l_{ij} + l_{jk} > l_{ki}$ for all the three background geometries, and another inequality: $l_{ij} + l_{jk} + l_{ki} < 2\pi$ for spherical geometry.

Circle Packing Metric The concept of the circle packing metric was introduced by Thurston in [132] as shown in Figure 13. Let Γ be a function defined on the vertices, $\Gamma : V \to \mathbb{R}^+$, which assigns a radius γ_i to the vertex v_i. Similarly, let Φ be a function defined on the edges, $\Phi : E \to [0, \frac{\pi}{2}]$, which assigns an acute angle $\Phi(e_{ij})$ to each edge e_{ij} and is called a *weight* function on the edges. Geometrically, $\Phi(e_{ij})$ is the intersection angle of two circles centered at v_i and v_j. The pair of vertex radius function and edge weight function on a mesh Σ, (Γ, Φ), is called a *circle packing metric* of Σ.

Figure 13 illustrates the circle packing metrics. Each vertex v_i has a circle whose radius is γ_i. For each edge e_{ij}, the intersection angle ϕ_{ij} is defined by the two circles of v_i and v_j, which either intersect or are tangent. Two circle packing metrics (Γ_1, Φ_1) and (Γ_2, Φ_2) on the same mesh are *conformally equivalent* if $\Phi_1 \equiv \Phi_2$.

Admissible Curvature Space A mesh Σ with edge weight Φ is called a *weighted mesh*, which is denoted as (Σ, Φ). In the following, we want to clarify the spaces of all possible circle packing metrics and all possible curvatures of a weighted mesh.

Let the vertex set be $V = \{v_1, v_2, \cdots, v_n\}$, and the radii be $\Gamma = \{\gamma_1, \gamma_2, \cdots, \gamma_n\}$. Let u_i be

$$u_i = \begin{cases} \log \gamma_i & \mathbb{E}^2 \\ \log \tanh \frac{\gamma_i}{2} & \mathbb{H}^2 \\ \log \tan \frac{\gamma_i}{2} & \mathbb{S}^2 \end{cases}$$

where $\mathbb{E}^2$, $\mathbb{H}^2$, and $\mathbb{S}^2$ indicate the background geometry of the mesh. We represent a circle packing metric on (Σ, Φ) by a vector $\mathbf{u} = (u_1, u_2, \cdots, u_n)^T$. Similarly, we represent the Gaussian curvatures at mesh vertices by the curvature vector $\mathbf{k} = (K_1, K_2, \cdots, K_n)^T$. All the possible $\mathbf{u}$'s form the *admissible metric space*, and all the possible $\mathbf{k}$'s form the *admissible curvature space*.

According to Theorem 3.8, the total curvature must be $2\pi\chi(\Sigma)$, and therefore the curvature space is $n-1$ dimensional. We add one linear constraint to the metric vector $\mathbf{u}$, $\sum u_i = 0$, for the normalized metric. As a result, the metric space is also $n-1$ dimensional. If all the intersection angles are acute, then the edge lengths induced by a circle packing satisfy the triangle inequality. There is no further constraint on $\mathbf{u}$. Therefore, the admissible metric space is simply $\mathbb{R}^{n-1}$.

A curvature vector $\mathbf{k}$ is *admissible* if there exists a metric vector $\mathbf{u}$, which induces $\mathbf{k}$. The admissible curvature space of a weighted mesh (Σ, Φ) is a convex polytope, specified by the following theorem. The detailed proof can be found in [27].

The admissible curvature space for weighted meshes with hyperbolic or spherical background geometries is more complicated. We refer the readers to [91] for detailed discussion.

Ricci Flow Suppose (Σ, Φ) is a weighted mesh with an initial circle packing metric. The discrete Ricci flow is defined as follows.

$$\frac{du_i(t)}{dt} = \bar{K}_i - K_i,$$

where $\bar{\mathbf{k}} = (\bar{K}_1, \bar{K}_2, \cdots, \bar{K}_n)^T$ is the user defined target curvature. The discrete Ricci flow has exactly the same form as the smooth Ricci flow, which deforms the circle packing metric according to the Gaussian curvature.

The discrete Ricci flow can be formulated in the variational setting, namely, it is a negative gradient flow of a special energy form. The energy is given by

$$f(\mathbf{u}) = \int_{\mathbf{u_0}}^{\mathbf{u}} \sum_{i=1}^{n} (\bar{K}_i - K_i) du_i$$

where $\mathbf{u_0}$ is an arbitrary initial metric. The energy is called the *discrete Ricci energy*.

Computing the desired metric with user-defined curvature $\bar{\mathbf{k}}$ is equivalent to minimizing the discrete Ricci energy.For Euclidean or hyperbolic cases, the discrete Ricci energy was first proved to be strictly convex in the seminal work in [30] for the $\Phi = 0$ case, and was generalized to all cases of $\Phi \leq \pi/2$ in [27]. The global minimum uniquely exists, corresponding to the metric $\bar{\mathbf{u}}$, which induces $\bar{\mathbf{k}}$. The discrete Ricci flow converges to this global minimum. Although the spherical Ricci energy is not strictly convex, the desired metric $\bar{\mathbf{u}}$ is still a critical point of the energy.

The energy can be optimized using Newton's method. As shown in figure 13(b), for each face f_{ijk} there exists a unique circle orthogonal to all three circles at the vertices, whose center is o. The distance from the center to edge e_{ij} is denoted as d_{ij}^k. The weight for an edge e_{ij} adjacent to f_{ijk} and f_{jil} is defined as

$$\mu_{ij} = d_{ij}^k + d_{ij}^l.$$

The Hessian matrix $H = (h_{ij})$ is given by the discrete Laplace form

$$h_{ij} = \begin{cases} 0, & [v_i, v_j] \notin E \\ d_{ij}, & i \neq j \\ \sum_k d_{ik}, & i = j \end{cases}$$

Figure 14 shows the result for computing the uniformization hyperbolic metric for a genus two surface. The universal covering space of the surface with the uniformization metric is isometrically embedded in the Poicaré disk.

Algorithm 2 Discrete Hyperbolic Ricci Flow.

Input: Surface M with negative Euler number.

Output: The hyperbolic metric U of M.

1. Assign a circle at vertex v_i with radius r_i, compute the discrete conformal factor u_i; For each edge $[v_i, v_j]$, two circles intersect at an angle ϕ_{ij}, called edge weight.

2. The edge length l_{ij} of $[v_i, v_j]$ is determined by the hyperbolic cosine law: $\cosh l_{ij} = \cosh r_i \cosh r_j + \sinh r_i \sinh r_j \cos \phi_{ij}$

3. The angle θ_i^{jk}, related to each corner , is determined by the current edge lengths with the inverse hyperbolic cosine law.

4. Compute the discrete Gaussian curvature K_i of each vertex v_i:

$$K_i = \begin{cases} 2\pi - \sum_{f_{ijk} \in F} \theta_i^{jk}, & \text{interior vertex} \\ \pi - \sum_{f_{ijk} \in F} \theta_i^{jk}, & \text{boundary vertex} \end{cases} \tag{3.16}$$

where θ_i^{jk} represents the corner angle attached to vertex v_i in the face f_{ijk}

5. Update the radius r_i of each vertex v_i: $u_i = u_i - \epsilon K_i$

6. Repeat the step 2 through 5, until $\|K_i\|$ of all vertices are less than the user-specified error tolerance.

4 Hyperbolic Harmonic Mapping for Constrained Surface Registration

Automatic computation of surface correspondence via harmonic map is an active research field in computer vision, computer graphics and computational geometry. It may help document and understand physical and biological phenomena and also has broad applications in biometrics, medical imaging and motion capture. Although numerous studies have been devoted to harmonic map research, limited progress has been made to compute a diffeomorphic harmonic map on general topology surfaces with landmark constraints. This work conquer this problem by changing the Riemannian metric on the target surface to a hyperbolic metric, so that the harmonic mapping is guaranteed to be a diffeomorphism under landmark constraints. The computational algorithms are based on the Ricci flow and nonlinear heat diffusion methods. The approach is general and robust. We apply our algorithm to study constrained surface registration problem which applied to both medical and computer vision applications. Experimental results demonstrate that, by changing the Riemannian metric, the registrations are always diffeomorphic, and achieve relative high performance when evaluated with some popular surface registration evaluation standards.

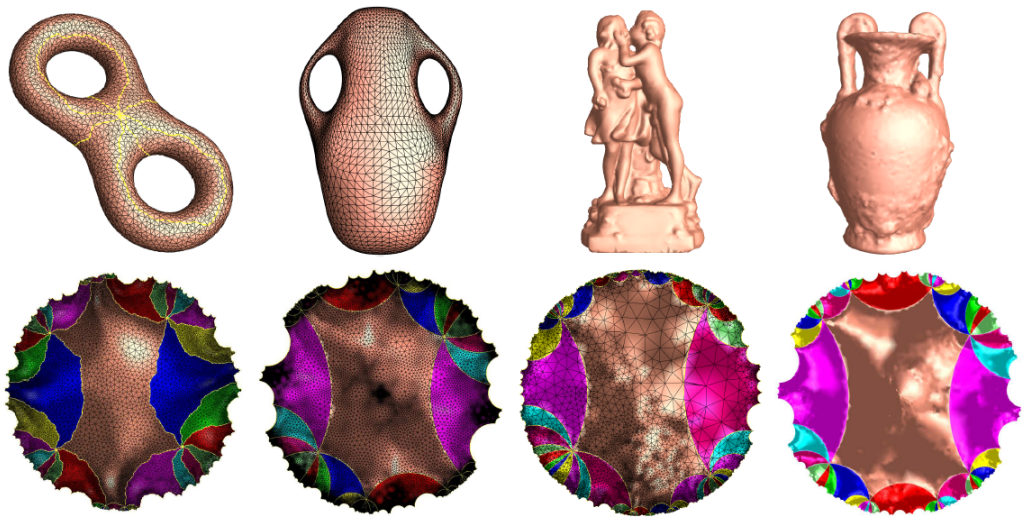

Figure 14: Hyperbolic Ricci flow method to compute a conformal mapping for a genus two surface.

4.1 Overview

Analysis and understanding of shapes is one of the most fundamental tasks in our interaction with the surrounding world. There are two major problems in shape analysis research: similarity and correspondence. Examples of similarity research include 3D face recognition [17], shape retrieval [19], etc. Among various correspondence research, automatic computation of surface correspondence regulated by certain geometric or functional constraints is an important research field in computer vision and medical imaging. For example, in human brain mapping research, since cytoarchitectural and functional parcellation of the cortex is intimately related the folding of the cortex, it is important to ensure the alignment of the major anatomic features, such as sucal landmarks.

Among various rigid and non-rigid surface registration approaches (e.g. [12, 17, 78]), harmonic map is one of the most broadly applied methods [1, 154]. The advantages of harmonic map computation are: (1) it is physically natural and can be computed efficiently; (2) it measures the elastic energy of the deformation so it has clear physical interpretation; (3) for a planar convex domain, it is diffeomorphism; (4) it can be computed by solving an elliptic partial differential equation so its computation is numerically stable; (5) it continuously depends on the boundary condition so it can be controlled by adjusted boundary conditions. In computer vision and medical imaging fields, surface harmonic map has been used to compute spherical conformal mapping [45], image registration [68], high resolution tracking of non-rigid motion [1], non-rigid surface registration [87], etc.

However, the current state-of-the-art surface harmonic map research has some limitations. For example, it usually only works with genus zero surfaces but does not work with general topology surfaces. It is hard to add landmark curve information. A harmonic map combined with landmark matching conditions usually does not guarantee diffeomorphism. All these problems become obstacles to apply harmonic map to solve general non-rigid surface matching problems. In contrast, in current work, we slice along the landmark curves on general surfaces and assign a unique hyperbolic metric on the template surface, such that all the boundaries become geodesics. Then by establishing harmonic mappings, the obtained surface correspondences are guaranteed to be diffeomorphic.

In this work, we apply the proposed method to study human brain cortical surface registration problem. Early research [40, 131] has demonstrated that surface-based approaches may offer advantages as a method to register brain images. The cortical surface registration may help identify early disease imaging biomarkers, develop new treatments and monitor their effectiveness, as well as lessen the time and cost of clinical trials.

In order to overcome these difficulties, this work proposes a novel method to establish harmonic maps between surfaces with complicated topologies, incorporating landmark curve constraints. We call our method as *Hyperbolic Harmonic Map*, which is based on the following key ideas:

1. *Metric Change* In general, harmonic maps between two surfaces with negative Euler numbers may not be diffeomorphic. According to Yau's harmonic mapping theory, if the Riemannian metric of the target surface induces negative Gaussian curvature everywhere, then the harmonic map is unique and diffeomorphic. Therefore, we deform the target surface metric to be hyperbolic based on our prior work of hyperbolic Ricci flow method [151], then the harmonic map obtained is guaranteed to be diffeomorphic.

2. *Topology Change* If the landmark curve constraints are required, the source and the target surfaces are sliced along these landmarks, such that the topologies of the surfaces are modified, the landmarks are converted to boundaries. Then the metric on the target is Then the harmonic map is established between the modified surfaces with Dirichlet boundary conditions. Then apply the above method to deform the metric on the target, establish the harmonic map. The final registration is ensured to be diffeomorhic and with the desired landmark alignment.

Furthermore, we apply the proposed method to study cortical, facial and general surface registration problem.

In summary, the main contributions of the current work are as follows: 1. Introduce a novel algorithm to compute harmonic mappings on hyperbolic metric using nonlinear heat diffusion method and Ricci flow. 2. Develop a novel surface registration method based on hyperbolic harmonic maps. The new method overcomes the shortcomings of the conventional methods, such that the registration is guaranteed to be diffeomorphic. 3.

Enforce the landmark constraints, by modifying the surface topologies. 4. Introduce a novel general methodology to achieve special goals in geometric processing by changing the surface Riemannian metrics.

4.2 Related Works

Shape matching and registration is a well-studied field with several recent books and surveys [16, 70]. It is out of scope for the this article to cover all existing shape matching and registration methods; we concentrate on inter-surface mapping based methods as well as various class of dense mapping methods.

Iterative closest points(ICP) based methods: The ICP based methods nd surface correspondences through an iterative procedure that starts with an initial correspondence and then repeatedly improves it by computing an aligning transformation from the correspondences and then updating the correspondences based on the transformation. These method are most commonly used for aligning surfaces related by a rigid transformation [11], but has also been used for moderate non-rigid deformations [4, 20, 104, 129, 43]. Unfortunately, it does guarantee that the final map is smooth or bijective (two points on one surface may map to the same point on another), and a good initial guess(which is sometimes difficult to obtain) is required to succeed in most cases.

Dense mapping methods: These kind of methods represent a map between a pair of shapes as a point-to-point correspondence. Since it is infeasible to optimize over such correspondences directly, most methods aim to obtain a sparse set of point correspondences and extend them to dense mappings [62, 153, 100, 73]. Because sparse point correspondences are inherently discrete, common ways to enforce global consistency include preservation of various quantities between pairs or sets of points, including geodesic distances [16, 62], various spectral quantities [63, 94, 96, 119, 100], or a combination of multiple geometric and topological tests [36, 6].

Inter-surface mapping: Given a set of correct sparse correspondences (defined by a user or an algorithm), one can use a variety of methods to find a smooth map interpolating them. A common approach is to map both surfaces to a canonical domain where sparse feature points align and then interpolate the map in that domain [3]. For example, [107] used a base coarse mesh (provided by a user) as such a domain. In their approach, the surface is cut into triangular patches defined by three geodesic curves, such that each geodesic curve is mapped to a triangle on a coarse base mesh. [117, 75] developed an automatic approach for creating the base domain. Conformal geometric methods based on the Euclidean metric have also been extensively studied [5, 151, 14, 145]. Wang et al. [141] studied brain morphology with Teichmüller space coordinates where the hyperbolic conformal mapping was computed with the Yamabe flow method. Zeng [151] proposed a general surface registration method via the Klein model in the hyperbolic geometry where they used the inversive distance curvature flow method to compute the hyperbolic conformal mapping.

Overall, finding diffeomorphic mappings between surfaces is an important but difficult

problem. In most cases, extra regulations, such as inverse consistency [120], have to be enforced to ensure a diffeomorphism. Since the proposed work offers a harmonic map based scheme for diffeomorphisms which guarantees a perfect landmark curve registration via enforced boundary matching, the novelty of the proposed work is that it facilitates diffeomorphic mapping between general surfaces with delineated landmark curves.

4.3 Theoretic Background

This section briefly covers the most relevant concepts and theorems, detailed treatments can be found in [32, 116, 151].

4.3.1 Algebraic Topology

Fundamental Group Let S be a surface, $q \in S$ is a base point. Consider all the loops through q. Two loops are homotopic, if one can deform to the other without leaving S. The product of two loops is the concatenation of them. All the homotopy classes of loops form the fundamental group (homotopy group), denoted as $\pi_1(S, q)$. Fig. 15 frame (a) shows a set of fundamental group generators.

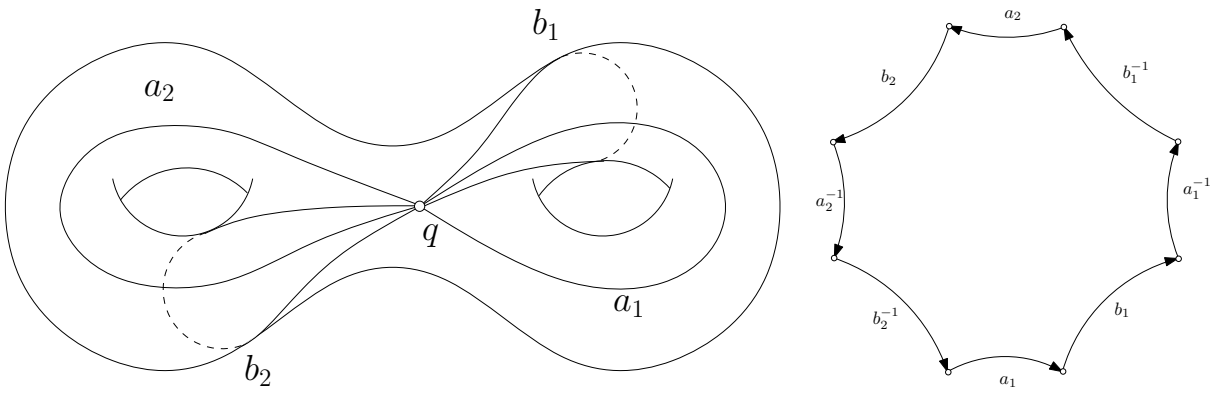

(a) fundamental group basis (b) fundamental domain

Figure 15: Canonical fundamental group basis and a fundamental domain.

Universal Covering Space Consider the set of all the homotopic classes of paths on the surface starting from p denoted as $\tilde{S}$, with an appropriate topology, $\tilde{S}$ forms a simply con-

nected surface. The projection map $\mathbf{p} : \tilde{S} \to S$ maps each path to its end point, the projection map is a local homeomorphism. The pair $(\tilde{S}, \mathbf{p})$ is called the *universal covering space* of S.

Let $q \in S$ be a point on the base surface, its preimage of the projection $\mathbf{p}$ is a discrete point set,

$$\mathbf{p}^{-1}(q) = \{\cdots, \tilde{q}_0, \tilde{q}_1, \cdots\}$$

which is called the *orbit* of q. Let $\tilde{D} \subset \tilde{S}$, $q \in S$ is an arbitrary point on the base surface S, if $\tilde{D}$ is simply connected and intersects the orbit of q at once, then $\tilde{D}$ is called a *fundamental domain*. Fig. 15 frame (b) shows a fundamental domain of a genus 2 surface. Fig. 16 show a finite portion of the universal covering space of a genus 3 surface.

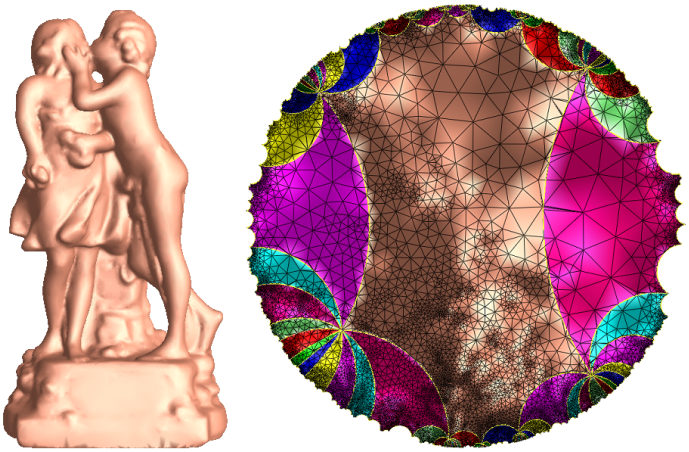

Figure 16: Finite portion of the universal covering space of a genus 3 surface.

Deck Transformation Let $\varphi : \tilde{S} \to \tilde{S}$ be a homeomorphism of the covering space $\tilde{S}$, which is commutable with the projection map, namely $\mathbf{p} \circ \varphi = \mathbf{p}$, then φ is called a *Deck transformation*. All the deck transformations form a group, which is denoted as $Deck(\tilde{S})$. Given a deck transformation φ, let $\tilde{q} \in \mathbf{p}^{-1}(q)$ be in the orbit of the base point q, then $\varphi(\tilde{q})$ is also in the orbit of q. Choose arbitrarily a path $\tilde{\gamma} \subset \tilde{S}$, connecting $\tilde{q}$ and $\varphi(\tilde{q})$, then the projection of $\tilde{\gamma}$ is a loop on S. This process gives an isomorphism between the fundamental group and the Deck transformation group, $\mathcal{F} : Deck(S) \ni \varphi \mapsto [\mathbf{p}(\tilde{\gamma})] \in \pi_1(S, q)$ We use α_k and β_k to denote the deck transformations, whose images under $\mathcal{F}$ are a_k and b_k

respectively. Therefore, formaly, the Deck transformation group has the representation

$$Deck(S) = \langle \alpha_1, \beta_1, \cdots, \alpha_g, \beta_g | \alpha_1 \beta_1 \alpha_1^{-1} \beta_1^{-1} \cdots, \alpha_g \beta_g \alpha_g^{-1} \beta_g^{-1} \rangle.$$

The transformations among the fundamental domains in Fig. 16 are Deck transformations.

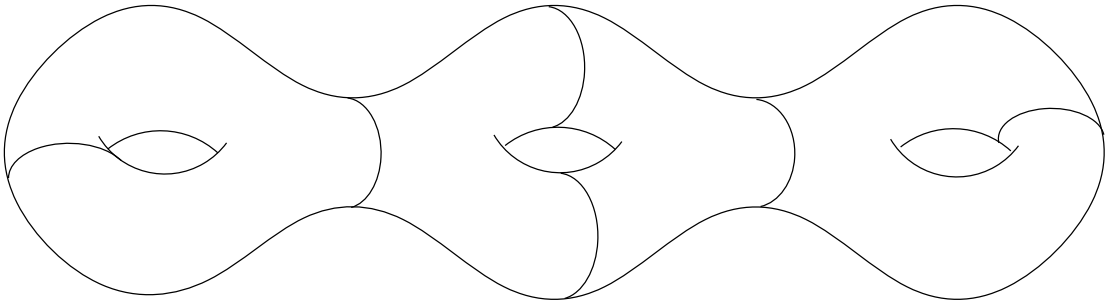

Figure 17: Pants decomposition of a genus 3 surface.

Pants Decomposition Suppose surface S is with the Euler characteristic number $\chi(S) < 0$. The surface can be decomposed to $|\chi(S)|$ pairs of pants. One pair of pants is a genus 0 surface with 3 boundaries. The pants decomposition [38] can be computed straight forwardly. Whenever there is a non-trivial loop γ on the surface, which is not homotopic to the boundary loops, the surface is sliced along γ. If the surface is divided to several connected-components, repeat this procedure, until all components are pairs of pants. Figure 17 shows one example of pants decomposition of a genus 3 surface.

4.3.2 Surface Differential Geometry

Isothermal Coordinates Suppose S is a surface embedded in $\mathbb{R}^3$ with a Riemannian metric $\mathbf{g}$ induced from the Euclidean metric. Let $u : S \to \mathbb{R}$ be a scalar function on S. It can be verified that $\tilde{\mathbf{g}} = e^{2\lambda}\mathbf{g}$ is also a Riemannian metric on S and angles measured by $\mathbf{g}$ are equal to those measured by $\tilde{\mathbf{g}}$. Thus, $\tilde{\mathbf{g}}$ is called a *conformal deformation* of $\mathbf{g}$, or a *conformal metric*.

Definition 4.1 (Isothermal Coordinates)**.** *Let S be a smooth surface with a Riemannian metric $\mathbf{g}$. Isothermal coordinates (x, y) for $\mathbf{g}$ satisfy $\mathbf{g} = e^{2\lambda(x,y)}(dx^2 + dy^2)$.*

where λ is the conformal factor. Locally, isothermal coordinates always exist. An atlas consisting of isothermal parameter charts is called a *conformal atlas*, or a *conformal structure*.

The Gaussian curvature[32] of the surface is given by

$$K(x, y) = -\Delta_{\mathbf{g}}\lambda, \tag{4.1}$$

where $\Delta_{\mathbf{g}} = e^{-2\lambda(x,y)}(\frac{\partial^2}{\partial x^2} + \frac{\partial^2}{\partial y^2})$ is the Laplace-Beltrami operator induced by $\mathbf{g}$. Although the Gaussian curvature is intrinsic to the Riemannian metric, the total Gaussian curvature is a topological invariant:

Theorem 4.2. *The total Gaussian curvature of a closed metric surface is* $\int_S KdA = 2\pi\chi(S)$, *where* $\chi(S)$ *is the Euler number of the surface[32].*

Harmonic Map For a surface S with a Riemannian metric $\mathbf{g}$, one can choose its isothermal coordinates (x, y) and have

$$\mathbf{g} = \sigma(x, y)(dx^2 + dy^2) = \sigma(z)dzd\bar{z},$$

where the complex parameter $z = x + iy$, $dz = dx + idy$.

Given a mapping $f : (M, \mathbf{g}_m) \to (N, \mathbf{g}_n)$, z and w are local isothermal parameters on M and N respectively; $\mathbf{g}_m = \sigma(z)dzd\bar{z}$ and $\mathbf{g}_n = \rho(w)dwd\bar{w}$. Then the mapping has local representation $w = f(z)$ or denoted as $w(z)$. We also name M as the *source surface* and N as the *target surface*.

Definition 4.3 (Harmonic Map)**.** *The* harmonic energy *of the mapping is defined as*

$$E(f) = \int_M \rho(w(z))(|w_z|^2 + |w_{\bar{z}}|^2)dxdy. \tag{4.2}$$

where the complex differential operator is defined as

$$\frac{\partial}{\partial z} = \frac{1}{2}(\frac{\partial}{\partial x} - i\frac{\partial}{\partial y}), \frac{\partial}{\partial \bar{z}} = \frac{1}{2}(\frac{\partial}{\partial x} + i\frac{\partial}{\partial y}).$$

If f *is a critical point of the harmonic energy, then* f *is called a* harmonic map.

Harmonic energy depends on the Riemannian metric on the target surface, and the conformal structure of the source surface. Namely, if the Riemannian metric on the source surface is deformed conformally, the energy does not change. The necessary condition for f to be a harmonic map is the following Euler-Lagrange equation

$$w_{z\bar{z}} + \frac{\rho_w}{\rho}w_z w_{\bar{z}} \equiv 0. \tag{4.3}$$

Harmonic maps can be defined on general surfaces. For surfaces with negative Euler number, it induces negative Gaussian curvature. The following theorem [115] shows that there is a special property with the induced hyperbolic harmonic map.

Theorem 4.4 (Yau). *Suppose $f : (M, \mathbf{g}_m) \to (N, \mathbf{g}_n)$ is a degree one harmonic map, furthermore the Riemannian metric on N induces negative Gaussian curvature, then for each homotopy class, the harmonic map is unique and diffeomorphic.*

The theory on the existence, uniqueness and regularity of harmonic maps have been thoroughly discussed in [115].

Klein-Poincaré Uniformization Theory Given a surface S with a Riemannian metric $\mathbf{g}$, there exist an infinite number of metrics conformal to $\mathbf{g}$. The Klein-Poincaré uniformization theorem states that, among all conformal metrics, there exists a unique representative, which induces constant Gaussian curvature everywhere. Moreover, the constant will be one of $\{+1, 0, -1\}$. Therefore, we can embed the universal covering space of any closed surface using its uniformization metric onto one of the three canonical surfaces: the *sphere* $\mathbb{S}^2$ for genus-0 surfaces with positive Euler numbers, the *plane* $\mathbb{E}^2$ for genus-1 surfaces with zero Euler number, and the *hyperbolic space* $\mathbb{H}^2$ for high genus surfaces with negative Euler numbers.

Surface Ricci Flow Surface uniformization metric can be computed using Ricci flow method.

Definition 4.5 (Surface Ricci Flow). *The normalized surface Ricci flow is defined as $\frac{d\mathbf{g}(t)}{dt} = 2\left(\frac{2\pi\chi(S)}{A(0)} - K(t)\right)\mathbf{g}(t)$ where $\chi(S)$ is the Eulder characteristic number of S, $A(0)$ is the total area of the surface at time 0, $K(t)$ is the Gaussian curvature induced by $\mathbf{g}(t)$.*

Theorem 4.6 (Hamilton). *If $\chi(S) < 0$, then the solution to the normalized Ricci flow equation exists for all $t > 0$ and converges to a metric with constant curvature $\frac{2\pi\chi(S)}{A(0)}$.*

By running Ricci flow, a hyperbolic metric of the surface can be obtained, which induces -1 Gaussian curvature everywhere.

4.3.3 Hyperbolic Geometry

Hyperbolic Plane and Fuchs Group The Poincaré's disk model for the hyperbolic plane $\mathbb{H}^2$ is the unit disk on the complex plane $\{z \in \mathbb{C} | \, |z| < 1\}$ with Riemannian metric $(1 - z\bar{z})^{-2} dz d\bar{z}$. The hyperbolic distance between two points $z_1, z_2 \in \mathbb{H}^2$ is given by $\rho(z_1, z_2) = \tanh^{-1}\left|\frac{z_1 - z_2}{1 - z_1\bar{z}_2}\right|$. The geodesics (*hyperbolic lines*) are circular arcs perpendicular to the unit circle. The hyperbolic rigid motions are Möbius transformations $\varphi : z \mapsto e^{i\theta}\frac{(z - z_0)}{(1 - \bar{z}_0 z)}$. Fig. 18 shows one example of Möbius transformation of the unit disk. The *axis* of ϕ is the hyperbolic line through its fixed points: $z_1 = \lim_{n\to\infty}\varphi^n(z), z_2 = \lim_{n\to\infty}\varphi^{-n}(z)$. The hyperbolic line through z_1 and z_2 is called the *axis* of the Möbius transformation. Given two non-intersecting hyperbolic lines γ_1 and γ_2, there exists a unique hyperbolic line τ orthogonal to both of them, and gives the shortest path connecting them. For each γ_k, there is a unique reflection ϕ_k whose axis is γ_k, then the axis of $\phi_2 \circ \phi_1^{-1}$ is τ.

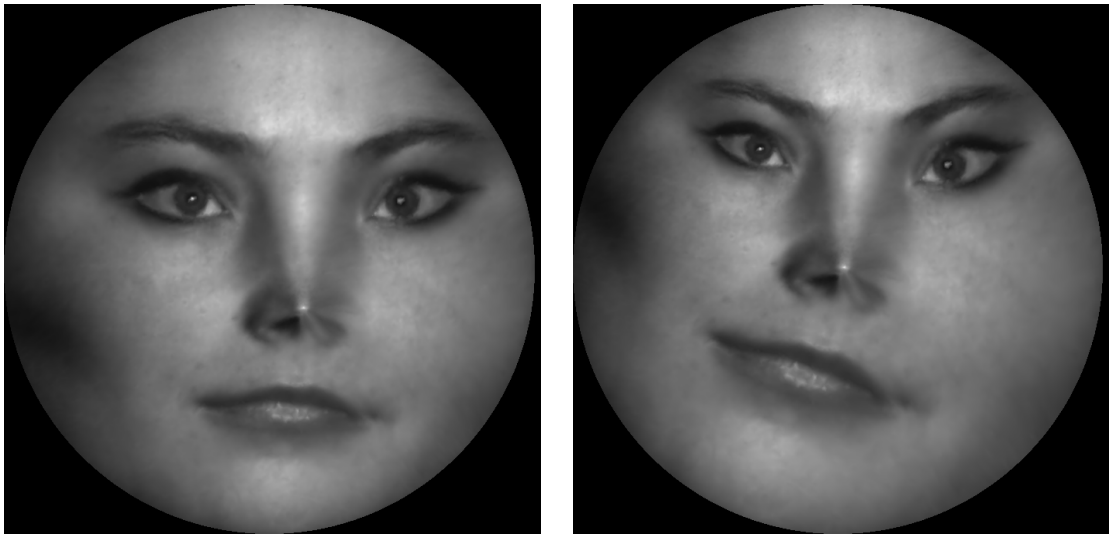

Figure 18: Möbius transformation.

Suppose S is with a hyperbolic metric, then its universal covering space $\tilde{S}$ can be isometrically embedded onto the hyperbolic plane $\mathbb{H}^2$. A *Fuchsian transformation* ϕ is a Möbius transformation, which preserves the projection $\phi \circ p = p$. All Fuchsian transformations form the *Fuchs group*, $Fuchs(S)$, which is isomorphic to the fundamental group $\pi_1(S, q)$.

Complex Cross Ratio Suppose z_1, z_2, z_3, z_4 are points in $\mathbb{C} \cup \{\infty\}$,

Definition 4.7 (Cross Ratio)**.** *The complex cross ratio is given by* $(z_1, z_2, z_3, z_4) := \frac{z_1 - z_3}{z_1 - z_4} : \frac{z_2 - z_3}{z_2 - z_4}$.

Complex cross ratio is invariant under Möbius transformations. Namely, if φ is a Möbius transformation, then $(\varphi(z_1), \varphi(z_2), \varphi(z_3), \varphi(z_4)) = (z_1, z_2, z_3, z_4)$.

Exponential Map Let z be a point on the Poincaré disk, the tangent space at z is denoted as $T_z\mathbb{H}^2$. Suppose $v \in T_z\mathbb{H}^2$ is a tangent vector at z, there is a unique geodesic $\gamma(t)$, such that $\gamma(0) = z, \dot{\gamma}(0) = v$, then the *exponential map* at z, $\exp(\cdot, z) : T_z\mathbb{H}^2 \to \mathbb{H}^2$ is

$$\exp(v, z) := \gamma(1). \tag{4.4}$$

The *logarithm map* is the inverse to the exponential map, the logarithm at the origin 0, $\log(\cdot, 0) : \mathbb{H}^2 \to T_0\mathbb{H}^2$,

$$\log(w, 0) := \rho(w, 0)\frac{w}{|w|}. \tag{4.5}$$

where $\rho(w, 0)$ is the hyperbolic distance between the origin and w. Fig. 19 illustrates the exponential map on a Riemannian manifold.

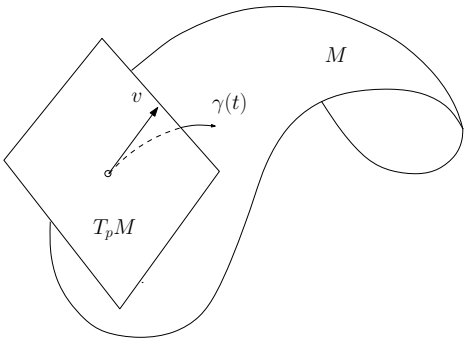

Figure 19: Exponential map.

Geodesic Mass Center Given a surface with a metric $(S, \mathbf{g})$, fix a point $p \in S$, the exponential map at p is diffeomorphic on a small disk at T_pS. The supreme of the such a disk radius is called the *injective radius* at p.

suppose $Q = \{q_1, q_2, \cdots, q_k\} \subset S$ is a point set in a geodesic disk $D(p, r)$, whose radius r is smaller than the injective radius at p. The points are associated with the weights $\Lambda = \{\lambda_1, \lambda_2, \cdots, \lambda_k\}$, each $\lambda_i \geq 0$, then the *weighted geodesic mass center* of (Q, Λ) is defined as $c(Q, \Lambda) := argmin_q \sum_{i=1}^{k} \lambda_j \rho^2(q, q_i)$. Then from Riemannian geometry, the mass center exists and is unique.

Klein's Model Another hyperbolic plane model is the *Klein's disk model*, where the hyperbolic lines coincide with Euclidean lines. The conversion from Poincare's disk model to Klein disk model is given by

$$z \to \frac{2z}{(1 + z\bar{z})}. \tag{4.6}$$

Hyperbolic Pants Decomposition Suppose S has a hyperbolic metric, one can compute a pants decomposition, such that all the cutting loops are geodesics. Furthermore, each pair of hyperbolic pants can be further decomposed. Assume the pair of pants have three geodesic boundaries $\{\gamma_i, \gamma_j, \gamma_k\}$. Let $\{\tau_i, \tau_j, \tau_k\}$ be the shortest geodesic paths connecting each pair of them. The shortest paths divide the surface to two identical hyperbolic hexagons with right inner angles. when mapped to the Klein's model, the hyperbolic hexagons coincide with convex Euclidean hexagons. Fig. 20 shows the decomposition of a pair of hyperbolic pants.

4.4 Algorithms

In this section, we introduce our hyperbolic harmonic mapping method. For comparison purpose, we will also briefly explain how to compute the constrained Euclidean harmonic

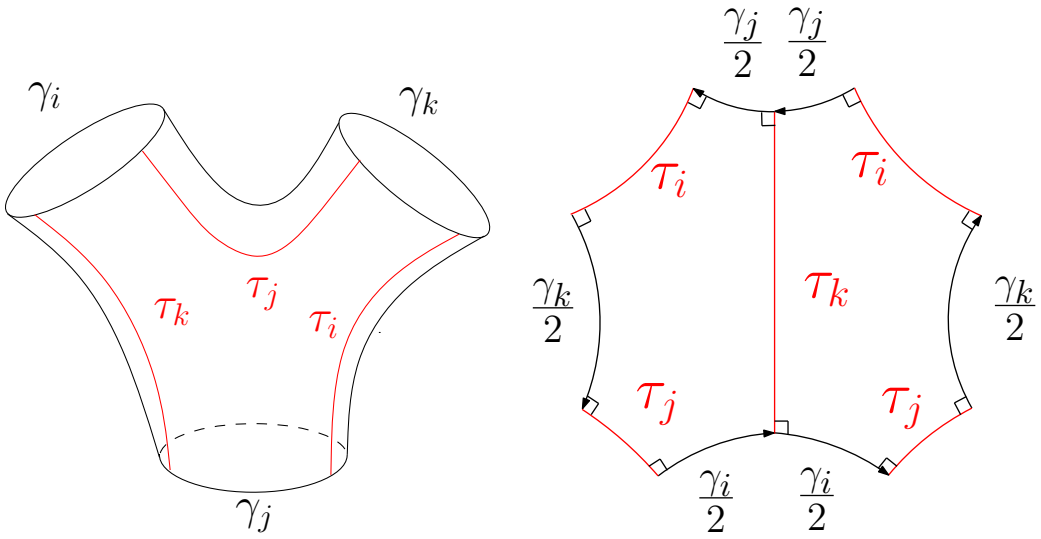

Figure 20: A pair of hyperbolic pants is decomposed to two hyperbolic hexagons.

mapping with the same framework. Fig. 21 illustrates the major steps for us to compute hyperbolic harmonic maps between surfaces.

4.4.1 Topology Optimization

In surface registration, sometimes one may define landmark curves and enforce the landmark curve matching to increase the global surface registration accuracy [130, 103] Since harmonic map depends on boundary conditions, it is natural to model landmark as boundaries by cutting surfaces along landmark curves. Later, in our harmonic mapping, these landmark curves are enforced to match as boundary conditions. We call this step as *topology optimization* and used it in some of our previous works [145, 146].

4.4.2 Discrete Hyperbolic Ricci Flow

Let M be a two-dimensional mesh surface, we denote the set of vertices, edges and faces by V, E, F respectively. Each face is a hyperbolic triangle, the edge lengths and corner angles are related by the *hyperbolic cosine law*. Assume the angles in face v_i, v_j, v_k are $\theta_i, \theta_j, \theta_k$, the edge lengths against them are l_i, l_j, l_k, then

$$\cosh l_k = \cosh l_i \cosh l_j - \sinh l_i \sinh l_j \cos \theta_k.$$

Furthermore, each vertex v_i is associated with a hyperbolic circle with radius γ_i.

Algorithm 3 Surface Hyperbolic Harmonic Mapping Algorithm Pipeline.

1. Construct an initial mapping.
2 Topology optimization for landmark curve constraints.
3. Compute the hyperbolic metric using hyperbolic Ricci flow.
4. Hyperbolic pants decomposition, isometrically embed them to the Poincaré disk and then map them to the Klein model.
5. Compute harmonic maps using Euclidean metrics between corresponding pairs of pants, with consistent boundary constraints.
6. Use nonlinear heat diffusion to improve the mapping to a global hyperbolic harmonic map on the Poincaré disk model.

A *discrete metric* is a function $l : E \to \mathbb{R}^+$, such that triangle inequality holds on every face, which represents the edge lengths. We set the target Gauss curvature for each interior vertex to be -1, and for each boundary vertex to be zero. Then compute the hyperbolic metrics of using discrete hyperbolic Ricci flow method [151]. The *discrete hyperbolic Ricci flow* is defined as $\frac{du_i}{dt} = -K_i$, The detailed computational algorithm of hyperbolic ricci flow can be found in [151].

4.4.3 Hyperbolic Pants Decomposition

Suppose the input surface S is with a hyperbolic metric g. The hyperbolic pants decomposition is accomplished by divide-conquer method.

First, we compute the fundamental group generators of S using the method described in [51], if the generators include a loop γ which is not an boundary loop, we slice S along γ. If γ divides S to two connected components S_1 and S_2, we repeat the same procedure on each component. Otherwise, we continue this process, until the surface is decomposed to $S = \cup_k S_k$, where is S_k is a genus 0 surface with multiple boundaries.

Second, if a component S_k has 3 boundary loops, then it is a pair of pants. Otherwise if S_k has more than 3 boundaries, $\partial S_k = \gamma_0 + \gamma_1 + \gamma_2 \cdots$, compute the product of γ_0 and γ_1, $\gamma = \gamma_0 \cdot \gamma_1$, slice S_k along γ, to get two connected components S_k^1 and S_k^2, such that the boundary of S_k^1 consists of γ_0, γ_1 and γ. Hence S_k^1 is a pair of pants. Continue the procedure on S_k^2. By repeating this process, eventually, all connected components are pairs of pants. Namely, we have topologically decomposed S pairs of pants.

Third, for each cutting loop $\gamma \subset S$, we compute the unique hyperbolic geodesic homotopic to γ. We find all the triangular faces attaching to γ. For each vertex v_i, we define its

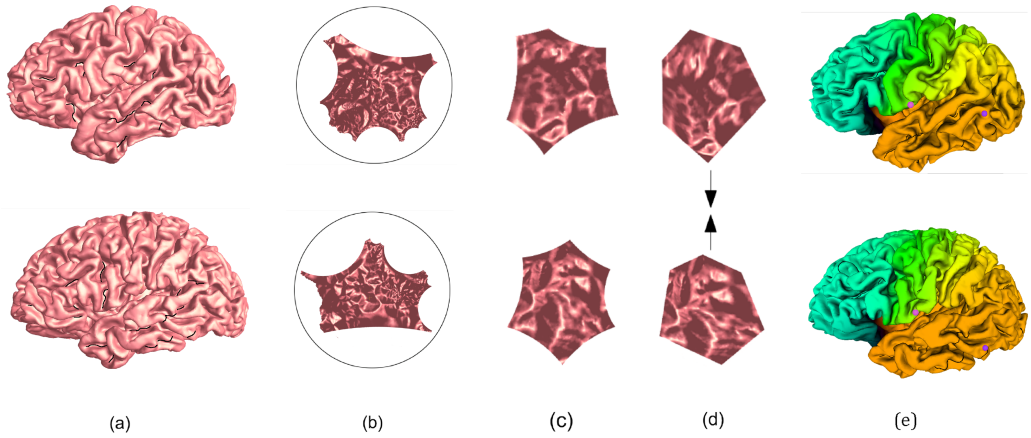

Figure 21: Algorithm Pipeline (suppose we have 2 brain surfaces M and N as input): (a). The input brain models M and N, with landmarks been cut open as boundaries. (b). Hyperbolic embedding of M and N on the Poincaré disk. (c). Decompose M and N into multiple pants, and each pant further decomposed to 2 hyperbolic hexagons. (d). Hyperbolic hexagons on Poincaré disk become convex hexagons under Klein model, then a one-to-one map between the correspondent parts of M and N can be obtained via the constrained Euclidean harmonic map. Then we can apply our hyperbolic heat diffusion algorithm to get a global hyperbolic harmonic diffeomorphism. (e). Color coded registration result of M and N.

one-ring neighborhood as $N(v_i)$,

$$N_i = \bigcup_{v_j, v_k \in V} [v_i, v_j, v_k].$$

Suppose the vertices on γ is sorted consecutively as $\{v_0, v_1, \cdots, v_{n-1}$. We isometrically embed N_k onto the hyperbolic disk $\mathbb{H}^2$, the embedding is denoted as τ_k. Suppose a face f is shared by two neighborhoods N_{k-1} and N_k, then there is a unique Möbius transformation φ_k, which maps $\tau_{k-1}(f)$ to $\tau_k(f)$. Then we can glue the embedding $\tau_{k-1}(N_{k-1})$ and $\tau_k(N_k)$. After embedding the neighborhood of the last vertex N_{n-1}, we can continue embedding the neighborhood of the first vertex N_0 again. Eventually, we flatten the neighborhood of γ onto $\mathbb{H}^2$. The neighborhood of the starting vertex v_0 has been isometrically embedded twice, the two embedding differ by a Möbius transformation φ. Then φ is the Fuchsian transformation in $Fuch(S)$ corresponding to the homotopy class of γ in the fundamental group, $[\gamma] \in \pi_1(S, q)$. We can find the two fixed points of φ, the hyperbolic line through the two fixed points is the unique geodesic homotopic to γ. By performing this procedure, we can use hyperbolic lines to replace all the cutting loops in the pants decomposition.

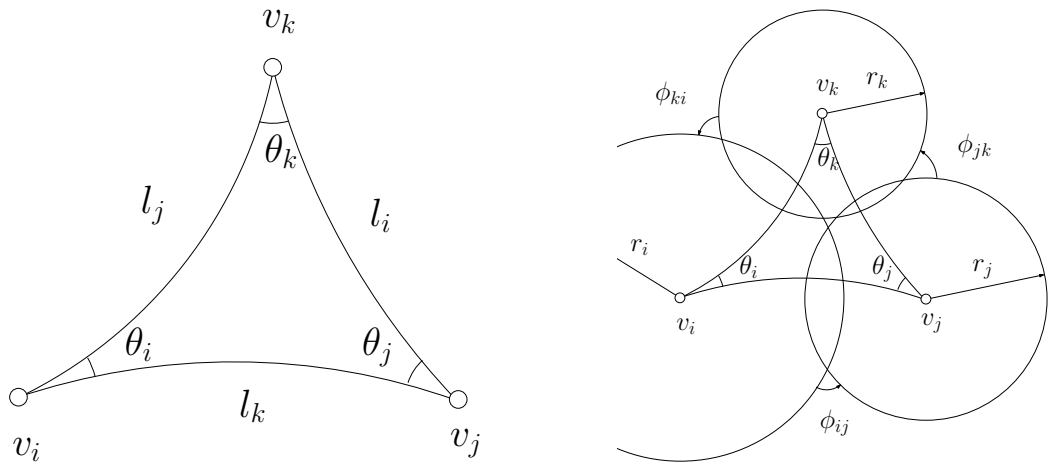

(a) hyperbolic triangle (b) circle packing

Figure 22: Hyperbolic triangle and the hyperbolic circle packing.

Algorithm 4 Topological Pants Decomposition.

Input: Arbitrary surface S with B boundaries.

Output: Pants decomposition of S.

1. Ignore the boundaries and decompose the surface into genus zero patches with multiple boundaries, then for each patch M perform the following steps.
2. Put all boundaries γ_i of M into a queue Q.
3. If Q has < 3 boundaries, end; else goto Step 2.
4. Compute a geodesic loop γ' homotopic to $\gamma_i \cdot \gamma_j$
5. γ', γ_i and γ_j bound a pants patch, remove this pants patch from M. Remove γ_i and γ_j from Q. Put γ' into Q. Go to Step 1.

Algorithm 5 Hyperbolic Geodesic.

Input: A triangle mesh S with hyperbolic metric $\mathbf{g}$, a loop γ

Output: The hyperbolic geodesic loop homotopic to γ.

1. Sort the vertices in the loop as $\{v_0, v_1, \cdots, v_{n-1}\}$.
2. Isometrically embed the one-ring neighborhood of each $v_k \in \gamma$, N_k. The embedding is denoted as $\tau_k : N_k \to \mathbb{H}^2$.
3. for each $k = 0, 1, \cdots, n-1$, find a face $f \in N_k \cap N_{k+1}$, find the Möbius transformation φ_k to map $\tau_{k+1}(f)$ to $\tau_k(f)$. Transform $\tau_k(N_k)$ by φ_k, this glues the embedding of N_{k+1} to the embedding of N_k.
4. The one-ring neighborhood N_0 has two embedding, τ_0 and τ_n. The composition $\varphi = \tau_n^{-1} \circ \tau_0$ is a Möbius transformation.
5. Compute the two fixed points of φ, $\varphi^{\infty}(0)$ and $\varphi^{-\infty}(0)$. The hyperbolic line through these two points is the axis of φ, which is the desired geodesic.

4.4.4 Constructing the Initial Mapping

This step has several stages: first each pair of pants are decomposed to two identical hyperbolic hexagons; second, then hyperbolic hexagons are isometrically embedded onto the Poincaré disk, then converted to hexagons on Klein model; finally the hexagons on Klein disk are treated as Euclidean polygons, the corresponding hexagons are registered using Euclidean harmonic maps with consistent boundary constraints. The resultant piecewise harmonic mapping is the initial mapping.

For the first stage, we use the method described in the theory section to find the shortest path between two boundary loops. Assume a pair of hyperbolic pants M with three geodesic boundaries $\{\gamma_i, \gamma_j, \gamma_k\}$. On the universal covering space $\tilde{M}$, γ_i and γ_j are lifted to hyperbolic lines, $\tilde{\gamma}_i$ and $\tilde{\gamma}_j$ respectively. There are reflections $\tilde{\phi}_i$ and $\tilde{\phi}_j$, whose symmetry axis are $\tilde{\gamma}_i$ and $\tilde{\gamma}_j$. Then the axis of the Möbius transformation $\tilde{\gamma}_j \circ \tilde{\gamma}_i^{-1}$ corresponds to the shortest geodesic path τ_k between γ_i and γ_j. By cutting τ_i,τ_j and τ_k we further decomposed a pair of pants to two hyperbolic hexagons.

In the second stage, each hyperbolic hexagon on the Poincaré disk is transformed to a convex hexagon in Klein's disk using Eqn. 4.6. Then a planar harmonic map between two corresponding planar hexagons is established by solving Laplace equation with Dirichlet boundary conditions [1],

$$w_{z\bar{z}} \equiv 0. \tag{4.7}$$

Specifically, we use the cotangent formula [37, 45] to solve the Dirichlet problem. Given a face $[v_i, v_j, v_k]$, the corner angle θ_k^{ij} at v_k in $[v_i, v_j, v_k]$the corner angle at v_k is denoted as θ_k^{ij}. The *cotangent edge weight* for an edge $[v_i, v_j]$ is given by

$$k_{ij} := \begin{cases} \cot\theta_k^{ij} + \cot\theta_l^{ji} & [v_i, v_j] \subset [v_i, v_j, v_k] \cap [v_j, v_i, v_l] \\ \cot\theta_k^{ij} & [v_i, v_j] \subset [v_i, v_j, v_k], [v_i, v_j] \subset \partial S \end{cases}$$

A Harmonic map minimizes the harmonic energy, by Finite Element Method, the harmonic energy for a map $f : S \to \mathbb{E}^2$ is given by $E(f) = \frac{1}{2}\sum_{[v_i,v_j]\in S} k_{ij} \left|f(v_i) - f(v_j)\right|^2$.
From the optimality condition, one can get the discrete Laplace equation. Given a mapping for each interior vertex $v_i \notin \partial S$,

$$\Delta f(v_i) := \sum_{[v_i,v_j]\in S} k_{ij}(f(v_j) - f(v_i)) = 0, \tag{4.8}$$

where Δ is the discrete Laplace-Beltrami operator. This is equivalent to the *mean value* property of a harmonic map f: $f(v_i)$ coincides with the *weighted mass center* of its neighbors,

$$f(v_i) := \frac{\sum_{[v_i,v_j]\in S} k_{ij} f(v_j)}{\sum_{[v_i,v_j]\in S} k_{ij}}, \tag{4.9}$$

The right hand side is the weighted mass center.

The Dirichlet boundary condition is as follows. The mapping maps hexagon vertices to vertices, boundary line segments to line segments. Restricted on one boundary line

segment, the mapping is a linear interpolation by arc length parameter. Because the edge lengthes of the cut landmarks are the same (they were originally the set of edges), the position constrain patterns are exactly the same for two adjacent patches which share this landmark. By solving sparse linear system, we can get a piecewise harmonic mapping between the surfaces.

It is well known that if the target mapping domain is convex, then planar harmonic maps are diffeomorphic [116]. The consistent boundary conditions ensure that the harmonic mappings between hexagons can be glued together to form a homeomorphic initial mapping. The process is visualized in Figure 23.

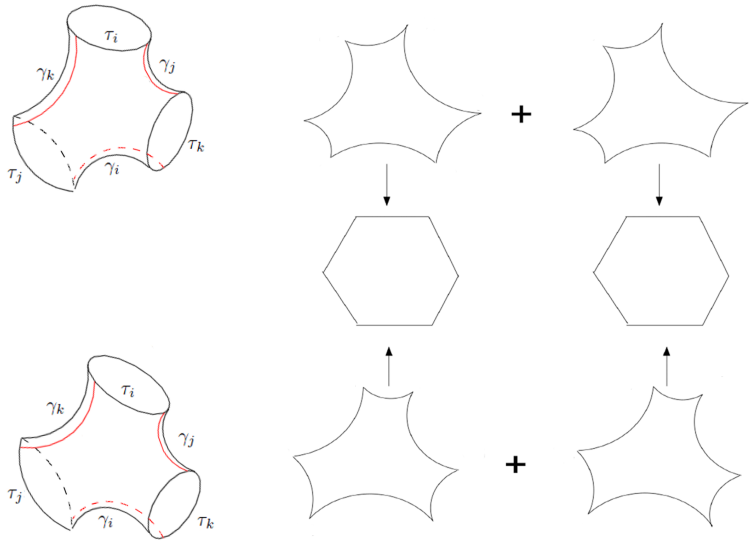

Figure 23: Hyperbolic hexagon matching.

4.4.5 Non-linear Heat Diffusion

The goal of this step is to diffuse the initial mapping and achieve a global hyperbolic harmonic map which is not restricted on every patch, as used in the prior step. Similar to how the Eikonal equation is solved in fast marching algorithm [118, 136], here a nonlinear heat diffusion method is proposed to compute the harmonic mapping, which is based on a conformal atlas induced by the hyperbolic metric.

Algorithm 6 Hyperbolic Hexagon Matching Algorithm.

Input: Two hyperbolic hexagons H_1 and H_2.

Output: A diffeomorphism maps H_1 to H_2.

1. Convert H_1 and H_2 from the Poincaré disk model to the Klein model, in which they become convex polygons H_1' and H_2'.
2. Set Dirichlet boundary condition by linearly interpolating the boundary line segments using arc length parameters.
3. Compute a harmonic map between H_1' and H_2', then construct a mapping the between original H_1 and H_2.

Hyperbolic Atlas Let $(S, \mathbf{g})$ be a dense triangle mesh with hyperbolic metric $\mathbf{g}$. Then for each vertex $v_i \in S$, the one ring neighboring faces form a neighborhood N_i, the union of N_i's cover the whole mesh, $S \subset \bigcup_{v_i \in S} N_i$. Isometrically embed N_i to the Poincaré's disk $\phi_i : N_i \to \mathbb{H}^2$, then $\{(N_i, \phi_i)\}$ form a conformal atlas. Furthermore, the chart transitions are Möbius transformations. All the following computations are carried out on local charts of the conformal atlas. The computational result is independent of the choice of local parameters.

Suppose $f : (S_1, \mathbf{g}_1) \to (S_2, \mathbf{g}_2)$ is the initial map, $\mathbf{g}_1$ and $\mathbf{g}_2$ are hyperbolic metrics. Compute the conformal atlases of S_1 and S_2. Choose local conformal parameters z and w for S_1 and S_2, f has local representation $f(z) = w$, or simply $w(z)$.

Map Representation Suppose v is a vertex on S_1, with local representation z, its image $w(z)$ is inside a triangular face $t(v)$ of S_2. Suppose the three vertices of $t(v)$ have local representations w_i, w_j, w_k, the we compute the *complex cross ration*

$$\eta(v) := (w(z), w_i, w_j, w_k) .$$

The image of v is then represented by the pair $[t(v), \eta(v)]$. Note that, all the local coordinates transitions in the conformal chart of S_1 and S_2 are Möbius transformations, and the cross ration η is invariant under Möbius transformation, therefore, the representation of the mapping $f : v \to [t(v), \eta(v)]$ is independent of the choice of local coordinates.

Hyperbolic Harmonic Map Let $f : (S_1, \mathbf{g}_1) \to (S_2, \mathbf{g}_2)$ be a mapping, the discrete harmonic energy is similar to the Euclidean one 4.4.4,

$$E(f) = \frac{1}{2} \sum_{[v_i, v_j] \in S_1} k_{ij} \rho^2(f(v_i), f(v_j)). \tag{4.10}$$

where $\rho(f(v_i), f(v_j))$ is the hyperbolic distance between $f(v_i)$ and $f(v_j)$. By definition, if f is harmonic, then for an arbitrary vertex v_i, fixing all the other vertices, the following energy should be minimized:

$$\min_{f(v_i)} \sum_{[v_i,v_j]\in S_1} k_{ij}\rho^2(f(v_i), f(v_j)), \tag{4.11}$$

therefore, the harmonic map f satisfies the *mean value property*: for each vertex v_i, its image coincides with the weighted geodesic mass center of the images of its neighbors.

Namely, let v_i be a vertex, its one-ring neighbors are $\{v_{i_1}, v_{i_2}, \cdots, v_{i_k}\}$. Let $Q(v_i) = \{f(v_{i_1}), f(v_{i_2}), \cdots, f(v_{i_k})\}$, and weights $\Lambda(v_i) = \{k_{i,i_1}, k_{i,i_2}, \cdots, k_{i,i_k}\}$, then $f(v_i) = c(Q(v_i), \Lambda(v_i))$, where the right hand side weighted geodesic mass center is defined in Eqn.4.9.

Weighted Geodesic Mass Center Given a point set $Q = \{z_1, z_2, \cdots, z_k\}$ and weights $\Lambda = \{\lambda_1, \cdots, \lambda_k\}$ on Poincaré's disk, denote the weighted geodesic mass center $c(Q, \Lambda)$ as c. It can be computed by the following iterations.

At the initial step, set $Q_0 = Q$, set c_0 be a point in the convex hull of Q_0. At the n-th step, apply a Mobiüs transformation to Q_n. $\varphi_n(z) = \frac{z-c_n}{1-\bar{c_n}z}$, Set $z_i^{n+1} = \varphi_n(z_i^n)$, $Q_{n+1} = \{z_1^{n+1}, z_2^{n+1}, \cdots, z_k^{n+1}\}$.

compute the logarithms of z_i^{n+1}'s using Eqn.4.5. In the tangent plane at the origin, compute the Euclidean weighted mass center $C := \frac{\sum_i \lambda_i \log z_i^{n+1}}{\sum_i \lambda_i}$. Compute the exponentional map of C using Eqn.4.4, update the center $c_{n+1} \leftarrow \exp(C, 0)$. Repeat this procedure, then the sequence $\{c_n\}$ converges, $\{z_i^n\}$ converges for all $1 \le i \le k$. Then the limit c_∞ is the weighted geodesic mass center of the point set Q_∞ with weights Λ. Detailed algorithm description can be found in Alg.7.

Non-linear Heat Diffusion The initial map $f : S_1 \to S_2$ can be diffused to be harmonic using the non-linear heat diffusion process.

For each vertex v_i, we compute the weighted geodesic mass center of the images of its neighboring vertices $c(Q(v_i), \Lambda(v_i))$, then update the image of v_i to be the mass center, $f(v_i) \leftarrow c(Q(v_i), \Lambda(v_i))$. Update the images of all vertices on S_1. Repeat this process, until for each vertex, the geodesic distance between its image, and the weighted geodesic mass center of the images of its neighbors is less than a given threshold.

4.4.6 Euclidean Harmonic Mapping with Hard Constraints

For comparison purpose, we also implement Euclidean harmonic mapping method with hard constraints for landmark matching [144]. Basically, for genus zero surfaces with one open boundary, we apply the Eqn. to map the surfaces to a unit disk.

Algorithm 7 Weighted Geodesic Mass Center.

Input: A point set $Q = \{z_1, z_2, \cdots, z_k\}$ on the Poincaré disk, the diameter of Q is less than the injective radius of S; A weight set $\Lambda = \{\lambda_1, \lambda_2, \cdots, \lambda_k\}$.

Output: The weighted geodesic mass center $c(Q, \Lambda)$.

1. Initialize $z_i^0 \leftarrow z_i$, $Q_0 \leftarrow \{z_i^0\}$, $c_0 \leftarrow 0$.

repeat

2. Set $\varphi_n \leftarrow (z - c_n)/(1 - \bar{c_n} z)$
3. Set $z_i^{n+1} \leftarrow \varphi_n(z_i^n)$, $Q_{n+1} \leftarrow \{z_i^{n+1}\}$.
4. Compute the logarithm of z_i^{n+1} using Eqn.4.5.
5. Compute the Euclidean weighted mass center in the tangent space at the origin $C \leftarrow (\sum_i \lambda_i \log z_i^{n+1})/(\sum_i \lambda_i)$.
6. Compute the exponential map of C using Eqn.4.4

$$c_{n+1} \leftarrow \tanh |C| \frac{C}{|C|}.$$

until $\rho(c_n, c_{n+1}) < \varepsilon$

7. Construct a Möbius transformation φ, mapping $\{z_1^n, z_2^n, z_3^n\}$ to $\{z_1, z_2, z_3\}$.
8. Return the weighted geodesic mass center $\varphi(c_n)$.

To enforce landmark curve matching, first, we use the unit speed parameterizations to build a one-to-one correspondence between a given landmark curves from different surfaces. Secondly, we select a surface and use its harmonic mapping image as the template surface and move landmark curves from other surfaces to the template landmark positions on the unit disk. We treat the landmark positions together with the boundary curves as the hard constraints and build a linear system with Dirichlet boundary condition as shown in Eqn. 6.13. After solving the linear system, we obtain the Euclidean harmonic map with hard constraints. Because of the Euclidean harmonic map nature, the obtained mapping is non-diffeomorphic. Fig 24 shows the Euclidean harmonic mapping pipeline for human face registration and the non-diffeomorphic effects around the constrained regions.

4.5 Experimental Results

In this section, we will report our hyperbolic harmonic mapping experimental results. We use a matching between the Eight and Amphora models to illustrate that our proposed method works for high genus surface matching applications. Furthermore, we study facial surface tracking and cortical surface registration applications. Extensive comparisons with Euclidean harmonic mapping are done and the results demonstrate the benefits for us to

Algorithm 8 Hyperbolic Heat Diffusion Algorithm.

Input: Two triangle meshes with hyperbolic metrics $(S_1, \mathbf{g_1})$ and $(S_2, \mathbf{g_2})$; an initial mapping $f : S_1 \to S_2$, represented as $(t(v_i), \eta(v_i))$, $\forall v_i \in S_1$. An error tolerance threshold ε.

Output: Discrete hyperbolic harmonic map $h : S_1 \to S_2$.

1. Construct a hyperbolic atlas of the target surface S_2.

repeat

  for each vertex $v_i \in S_1$ **do**

    Collect all its neighboring vertices $N(v_i) = \{v_{i_j}\}$ and neighboring edge weights $\Gamma(v_i) = \{k_{i,i_j}\}$.

    3. Choose a local chart of S_2, which covers the images of all neighboring vertices in $N(v_i)$.

    4. Convert the mapping representation of each $v_{i_j} \in N(v_i)$, $(t(v_{i_j}), \eta(v_{i_j}))$ to local coordinates w_{i_j}. Let $Q(v_i) = \{w_{i_j}\}$.

    5. Compute the weighted geodesic mass center $c(Q(v_i), \Gamma(v_i))$.

    6. Update $f(v_i)$, $f(v_i) \leftarrow c(Q(v_i), \Gamma(v_i))$. Convert $f(v_i)$ to the representation $(t(v_i), \eta(v_i))$.

  end for

until for all $v_i \in S_1$, $\rho(f(v_i), c(Q(v_i), \Lambda(v_i))) < \varepsilon$.

8. Output the harmonic map $f : S_1 \to S_2$, represented as $(t(v_i), \eta(v_i))$, $\forall v_i \in S_1$.

adopt hyperbolic harmonic mapping framework for surface registration research.

4.5.1 General Surface Registration

Our method is general and can handle general surface structure, i.e. surfaces with arbitrary holes and open boundaries. Here we show how it works on closed surface matching problem. Fig. 26 (a) and (b) show two genus-two surface models, Eight model and Amphora model. They are marked with a set of canonical fundamental group generators, which can cut the surface into a topological disk with eight sides. (c) and (d) illustrate the embedding of their fundamental domains to the Poincaré disk. Multiple fundamental domains are shown and each color labels a complete fundamental domain. As the rigid translation on the Poincaré disk, the Möbius transformation generates a new fundamental domain across each edge. Cutting along the yellows lines on (e) and (f) may decompose them into to two pairs of topological pant models. On each pair of pant model, it can be further cut into two symmetric pieces, each of which is labeled with a unique color in (g) and (h). The initial mapping is computed between these four pieces of two surfaces.

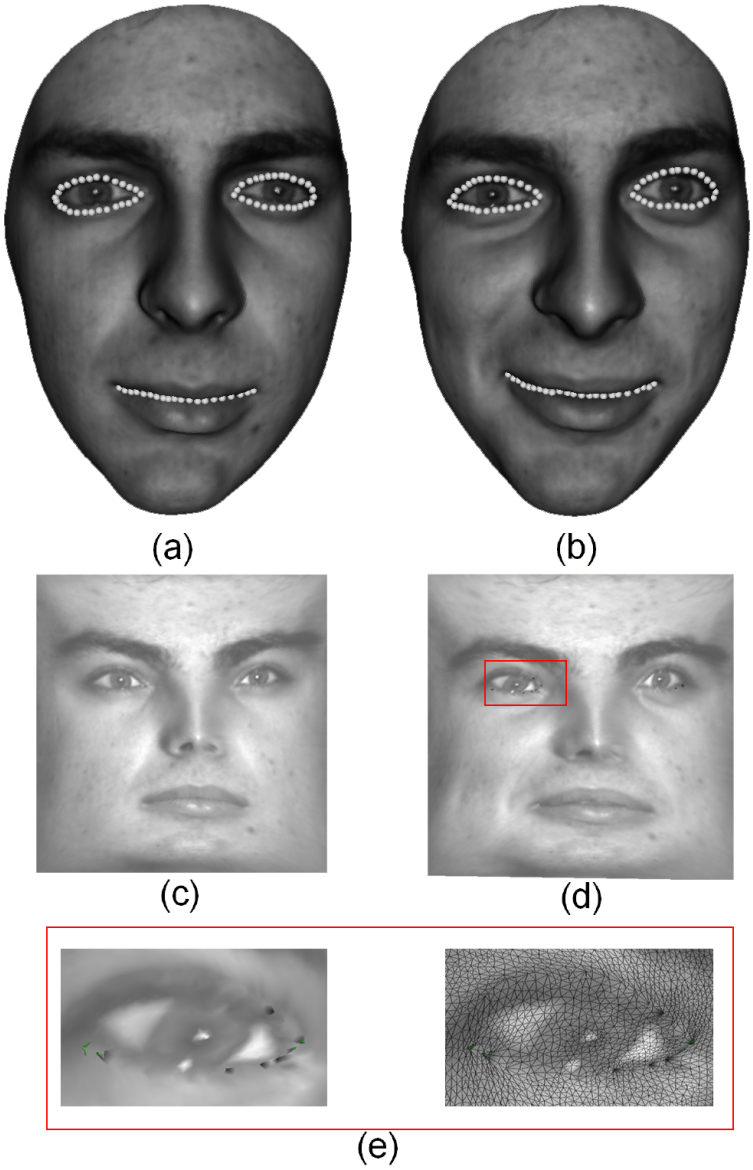

Figure 24: Euclidean harmonic mapping. (a) and (b) are the input face models. The Euclidean harmonic mapping method first map (a) to a rectangle, shown by (c), then map (b) to (c) with the constrain curves shown by the white balls. (d) shows the result of this constrained mapping, (e) shows that there are flipping at the constrained region.

Fig. 27 further illustrates the matching process. For each pair of pant surface (shown in (a) and (b)), it may decompose two pieces and they are mapped to two hexagon models on the Poincaré disk. (c) and (d) show two hexagons model on the Poincaré model. With Eqn. 4.6, one may convert them to two convex hexagons on the Klein model ((e) and (f)).

Note that the geodesics on the Poincaré model are arc while they are straight lines on the Klein model. So the hexagons are convex on the Klein model. Initial mapping are computed between the convex hexagons. Following that, non-linear heat diffusions are computed throughout the entire surfaces and the final hyperbolic harmonic mapping results are color coded in (g) and (h).

Running Time Analysis We implemented our algorithms using C++ on Windows platform, with an Open source linear system solver UMFPACK [29]. All the experiments are conducted on a laptop computer of Intel Core2 T6500 2.10GHz with 4GB memory. The "Eight" model has about 1K vertices and the Amphora model has about 30K vertices. The registration pipeline took about 16 seconds.

Comparison to Holomorphic 1-Form based Method Prior to hyperbolic Ricci flow method, our prior work [49] proposed a holomorphic 1-form based method to compute the global conformal parameterization of general surfaces. Later, a holomorphic flow segmentation method was introduced in [143] to match general surfaces and this method was adopted in multivariate tensor-based morphometry research to study lateral ventricular morphometry [146]. Based on surface cohomology, the holomorphic flow segmentation method computes a set of holomorphic 1-form basis functions which induces global surface conformal parmeterizations on general surfaces. However, for high genus surfaces, i.e. genus number is great than one, the global conformal parameterization results will always have zero points, as shown in Fig. 25. The areas covered by the zero points are mapped to a single point and create big distortions around zero point areas. As a result, the surface matching results will always be inaccurate and create holes on the average surface shapes. Benefited by surface hyperbolic Ricci flow and hyperbolic harmonic map, the current method does not have any singularity point and one may achieve an exact diffeomrophic mapping between general surfaces.

4.5.2 Human Face Registration and Tracking

In this section we applied our algorithm to human face registration and tracking research. We ran our algorithm on a face sequence of 100 frames, with each face model has about $36k$ vertices. The Ricci Flow processing took 8 seconds for one frame averagely, the hyperbolic heat diffusion took about 10 seconds averagely. In the current setting, it took about 18 seconds to register each adjacent mesh frames.

We performed our algorithm on human face registration and tracking problem and evaluate our method by comparing with the Euclidean harmonic mapping with hard constraints[103, 1], as detailed in Sec. 4.4.4. To process the face model, we cut out the eye regions along the automatically identified eye contour curves [144]. We also cut the mouth open. After the topology optimization, each facial surface has four open boundaries and they are used as landmark constraints. The pants decomposition was shown in Fig 49 (a)-(d) shows the tracking result. We applied the hyperbolic harmonic mapping algorithm to each pair of adjacent meshes, with the mouth and eye boundaries as constraints, then put the same

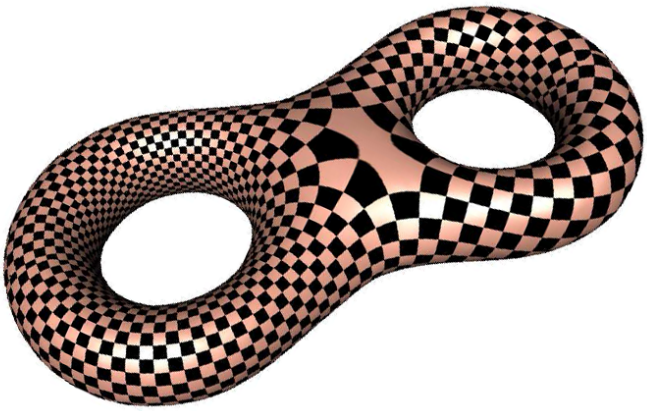

Figure 25: Zero point of Holomorphic 1-Form method on high genus surface.

registration mesh (as the green color) to each face to show the tracking result. The results demonstrated that our algorithm may well register surfaces with significant expression changes. Fig 49 (e)-(g) show the pants decomposition of the face model. The following sections detail the performance comparison results between our algorithm and the Euclidean harmonic mapping method.

Registration Flipping One of the most promising advantages of our registration algorithm is that it guarantees the mapping between two surfaces to be diffeomorphic. We randomly choose one face model as template and all others as source to do registration. For each registration, we compute the Jacobian determinant and measure the area of flipped regions. The ratio between flipped area to the total area is collected to form the histogram shown in Fig.29. The conventional method (blue bars) produces a big flipped area ratio, even as much as 9%. In contrast, the flipped area ratios for all registrations obtained by the current method are exactly 0's.

Curvature Distortion We first evaluated registration accuracy by comparing the alignment of curvature maps between the registered models [103]. In this work we calculated curvature maps using an approximation of mean curvature, which is the convexity measure. We quantified the effects of registration on curvature by computing the difference of curvature maps from the registered models. We assign each vertex the curvature difference between it's own curvature and the curvature of it's correspondent point on the target surface, then build a color map. Fig 49 (h)-(j) show that our method produced much less curvature distortion than the traditional harmonic method.

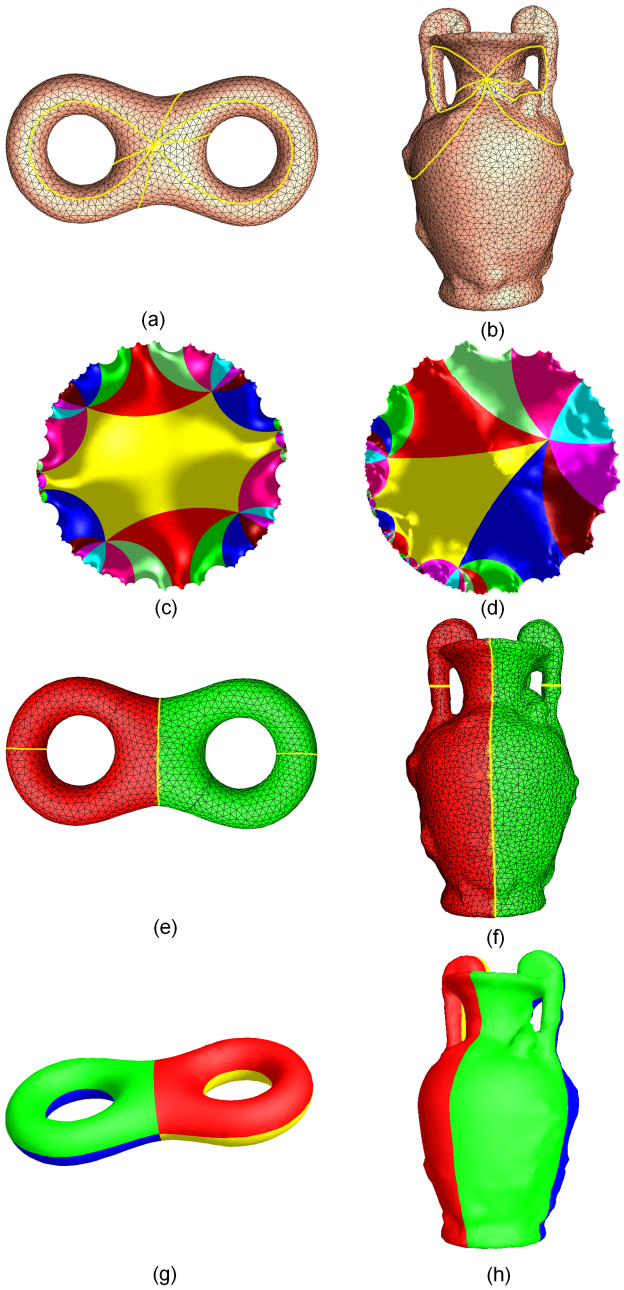

Figure 26: (a),(b) show the input Eight and Amphora model, as well as their geodesic homotopy basis. (c),(d) show their universal covering space on Poincaré's disk. (e),(f) show their pants decomposition, with each model been decomposed into 2 pants. (g),(h) show the each pant can be further decomposed into 2 hyperbolic hexagons.

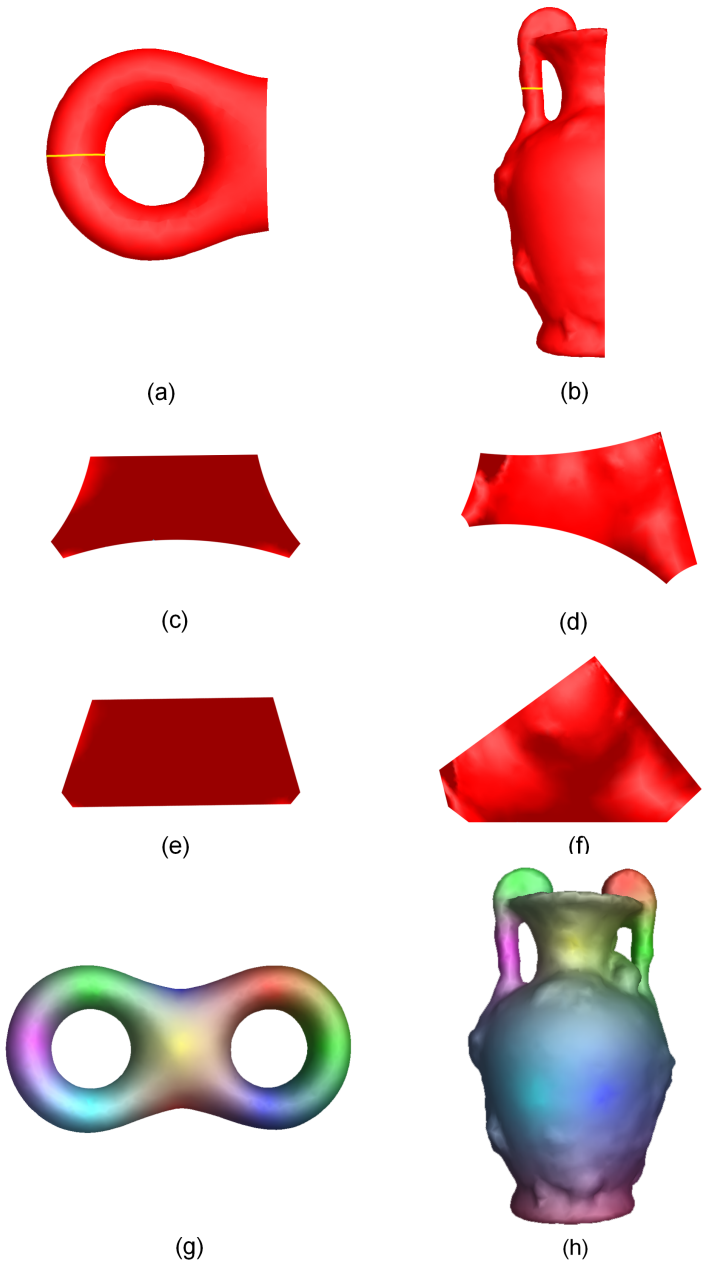

Figure 27: (a),(b) show one of the hyperbolic hexagons of Eight and Amphora model. (c),(d) show the image of (a),(b) on Poincaré's disk. (e),(f) show the image of (c),(d) after converted on Klein disk. (g),(h) show the final registration result by color mapping.

Area Distortion We also measured the local area distortion induced by the registration. For each point p on the template surface, we compute its Jacobian determinant $J(p)$, and

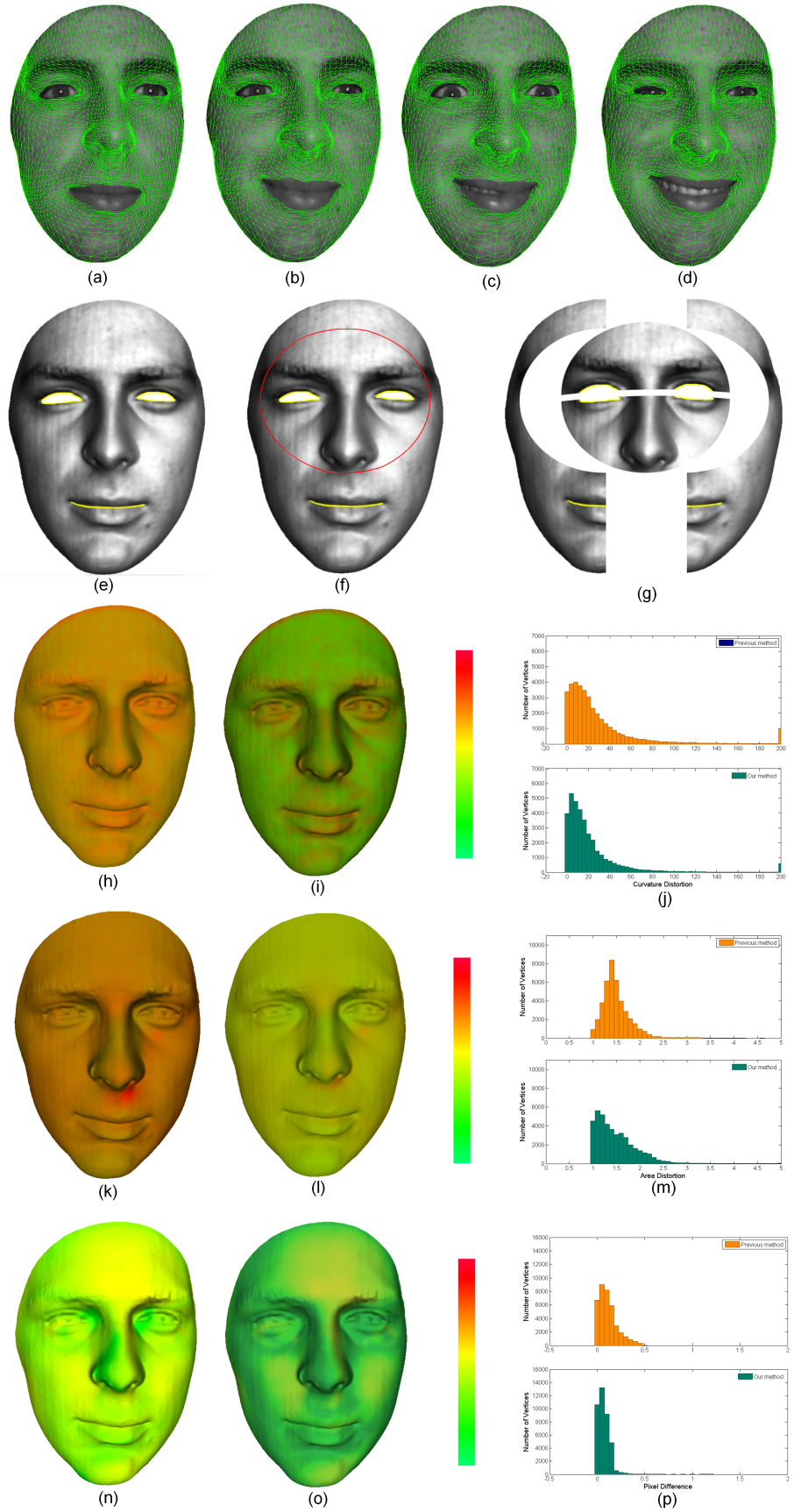

Figure 28: Experimental results for human face registration and tracking.

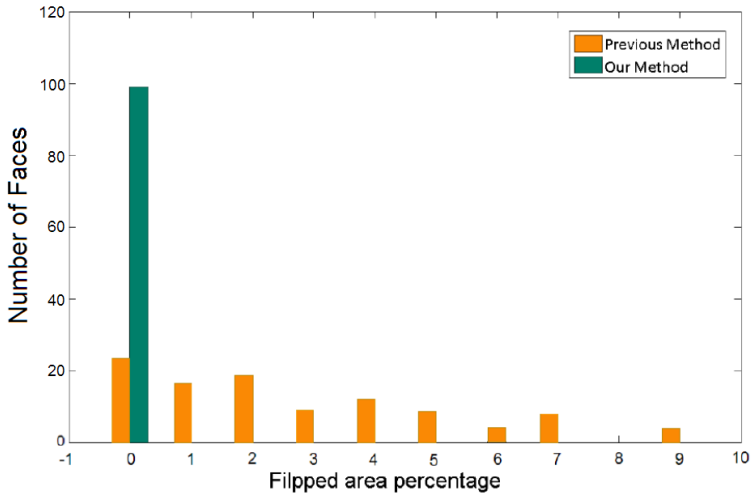

Figure 29: Flipped area percentage for human face registration.

represent the local area distortion function at p as $\max\{J(p), J^{-1}(p)\}$. J can be approximated by the ratio between the areas of a face and its image. Note that, if the registration is not diffeomorphic, the local area distortion may go to ∞. Therefore, we add a threshold to truncate large distortions. Fig 49 (k)-(m) show that our method produced much less area distortion than the traditional harmonic method.

Pixel Distortion Finally we evaluated the average registration accuracy using the pixel distortion: we calculate the pixel color difference between every source-image vertices of the face model, and compared to the traditional harmonic method. Fig Fig 49 (n)-(p) show that our method produced much less pixel error.

4.5.3 Cortical surface registration

In this section we apply our method to brain cortical surface registration problem. Morphometric and functional studies of human brain require that neuro-anatomical data from a population to be normalized to a standard template, so brain cortical surface registration is often needed. Due to the anatomical fact, the registration mapping is required to be smooth and bijective, namely, diffeomorphic. Since cytoarchitectural and functional parcellation of the cortex is intimately related the folding of the cortex, it is also important to ensure the alignment of the major anatomic features, such as sucal landmarks. We performed our algorithm on cortical surface registration problem and again compared with [103, 1]. We perform the experiments on 24 brain cortical surfaces reconstructed from MRI images. Each cortical surface has about $150k$ vertices, $300k$ faces and used in some prior

research [103]. On each cortical surfaces, a set of 26 landmark curves were manually drawn and validated by neuroanatomists. Fig. 30 show the landmark curves and their labels. In our current work, we selected 10 landmark curves, including Central Sulcus, Superior Frontal Sulcus, Inferior Frontal Sulcus, Horizontal Branch of Sylvian Fissure, Cingulate Sulcus, Supraorbital Sulcus, Sup. Temporal with Upper Branch, Inferior Temporal Sulcus, Lateral Occipital Sulcus and the boundary of Unlabeled Subcortcial Region. The hyperbolic Ricci flow takes about 120 seconds averagely, the hyperbolic heat diffusion takes about 100 seconds averagely. In the current setting, it takes about 90 seconds in average.

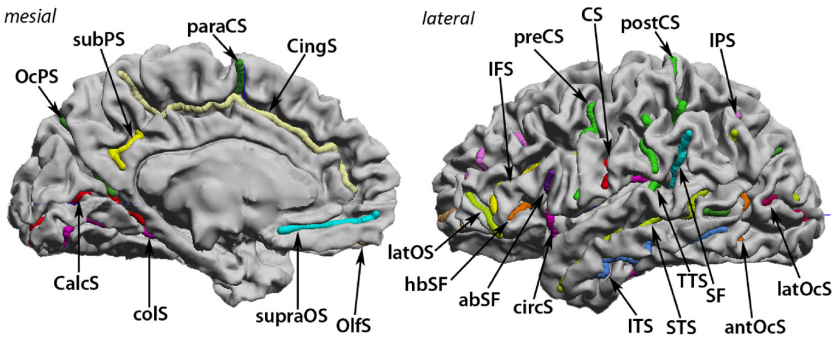

Figure 30: Landmark curves on human cortical surface [103].

Registration Visualization We show our visualized registration result of 2 brain models in Figure 37, with one as target and the other one registered to it. We can see our algorithm shows a reasonable good result.

Curvature Distortion We measure the curvature distortion according to the previous section. We use all 24 data sets for the experiment. First, one data set is randomly chosen as the template, then all others are registered to it. The average curvature difference map is color encoded on the template, as shown in Fig.32. The histogram of the average curvature difference map is also computed, as shown in Fig.33.

Area Distortion We measure the area distortion according to the previous section. We compute the average of all local area distortion functions induced by the 23 registrations

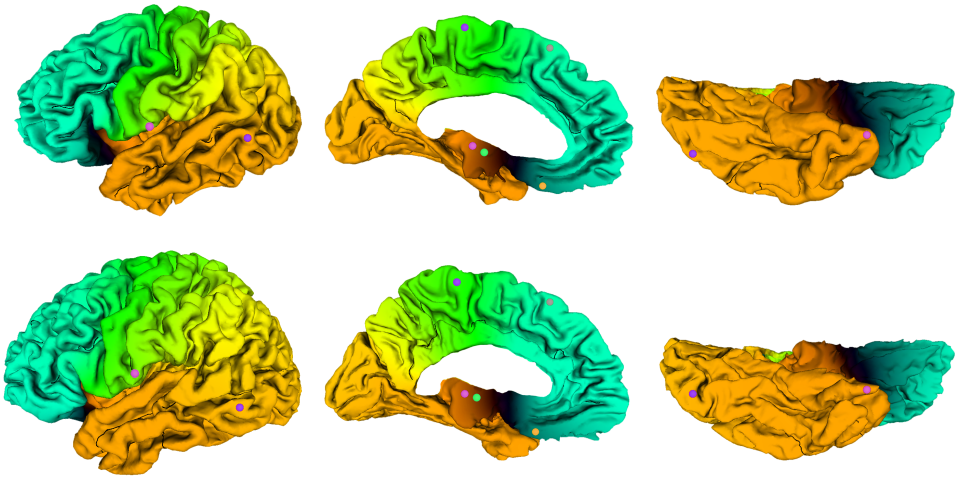

Figure 31: First row: source brain surface from front, back and bottom view. Second rows: target brain model. The color on the models shows the correspondence between source and target; the colored balls on the models show the detailed correspondence, as the balls with the same color are correspondent to each other.

on the template surface. The average local area distortion function on the template is color encoded as shown in Fig.34, the histogram is also computed in Fig.35.

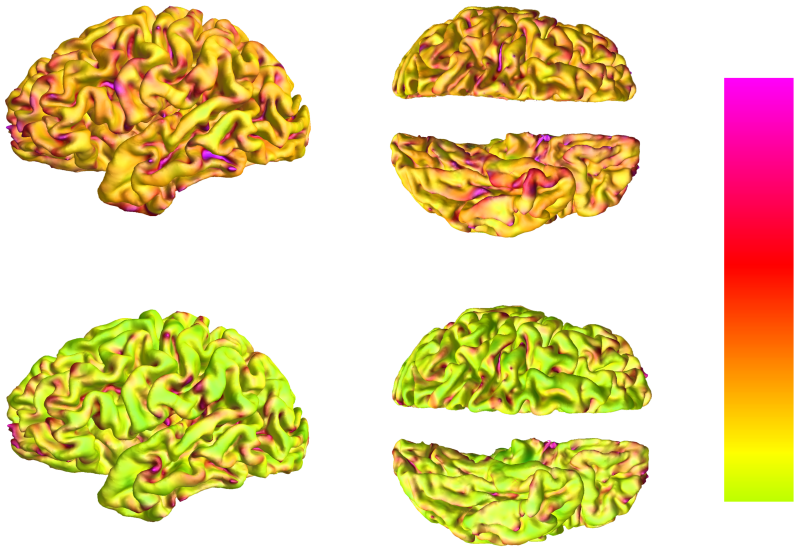

Figure 32: Curvature map difference of previous method (top row) and our method (bottom row). Color goes from green to red while the curvature difference increasing.

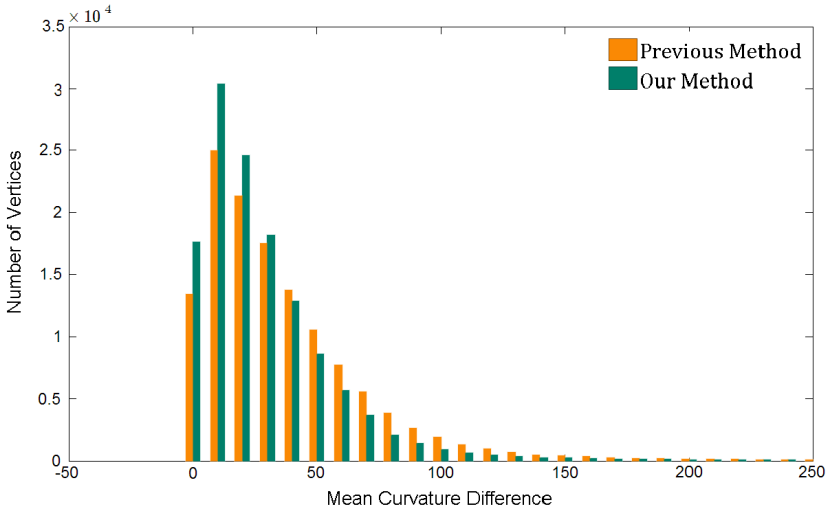

Figure 33: Average Curvature Map Difference.

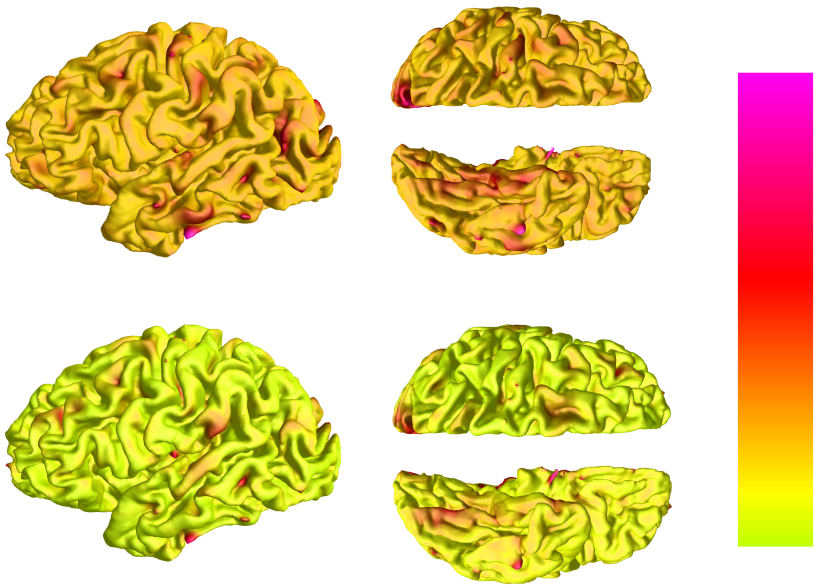

Figure 34: Average Area Distortion. Color goes from green to red while area distortion increasing.

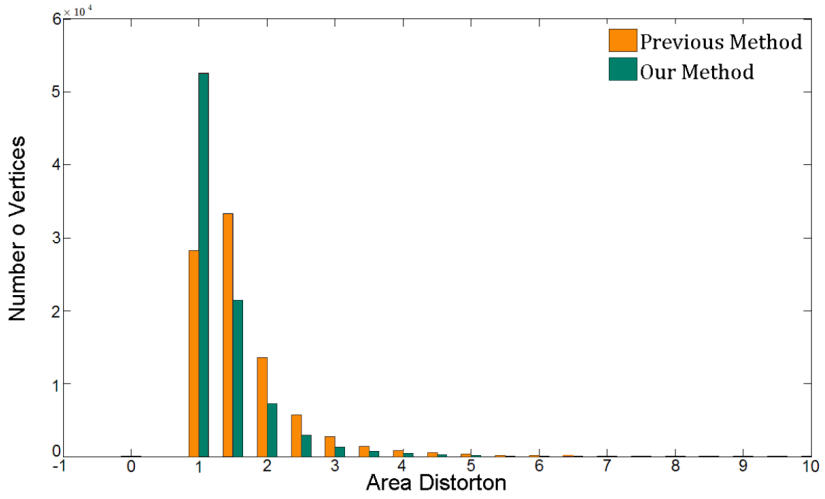

Figure 35: Average Area Distortion.

5 Traffic Analysis and Source Location Privacy under Random Walks

Random walk on a graph is a Markov chain and thus is 'memoryless' as the next node to visit depends only on the current node and not on the sequence of events that preceded it. With these properties, random walk and its many variations have been used in network routing to 'randomize' the traffic pattern and hide the location of the data sources. In this work we show a myth in common understanding of the memoryless property of a random walk applied for protecting source location privacy in a wireless sensor network. In particular, if one monitors only the network boundary and records the first boundary node hit by a random walk, this distribution can be related to the location of the source node. For the scenario of a single data source, a very simple algorithm which says the simple integration along the network boundary would reveal the location of the source. We also develop a generic algorithm to reconstruct the source locations for various sources that have simple descriptions (e.g., k source locations, sources on a line segment, sources in a disk). This represents a new type of traffic analysis attack for invading sensor data location privacy and essentially re-opens the problem for further examination.

5.1 Overview

Given a graph and a starting vertex, we choose a neighbor of the current node at random and move to this neighbor and continue in this fashion. This sequence of nodes is called a *random walk* on the graph. Random walk is a Markov chain such that the next node to visit only depends on the current node and is independent of the history. This is often termed as the "memoryless" property of a random walk, which makes it useful for many applications in computer networking. Of particular interest to this work is the application of random walk in wireless sensor network routing for preserving source location privacy.

Source Location Privacy: Wireless sensor networks find many useful civilian and military applications. In many settings one would like to protect the privacy of sensor data, defined in the general sense that sensor data and its contextual information are observable by only those who are supposed to observe it [72]. Providing privacy in wireless sensor network is challenging for a number of reasons. Besides that the sensor nodes are low cost devices with limited computation and storage capacities, the fact that the sensor nodes use wireless medium make it susceptible to attacks such as eavesdropping and traffic analysis. In the literature, privacy threats in sensor networks are classified as content-oriented privacy threats (i.e., the leaking of packet content to adversaries), that can be addressed by security and encryption mechanisms, and contextual privacy issues (i.e., the leaking of context information related to the measurement and transmission of the sensor data), of which location of the data source is a major piece of information to be protected. In particular, an adversary may be able to compromise private information of source locations without the

ability of decrypting the transmitted data – by simply monitoring and analyzing the traffic pattern in the air.

A classical model formed for protecting the source location privacy is the "Panda Hunter Game" [72]. In the game, a large number of panda detecting sensors are placed in a habitat to detect panda presence. Pandas here are analogs of generic assets to be monitored by a sensor network. When a panda is observed, the nearby sensor node will report such detection data periodically to the sink through multi-hop routing methods. The data package could be encrypted such that the adversary cannot decipher the content of the message and cannot derive the location of panda right away. However, an adversary, in this case, the hunter, can monitor the traffic in the network and by timing analysis trace back the routing path to the origin of the message, i.e., the location of the data source. Clearly, simple routing schemes such as shortest path routing cannot provide data source privacy against traffic analysis attacks.

Many schemes proposed in the literature for preserving source location privacy use a common idea of introducing randomness in packet routing. The objective is to make the traffic pattern look random and uncertain, and then counteract the adversarial traffic analysis attacks. Many of them use random walk or variations of random walks as a major component in the design. Phantom routing [72], for example, first uses random walk in the network until the node is reasonably far from the source node and then uses (probabilistic) flooding method to deliver it to the source. Although a short random walk may still have the current node correlated with the origin, a long random walk will stop at a location that is independent of the packet original. It is known that if the random walk is longer than the *mixing time*, the random walk converges to its limiting distribution called the stationary distribution [89]. This it is equivalent to selecting a node in the network randomly (from the stationary distribution) and thus packet analysis afterwards will only trace back to this random location, unrelated to the true data source.

Traffic Analysis on Random Walk: In this work we show that it is a myth in common understanding that random walk automatically brings with it source location privacy. In other words, we present a technique which allows certain traffic analysis to infer the source location even for random walks that are as long as they want. Therefore our message is that random walk should be used carefully in protecting source location privacy.

Network Model and Attack Model: We assume in this work a wireless sensor network deployed in a planar domain R of interest for monitoring interesting events. The event locations are of great importance for both the network owners and the adversary. When an event is detected, the nearby sensor node becomes the data source and sends the report periodically to a data sink (e.g., a base station or a mobile sink) in the network. We assume that the message is delivered by using random walk, in which the next node to visit is uniformly chosen from all neighbors of the current node. The random walk is sufficiently long to ensure that the message will be delivered to the data sink with high probability. A data source will generate data packets periodically and the delivery of these packets is

completely independent of each other. That is, they follow different random walk paths. The specific capabilities of the adversary is summarized below.

- *Monitoring traffic on network boundary.* We assume that the adversary can only monitor network traffic along the network outer boundary. This is a reasonable assumption in many settings when the domain of interest has restricted access to anyone but the network owner. It is also a realistic model of many military applications. The adversary places monitoring stations to monitor network traffic along the network outer boundary. Each monitoring station listens to the traffic in the neighborhood of a sensor node and record the signals delivered to/from the sensor node. We assume that the positions of the monitoring stations, or equivalently the network boundary, are known. The monitoring stations are also assumed to be perfectly synchronized. The traffic data from the monitoring stations is collected and delivered to an offline base station for further analysis. We remark that the assumption puts more restriction to the adversary's power than the Panda Hunter model, in which the adversary can be anywhere inside the network and can move around as fast as possible.
- *Packets are encrypted.* We assume that the packets in the network are encrypted using symmetric encryption between the data source and the data sink and that the adversary does not have the key to decipher the content of the message. Similar to the Panda Hunter problem, the data source issues data packets periodically. We assume that the content of these data messages are different, i.e., with different time stamps. The monitoring stations can compare the messages received by different boundary nodes and conclude whether two messages received by two boundary nodes are the same or not. We assume that the chained encryption scheme used in onion routing is not feasible for sensor network, for two reasons. First the chained encryption requires that the source knows the entire path taken by the message, which is not the case for random walk. Second, chained encryption and decryption for each relay node is too heavy for resource constrained sensor nodes.
- *Non-malicious.* The adversary does not interfere with the normal functioning of the sensor networks. Otherwise it will be detected by intrusion detection schemes. The adversary does not compromise any node and does not generate or alter traffic in the network.
- *Informed.* We use the standard philosophy in security [134] that the adversary is aware of the routing methods used by the system, in our case, the random walk scheme.
- *Centralized and powerful.* The monitoring stations gather traffic received from the network boundary and then deliver all the data to an offline central station for processing. We assume the adversary has abundant computing resources and can perform complicated analysis.

Traffic Analysis of Random Walk: We first consider a special case when the network is in a domain of disk shape and sensors are uniformly distributed inside the disk. In this case the random walk can be considered as a discrete approximation of the continuous Brownian motion inside a disk. For each message issued by the data source, through comparing the messages gathered by the monitoring stations at the network boundary we can conclude the node on the boundary that received the message for the first time. Now, since the data source generates multiple data packets, we monitor the position of the first hit on the boundary by different data packets. This constitutes a 'first hit' distribution (also called the exit distribution) ω'_x on the boundary where x is the source location. If the data source is at the center o of the disk, by symmetry the distribution ω'_x is a uniform distribution. When the data source is not at the center of the disk, the distribution has a single peak at the boundary intersected by the ray ox, and the closer the source to the boundary, the higher the peak is. See Figure 36 for an example. Therefore by monitoring the traffic pattern on the network boundary only, we obtain an observation of the first hit distribution p_x, through examining which we can infer the source location.

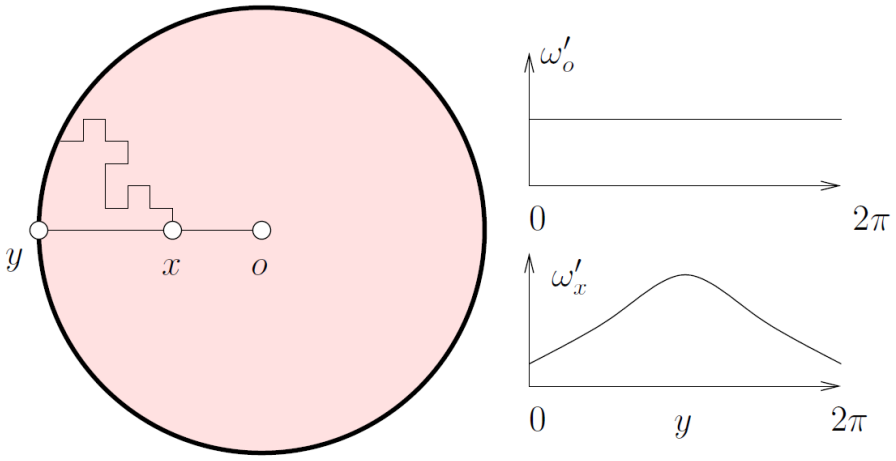

Figure 36: The first hit distribution ω'_x and ω'_o for random walk inside a unit disk starting at x and o respectively.

In general the network may not be of a disk shape thus the first hit distribution could have a complicated correlation with the source location. For a bounded domain R in the plane, the probability that a Brownian motion started inside a point $z \in R$ hits a portion of

the boundary is termed the *harmonic measure* [71] ω_z. The first hit distribution observed from the traffic pattern ω'_z is a Monte Carlo approximation of ω_z. On simply connected planar domains, there is a close connection between harmonic measure and the theory of conformal maps. A conformal map is a continuous one-to-one map that preserves angles. It is known that Brownian motions are conformally invariant [80]. What this means is that under a conformal map, $f : R \to R'$, the probability for a Brownian motion starting from $x \in R$ and exiting from an interval $I[a, b]$ on the boundary ∂R is the same as the probability of a Brownian motion starting from $f(x) \in R'$ and exiting from an interval $I[f(a), f(b)]$ on the boundary $\partial R'$. Now, since any simple planar domain can be mapped to a canonical shape of a unit disk by a conformal mapping, one can obtain the harmonic measure for any simply connected domain. In particular, take the example in Figure 36, we can apply a Mobius transformation f from a disk to a disk such that the point x is now mapped to the center of the disk. Therefore the distribution ω_x can be immediately computed through f.

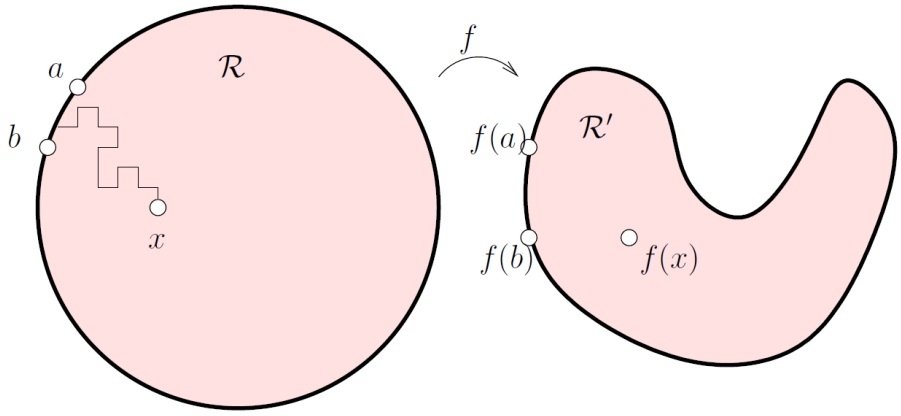

Figure 37: The probability for a Brownian motion starting from $x \in R$ and exiting from an interval $I[a, b]$ on the boundary ∂R is the same as the probability of a Brownian motion starting from $f(x) \in R'$ and exiting from an interval $I[f(a), f(b)]$ on the boundary $\partial R'$.

The discussion above suggests that the exit distribution observed by the adversary along the sensor network boundary can be used to infer the source locations. In this work we present such traffic analysis algorithms. We present two algorithms specifically. The first one is for recovery of a single data source. It is very simple, by integrating the position and the harmonic measure along the domain boundary, i.e., $\int_{z \in \partial R} z d\omega_x(z)$. To understand this,

take a look at Figure 36. If the source is at o and we integrate the position by the harmonic measure ω_o (which is uniform) along the unit circle, by symmetry this integration gives us the center of the disk. If the source is at x, the integration of the position by ω_x must lie on the line segment oy – again by axial symmetry of ω_x with respect to oy. In fact, this integration would give precisely the position of x. And this is true not only for the case of a unit disk but for *any* planar domain. Since the first hit distribution observed from the traffic pattern, ω'_x, would be a good approximation to the harmonic measure ω_x. By using $\int_{z\in\partial R} z d\omega'_x(z)$ we will get a very close approximation to x, as long as we have enough samples to be statistically meaningful.

The second algorithm is a general method using maximum likelihood estimation and it can be used for a general case when the data sources can be represented using low complexity. A number of representative scenarios include multiple data sources, data sources uniformly distributed on a line segment, as in the case of target tracking applications, or data sources uniformly inside a small disk or square, as in the case when an event triggers multiple sensors to report to the sink. The results and the algorithms can be extended to a non-simple planar domain as well as a general non-planar terrain.

We presented an extensive list of simulations for different network shape and different data source models as mentioned above. In particular, we presented the tradeoff between the number of messages issued by the data source vs the accuracy of our prediction of the source location.

Last we want to remark that we do not mean to claim that previous source location privacy preserving schemes using random walks are inadequate, but rather raise an alarm that their effectiveness should be reconsidered carefully given the potential attack illustrated in this work. At the end of the work we discuss variations of basic random walks and suggest ideas to defeat this particular traffic analysis attack.

5.2 Related Work

Routing that preserves source anonymity has been a topic of study for a number of years. For routing on the Internet, one would like to hide the sender's identity, as phrased in anonymous routing. The most popular schemes are Chaum's mixes [22] and onion routing [126, 127]. In Chaum's scheme, the idea is to send the message in an encrypted manner to a central server called the anonymizer, which removes the source identity and then sends the message to the receiver. Thus one cannot differentiate the sources of the messages delivered by anonymizer. Onion routing uses encryption on source routing, such that the source identifies the entire routing path to the destination and encrypt the messages in layers in the order of the nodes along the path. Each relay node descrypt the message using its own private key, which reveals the next hop and sends the message. In this way each node on the path is only aware of the immediate upstream and downstream node and is not aware of the entire path, in particular the source identity. Both schemes cannot be applied in sensor network setting since we cannot afford a central server, and public key encryption

is too heavy for sensor nodes. In addition, encryption based security schemes only protect the content of the messages but cannot deal with traffic analysis attacks.

Existing schemes for preserving source location privacy is summarized in a recent survey [83]. Among them, random walk is a commonly used component. Phantom routing [101, 72] first uses random walk to arrive at a node that is reasonably far away from the source and then use probabilistic flooding to deliver the message to the destination. Followup schemes such as in [147, 84, 92] use biased random walk in order to get farther away from the data source, or introduce fake data sources to further confuse the traffic pattern [72, 95]. In the next section we examine some of these variations and discuss the performance of the traffic analysis attack for these cases.

5.3 Theoretic Background

5.3.1 Conformal Maps

Let $\mathbb{C} = \{z : z = x + iy;\ x, y \in \mathbb{R}\}$ denote the complex plane. The following material can be found in [39, 2].

Definition 5.1. *A holomorphic function f on a domain $D \subset \mathbb{C}$ is a complex valued function defined on D such that the complex derivative of f exists everywhere inside D. This also implies that f is infinitely differentiable, equal to its own Taylor series and preserves angles at all points where the derivative of f is non-zero.*

A holomorphic function which has a non-zero derivative everywhere is also called conformal.

Definition 5.2. *A harmonic function f on a domain $D \subset \mathbb{R}^2$ is a twice continuously differentiable real valued function such that $\frac{\partial^2 f}{\partial x^2} + \frac{\partial^2 f}{\partial y^2} = 0$.*

Here are two useful properties:

- Let $f(z) = f_1(z) + if_2(z)$ be holomorphic. Then f_1 and f_2 are harmonic.
- *Mean Value Property* Let u be holomorphic/harmonic on the unit disk $\mathbb{D}$. Then, $u(0) = \int_{\partial\mathbb{D}} u(e^{i\theta})\frac{d\theta}{2\pi}$.

Mobius transforms and Riemann mapping:

Let $\mathbb{D}$ denote the unit disk centered at the origin in $\mathbb{C}$. The group of Möbius transformations is the set of all conformal maps from $\mathbb{D}$ to itself. It is well-known that any such map is of the form $f(z) = e^{i\theta}\frac{z - z_0}{1 - \bar{z}_0 z}$ for some $\theta \in (0, 2\pi)$ and some $z_0 \in \mathbb{D}$.

Let Ω be a simply connected domain (a topological disk) in the plane, such that the boundary $\partial\Omega$ is a smooth curve:

Theorem 5.3 (Riemann Mapping)**.** *Let Ω be as above. Then there exists a conformal map $f : \mathbb{D} \longrightarrow \Omega$. Further, f is unique upto composition by a Möbius transformation.*

5.3.2 Harmonic Measure

Definition 5.4 (Harmonic Measure)**.** *[13][41] For any subset X of the boundary ($X \subset \partial\Omega$), the harmonic measure of X with respect to z is defined as $\omega(X, \Omega, z) = \frac{1}{2\pi}|f^{-1}(X)|$.*

Here $|.|$ denotes the Euclidean length of an arc on the unit circle. Note that any two conformal maps sending O to z only differ by a rotation, so this definition does not depend on the f chosen. Using harmonic measure, one can extend the Mean-value property to arbitrary domains. If u is a harmonic function on an arbitrary simply connected domain Ω, $z_0 \in \Omega$ is a base point and f_{z_0} is a conformal map such that $f(0) = z_0$, then $u \circ f$ is harmonic on the disk, so that

$$u(z_0) = (u \circ f)(0) = \int_{S^1} u(f(e^{i\theta}))\frac{d\theta}{2\pi} = \int_{\partial\Omega} u(z)d\omega_{z_0} \tag{5.1}$$

where $d\omega_{z_0}$ is the harmonic measure with respect to z_0.

The harmonic measure $\omega(X, \Omega, z)$ is related to a Brownian Motion started in the domain Ω frm the point z. We define Brownian Motion next.

5.3.3 Brownian Motion

Definition 5.5. *A one-dimensional Brownian Motion [81] W_t intuitively is a scaling limit of the random walk. In other words, it is a stochastic process indexed by time $t > 0$, which has the following properties :*

1. *$W_0 = x$; here $x \in \mathbb{R}$ is the starting point.*
2. *The process has independent increments, i.e. for any two disjoint intervals $[s_1, t_1]$ and $[s_2, t_2]$, where $s_i, t_i > 0$, the increment in one interval $W_{t_1} - W_{s_1}$ is independent of the increment in the other $W_{t_2} - W_{s_2}$.*
3. *$W_{t+h} - W_t$ is Normally distributed with mean 0 and variance h.*
4. *Almost surely, the function $t \longrightarrow W_t$ is continuous.*

The case $W_0 = 0$ is called Standard Brownian Motion. A two-dimensional Brownian motion is a pair $B_t = (W_t^1, W_t^2)$ of two independent one-dimensional Brownian Motions.

5.3.4 Harmonic Measure, Brownian Motion and Conformal Invariance

An important property of the Brownian motion is that it is invariant under conformal changes, i.e. the image of a Brownian motion under a conformal map is again a Brownian motion in the image of the domain [81]. The Brownian Motion can be viewed as the limit, as $t \longrightarrow 0$, of a walk which starts at 0, chooses a direction randomly, goes a distance t in that direction, and continues this way at every point. The angle changes are preserved

under conformal maps, therefore one should expect that the law of the trajectory should be invariant.

Clearly, the same is true for harmonic measure. In other words, $\omega(X, \Omega, z) = \omega(f(X), f(\Omega), f(z))$ for any $X \subset \partial\Omega$ and f conformal.

5.3.5 Discrete Theory

In this section, we summarize the related theories of random walks on graphs.

Suppose G is a planar graph, embedded on the plane. Let $V = \{v_1, v_2, \cdots, v_n\}$ be the vertex set, (x_k, y_k) be the 2D position of vertex v_k, $E = \{e_1, e_2, \cdots, e_m\}$ be the edge set. For simplicity, we assume each face of G is a triangle.

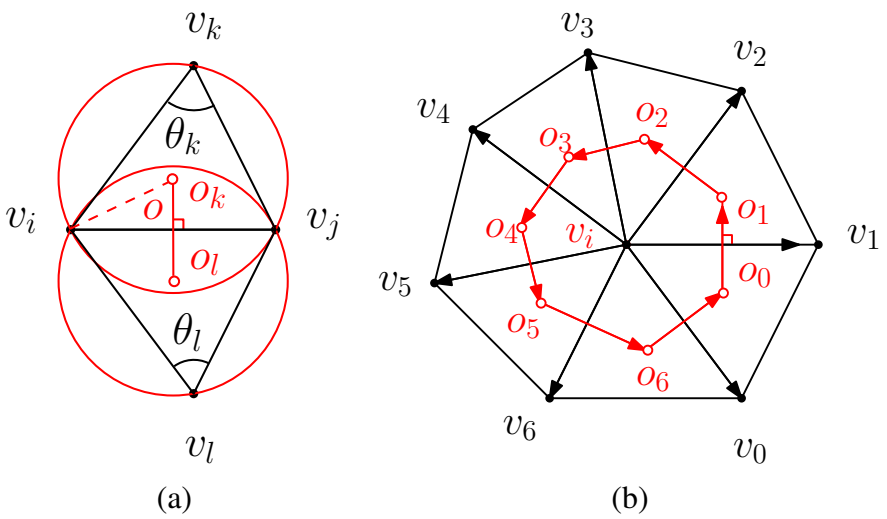

Figure 38: (a) shows the edge weight. (b) shows that the vertex position function is harmonic.

The following edge weight definition is motivated by the relationship of random walk and resistance of the triangulation as in an electrical network [15][35].

Definition 5.6 (Cotangent Edge Weight)**.** *[35, 15] Suppose edge $[v_i, v_j]$ is adjacent to two faces $[v_i, v_j, v_k]$ and $[v_j, v_i, v_l]$, then the weight on edge is given by $w_{ij} = \frac{1}{2}(\cot\theta_k + \cot\theta_l)$.*

The edge weight determines the transition probability for a random walk on graph.

Definition 5.7 (Random Walk on Graph)**.** *Suppose $X(t)$ is a random walk on the graph G defined as follows: if at time t the walk is at vertex v_i, then the probability of v_j being the next vertex is given by: $Prob\{X(t+1) = v_j | X(t) = v_i\} = \frac{w_{ij}}{\sum_k w_{ik}}$.*

When we choose a uniform sampling and all the triangles are equilateral triangles, all the edge weights are close to 1. In this case the above definition becomes the same as the random walk with uniform distribution on all neighbors. In our simulations we choose G to be a Delaunay triangulation on a nice set of samples inside R.

Definition 5.8 (Discrete Harmonic Measure)**.** *Suppose G is a planar graph with triangular faces. If the random walk $X(t)$ starts from a vertex v_i and exits at $v_k \in \partial G$, then the discrete harmonic measure is defined as the probability $\omega_k(v_i) := Prob\{X \sim v_k | X(0) = v_i\}$.*

Here $X \sim p$ means that the random walk X exits the boundary ∂G via the point p.

Definition 5.9 (Discrete Laplace Operator)**.** *Let $f : V \to \mathbb{R}$ be a function defined on the vertices of the graph G. The discrete Laplace operator is defined as $\Delta f(v_i) = \sum_j w_{ij}(f(v_j) - f(v_i))$.*

Definition 5.10 (Discrete Harmonic Function)**.** *Let $f : V \to \mathbb{R}$ be a function and Δ be the discrete Laplace operator. If Δf equals to zero for all vertices, then f is called a discrete harmonic function.*

From definition, it is easy to show that discrete harmonic measures $\omega_j : V \to \mathbb{R}$, $\forall v_j \in \partial G$ are harmonic functions. By definition, expected position function is harmonic. Figure 38 shows the vertex position function is also harmonic. Like smooth case, discrete harmonic functions have mean-value property, which states the value at each vertex is the average of the values in the neighborhood. Mean-value property implies maximal value principle, which says the max and min value of a harmonic function must be on the boundary of the graph.

Definition 5.11 (Discrete Dirichlet Problem)**.** *Suppose $f : V \to \mathbb{R}$ is a function defined on the graph, f is harmonic, and with boundary condition $f|_{\partial G} = g$,*

$$\begin{cases} \Delta f(v_i) &= 0 & \forall v_i \notin \partial G \\ f(v_j) &= g(v_j) & \forall v_j \in \partial G. \end{cases} \tag{5.2}$$

Then from the maximum modulus principle, we can get the uniqueness of the solution to the discrete Dirichlet problem. The solution to the Dirichlet problem can be explicitly given using harmonic measure.

Theorem 5.12 (Harmonic Measure Boundary Integration)**.** *Suppose $f : V \to \mathbb{R}$ is the solution to the Dirichlet problem (Eqn.(5.2)). Then $f(v_i) = \sum_{v_j \in \partial G} g(v_j)\omega_j(v_i)$.*

Suppose a vertex v_0 at (x_0, y_0) sends messages routed by random walks. Figure 38 (b) shows the position function is harmonic. According to theorem 5.12, $(x_0, y_0) = \sum_{v_k \in \partial G}(x_k, y_k)\omega_k(v_0)$.. This is a linear running time algorithm, given the harmonic measure $\omega_k(v_0)$ =Prob$\{X \sim v_k | X(0) = v_0\}$. In our applications, we estimate the harmonic measure simply by the ratio between the number of messages received at v_k and the total number of messages.

The above definitions and theorems do not require the graph to be planar. In fact, these concepts can be defined on triangular meshes in $\mathbb{R}^3$. But the 3D vertex position is not harmonic. Similar to smooth case, one can apply conformal mapping [113][47] to flatten the 3D triangulation and use the same method to estimate the source position on the 2D image. Because the Laplace matrix is solely determined by the connectivity of the graph and the corner angles, roughly speaking, discrete conformal mapping preserve angles, therefore conformal mapping preserves harmonic measures. Therefore, the harmonic measure can be estimated using the random walks on the 3D mesh, and applied for boundary integration to estimate the source location on the 2D image plane.

5.4 Algorithm: Traffic Analysis on Random Walks

5.4.1 Settings

We assume that a sensor network W is deployed densely in a geometric domain R. Packet routing in the sensor network is done by random walk on the network. Suppose that a data source at x generated N data messages, we record for each message the boundary node that receives this message for the first time. This frequency count can be normalized as a distribution ω'_x on the sensor network boundary. The input to the traffic analysis algorithm for the adversary is the exit distribution ω'_x, together with the geometry of the sensor network boundary R. The adversary has no knowledge of the sensor network in the interior of R and would like to reconstruct the position x.

To reconstruct the source location, we assume that the sensor network is dense and thus the random walk is a good approximation of Brownian motion in the continuous domain R. Therefore, for each point $x \in R$, define by ω_x the exit distribution of Brownian motion starting from x. We will compare ω'_x to ω_x to reconstruct the position of the source. Notice that in this setting there are two relaxations: 1) the distribution ω'_x is obtained through random walk on the (unknown) graph W; 2) the distribution ω'_x is obtained through a Monte Carlo method, i.e., based on the frequency count of N random walk samples. Thus our prediction of the source location could be a bit off from the true source location. But if random walks on the real sensor network are good approximations of the Brownian motion in R, and that the number of samples, N, is not too small, the error in the prediction is expected to be small. This is indeed confirmed by simulations in the next section.

We will present two algorithms. The first algorithm provided a closed-form solution by simply integrating along the domain boundary R. It works for a single source on a topological disk domain or topological disk with multiple holes. The second algorithm is based

on maximum likelihood method. Basically by comparing ω' and ω (the exit distribution of brownian motion), we find the source location y such that ω'_x and ω_y are the most similar. This is a generic framework for finding the locations of multiple data sources or any sources that can be represented in a compact way.

5.4.2 ALG1: Integration Along Domain Boundary

Recall that if u is a harmonic function on the domain Ω, then its value at any point in the interior can be recovered by its values on the boundary, as long as one knows the harmonic measure of the boundary, i.e. $u(z_0) = \int_{\partial\Omega} u(z) d\omega_{z_0}$ where $d\omega_{z_0}$ is the harmonic measure with respect to z_0. Clearly, the identity function $u(z) = z$ is holomorphic (i.e., is differentiable in z), the real part and imaginary part are both harmonic. Hence we get $z_0 = \int_{\partial\Omega} z d\omega_{z_0}$.

For the case of a single source at position z, our construction algorithm is to simply multiply the coordinates of the location of a point $p \in \partial R$ with its harmonic measure and add the resultants over the entire boundary. This algorithm is a linear running time algorithm with complexity dependent only on the *length* of the boundary ∂R. The algorithm applies for all planar domains, including multiply connected ones.

Calculating harmonic measure Now we show how to efficiently compute $\omega(X, R, z)$,i.e. for any point z and any subset X of the boundary of R, the probability that a random walk started from z will first exit the boundary from X. We first handle the (highly symmetric) case where the domain is the disk $\mathbb{D}$; X then is a subset of the unit circle and the starting point is the origin.

$\omega(X, \mathbb{D}, 0)$: This is the probability that a random walk started from the origin in the disk exits the disk from the set X on the boundary. Clearly, this is uniform (by symmetry), and hence $\omega(X, \mathbb{D}, 0) = \frac{|X|}{2\omega}$. In other words this probability is just the normalized Euclidean arclength of X.

$\omega(X, \mathbb{D}, z_0)$: To compute the harmonic measure for an arbitrary point $z_0 \in \mathbb{D}$, recall from 5.3.1 that the (conformal) Möbius transformation $g(z) = \frac{z - z_0}{1 - \bar{z_0} z}$ maps the unit disk to itself and sends the point z_0 to the origin. Now, we use the property that the harmonic measure is preserved under conformal maps to obtain

$$\omega(X, \mathbb{D}, z_0) = \omega(g(X), \mathbb{D}, g(z_0)) = \omega(g(X), \mathbb{D}, 0) = \frac{|g(X)|}{2\omega}$$

$\omega(X, R, z_0)$ **for arbitrary** R Here we will describe how to find the harmonic measure for an arbitrary planar domain R. The first method only works for simply connected domains (domains with no holes) while the second works for both simply and multiply connected domains.

Method 1: Using Riemann Mapping This method uses the conformal invariance we described in Section 5.3.4. As above, let R be a simply connected domain, with boundary Γ a Jordan curve. In almost all practical applications, one approximates R by a polygon, and

Γ by a polygonal chain. The first step is to compute the Riemann mapping from D to R. For accomplishing this task, various methods have been proposed [113][47].

So let us assume we have computed the Riemann mapping $f : \mathbb{D} \longrightarrow R$. Notice that $f^{-1} : R \longrightarrow \mathbb{D}$ is also conformal and once again, conformal invariance implies that $\omega(X, R, z_0) = \omega(f^{-1}(X), \mathbb{D}, f^{-1}(z_0))$ and we have shown how to compute $\omega(X, \mathbb{D}, z)$ for arbitrary $X \subset \partial\mathbb{D}$ and $z \in \mathbb{D}$ previously.

Method 2: Symm's Method This method does not require one to explicitly compute the Riemann Mapping from $\mathbb{D}$ to R, and holds for multi-holed domain. We refer the reader to [13] for a short summary of this method.

Recall from 5.1 that for any holomorphic function u on R, we have the property $u(z_0) = \int_{\partial R} u(z) d\omega_{z_0}$. We can discretize the boundary of R into n intervals $\{P_j\}_{j=1}^n$, assume that the harmonic measure is constant in each interval and look at the discrete counterpart to the above equation:

$$u(z_0) = \sum_j \int_{P_j} u(z) d\omega_{z_0} = \sum_j \frac{\omega_{z_0}(P_j)}{|P_j|} \int_{P_j} u(z) dz$$

Now if we choose n independent harmonic functions $\{u_i\}_{i=1}^n$, we get a system of n equations in n unknowns and we can solve to find $\omega_{z_0}(P_j)$.

5.4.3 ALG2: Maximum Likelihood Method

To apply a maximum likelihood approach (MLE), we first need the exit distribution/harmonic measure of a Brownian motion starting at a point $z \in R$, which can be computed using methods in the section above. We then explain the application of MLE for different settings.

Let $f(.|\theta)$ denote a family of distributions parameterized by θ. If one observes an i.i.d. sample $x_1, x_2, ...x_n$ from one of the distributions in this family, the Maximum Likelihood Method is a way to estimate the true parameter θ_0 such that this sample is most likely to come from $f(.|\theta_0)$.

Since the observations are assumed to be identically and independently distributed, the joint density function is

$$f(x_1, x_2, ...x_n|\theta) = f(x_1|\theta) f(x_2|\theta) ... f(x_n|\theta)$$

One then forms the *Likelihood Function*

$$\ell(\theta|x_1, x_2, ...x_n) = \Pi_{i=1}^n f(x_i|\theta)$$

The maximum likelihood estimate (MLE) $\hat{\theta}$ is defined to be the value of θ which maximizes the likelihood function, given the observed values x_i, i.e.

$$\hat{\theta} = \underset{\theta}{\operatorname{argmax}}\, \ell(\theta|x_1, x_2, ...x_n)$$

For simplicity, the log-likelihood function $\hat{\ell} = \log \ell$ is also used, since $\log$ is a monotonic transformation.

From now on, $f_z := f(x|z)$ will denote the density function for the harmonic measure. Denote by X_z the exit position (the first hit position) of a random walk starting at z. It is a random variable distributed with density f_z; $\mathbb{P}(X_z \in A) = \int_A f_z(x)dx$ for all $A \subset \partial\Omega$.

- **Single source.** Suppose that $x_1x_2, ...x_N$ are the first hit positions on the boundary for the N messages sent by an unknown source $z_0 \in R$ respectively. We know $f(x|z)$ from the previous section, form the likelihood function and maximize.
- k **sources,** k **is known.** This boils down to the single source problem for each of the sources. Now let's assume that the adversary cannot distinguish the data packets from different sources. Let the unknown source locations be $z_1, ...z_k$. Then what we observe is the random variable

  $$Y = X_{z_1} + X_{z_2} + ...X_{z_k}$$

  Given the z_i, the density of Y can be computed. Again one can form the likelihood function and maximize, now with respect to the vector of z_i. We also allow short-lived fake message which is sent to a randomly selected neighbor by the relay node after a real message is relayed. Our traffic analysis is not affected if the fake messages are discarded and not relayed any further.
- **Source moving on a line.** Assuming that we have a mobile data source moving on a line. The source sends packets periodically after distance ϵ. We are interested in estimating the initial position z_0 and the direction θ in which the source is travelling. Let $z_i = z_0 + i\epsilon e^{i\theta}$. Notice here we just need to estimate 3 real parameters, thus we could expect to get good estimates with just a lot fewer data packets per source z_i.

5.5 Experimental Results

We conducted extensive simulation tests to examine the performance of our algorithm to find the source location, as well as how recovery accuracy is affected by different parameters.

The simulations were done under different settings, namely a unit disk, a planar non-disk domain, a planar domain with holes and a non-planar domain. Also for each type of domain, we conducted simulations using both a triangle mesh (TM) and a unit disk graph (UDG). In TM model, we calculated the transition probability for each node d by it's neighbors in the triangulations; for UDG model, we calculated the transition probability for d by it's neighbors in the unit disk graph. We scaled all planar domains inside a 2×2 bounding box, and scaled non planar domains inside a $2 \times 2 \times 2$ bounding box. We use the term $Error$ to measure the distance between the true source location and the location predicted by our algorithm. The $Error_{ave}$ and $Error_{max}$ bellow, which represent the average and

max value of $Error$, are respect to the bounding box unit above. In the following, N_{domain} represents the number of nodes inside domain R, N_{msg} represents the number of messages issued at each source node.

Unit Disk Domain Figure 39 right and figure 40 right show the relationship between N_{msg} with $Error_{ave}$ and $Error_{max}$ under TM disk model and UDG disk model respectively. This is obtained by fix N_{domain}=1K, then randomly chose n=100 sources inside the R and issued N_{msg} numbers of random walks started from each of these chosen sources, then calculated the $Error_{ave}$ and $Error_{max}$ respectively. Beside this, we also examined how the location of source (the distance r from disk center) affects $Error_{ave}$. We uniformly sampled $0 < r < 1$ to get $\{r_1, r_2, ...r_m\}$, for each r_i we randomly chose n_i=100 points whose distance to center r_{n_i} satisfies $r_i - \varepsilon < r_{n_i} < r_i - \varepsilon$ (here we used ε=0.05) as the source to issue random walk for N_{msg}=1000 times. Then we use our method to predict the source location according to the boundary message distribution. Based on the real source location and the one calculated by our method, we computed $Error_{ave}$ for each r_i. Figure 39 left and figure 40 left show the relationship between r_i and $Error_{ave}$ under TM model and UDG model respectively. We can see that $Error_{ave}$ decreased while the real source leaving the disk center.

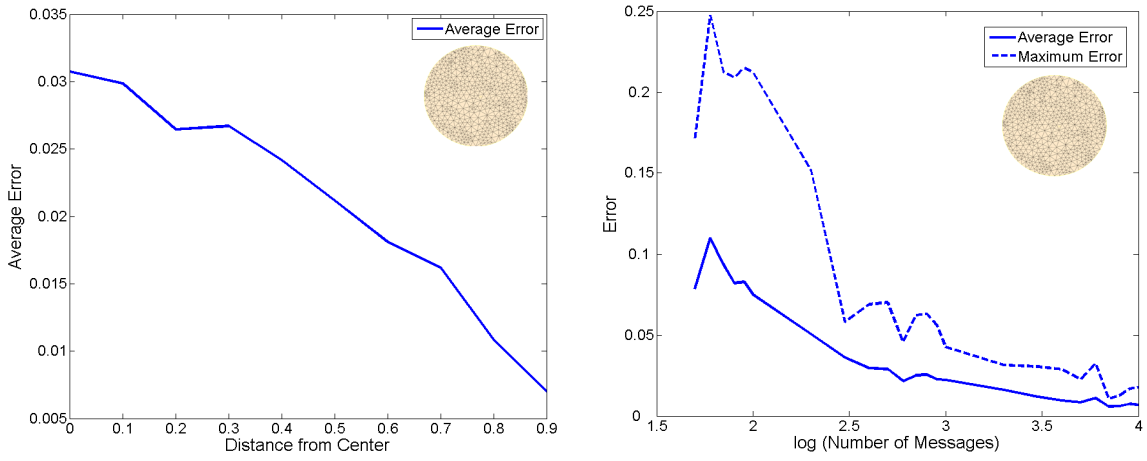

Figure 39: Left: Distance from Center VS. $Error_{ave}$ under TM Model. Right: N_{msg} VS. $Error_{ave}$/$Error_{max}$ under TM Model.

Planar non-disk Domains We did the same kind of simulation on an irregular domain. We

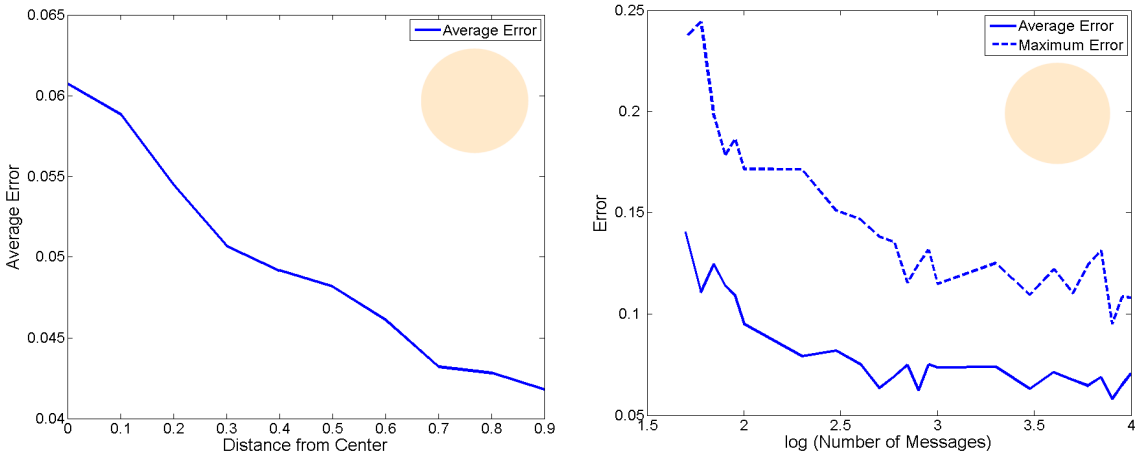

Figure 40: Distance from Center VS. $Error_{ave}$ under UDG Model. Right: N_{msg} VS. $Error_{ave}$/$Error_{max}$ under UDG Model.

evaluated how N_{msg} affects $Error_{ave}$ and $Error_{max}$ by fix N_{domain}=1K. The results are shown in figure 41. We can see that $Error_{ave}$ and $Error_{max}$ decreased while we increased N_{msg}. We obtained $Error_{ave}$ around 0.04 and 0.08 under TM model and UDG model by 100 messages.

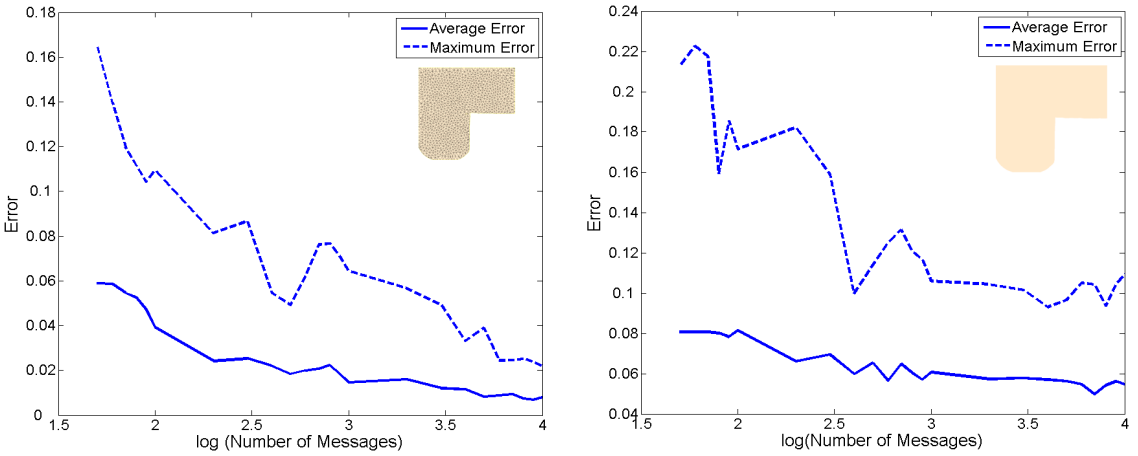

Figure 41: Left: N_{msg} VS. $Error_{ave}$/$Error_{max}$ under TM Model. Right: N_{msg} VS. $Error_{ave}$/$Error_{max}$ under UDG Model.

Planar Domain with Holes The same as above, we evaluated how N_{msg} affects $Error_{ave}$ and $Error_{max}$ for a planar domain with holes. For a planar domain with holes, as long as we can monitor the inside hole boundaries as well, we can just treat them as the same as outer boundary in the calculation. The results are shown in figure 42. We obtained $Error_{ave}$ around 0.04 and 0.07 under TM model and UDG model by 100 messages.

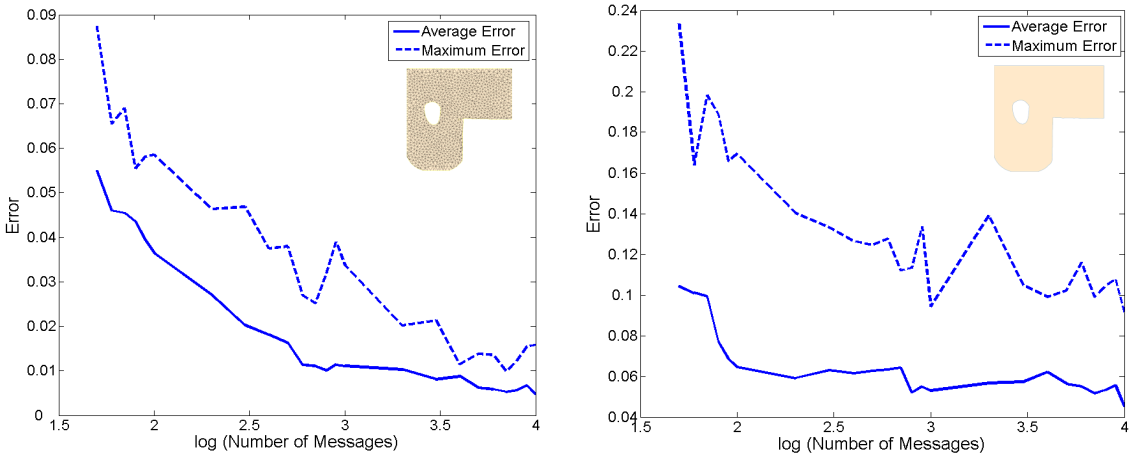

Figure 42: Left: N_{msg} VS. $Error_{ave}$/$Error_{max}$ under TM Model. Right: under UDG Model.

Non-planar Domain For a general non-planar domain, we first mapped it to the unit disk using conformal mapping method in[47]. Since Brownian motion is invariant under conformal mapping, we used the same method to calculate source location in the parameter domain, then mapped it back to the original surface. The simulation results are in figure 43. We obtained $Error_{ave}$ around 0.08 and 0.09 under TM model and UDG model by 100 messages.

Visualization of Exit Distribution Following we show the exit distribution along the domain boundary. We took the non-uniform planar domain, set an arbitrary source and visualizes the exit distribution (figure 44 left) using small disks along the boundary with area proportional to $NO.\ of\ first\ hit$. We also show the distribution on the parameter domain, which is obtained by conformally mapping the non-uniform domain to a unit disk (figure 44 right). The distribution on the parameter domain gives strong evidence that conformal mapping preserves Brownian motion. Namely the Brownian motion starting from source

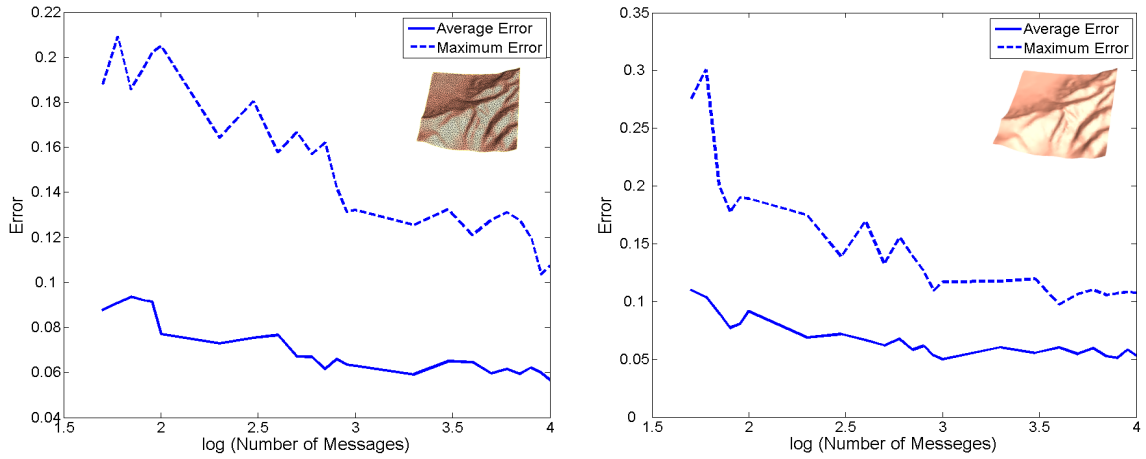

Figure 43: Left: N_{msg} VS. $Error_{ave}$/$Error_{max}$ under TM Model. Right: under UDG Model.

s on surface M is equivalent to the Brownian motion start from $\phi(s)$ on surface $\bar{M}$, if $\phi : M \to \bar{M}$ is a conformal mapping from M to $\bar{M}$.

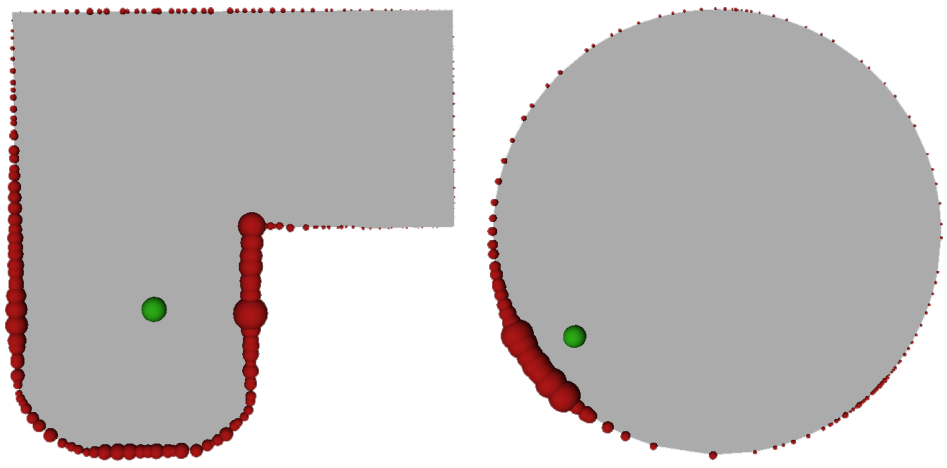

Figure 44: Left: First Hit Distribution. Right: First Hit Distribution on parameter domain.

Network Density Versus Average Error To examine how much the network density N_{domain} affects the average distance error $Error_{ave}$ by fix N_{msg}, then varying N_{domain} and observe $Error_{ave}$. The results are shown in Figure 45.

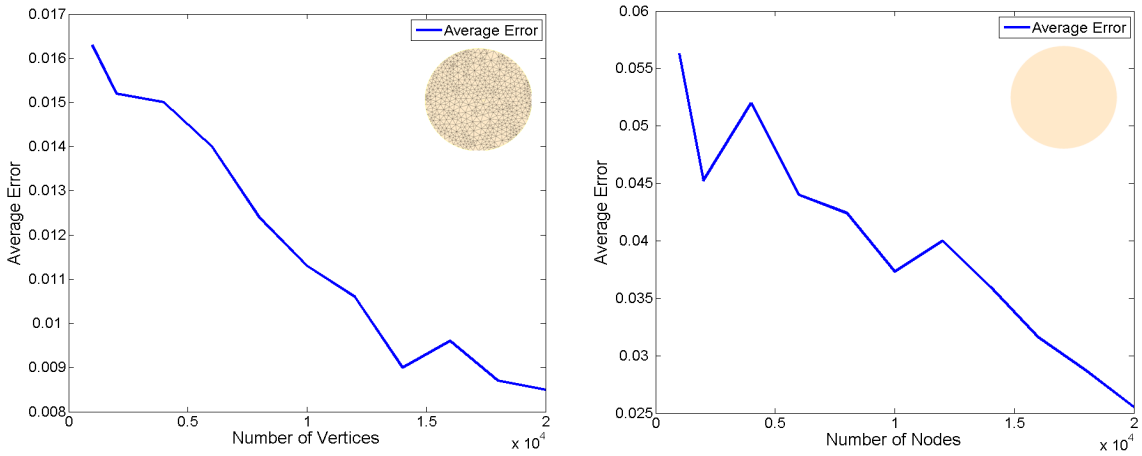

Figure 45: Left: N_{domain} VS. $Error_{ave}$ under TM. Right: N_{domain} VS. $Error_{ave}$ under UDG.

Multiple Sources We uniformly discretized the unit square domain into $N \times N$ grids(N=20 in our experiment), and assumed the possible location of a source is on the center of a grid. For 2 sources case, there are $N^4/2$ numbers of possible source location combinations. For each possible pair $(s_i,\ s_j)$, we issued $N_{msg} = 2000$ numbers of random walks from s_1 and s_1 , then stored a set of first hit distributions $\{\Phi_{ij}, 0 < i, j < N\}$. Then we randomly picked sources pair $(s_1,\ s_2)$ to issue $\bar{N}_{msg}$ random walks and obtained a first hit distribution Φ_{test}. By comparing Φ_{test} with Φ_{ij} we got a p-value which stands for the probability that Φ_{test} and Φ_{ij} are the same distribution. The i, j which gave the maximum p-value directly points out the location of s_i and s_j. In this experiment, we varied $\bar{N}_{msg}$ and obtained a set of $Error_{ave}$, like in figure 46. We can see that $Error_{ave}$ decreased as we increased $\bar{N}_{msg}$.

5.6 Discussions

Length of Random walks Our traffic analysis scheme uses the exit distribution of random walks on the network boundary. This means that the random walks should be long enough

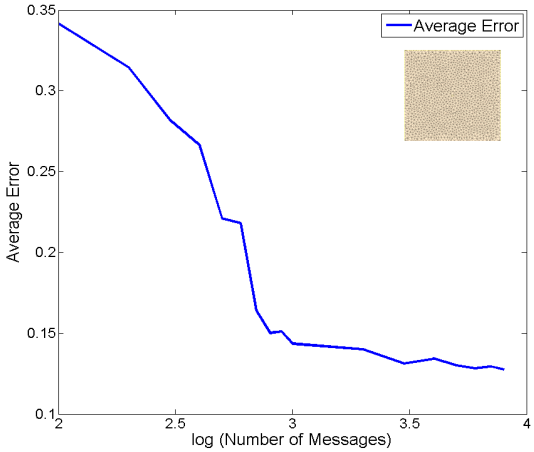

Figure 46: N_{msg} VS. $Error_{ave}$ for two sources.

so that they hit the network boundary with good probability before they stop. We argue that this is true as the random walks should be long enough to deliver the message to the data sink. If the data sink is at an unknown location in the network, the random walk should be long enough so that it visits every node in the network. This is termed as the *cover time*, defined as the expected number of steps for a random walk to cover all the nodes in the network [89]. For a 2D grid of n nodes the cover time is roughly in the order of $\Omega(n^2)$.

To estimate the probability that a random walk of length h hits the network boundary, we again consider a 2D grid of n nodes. Suppose X_i is the displacement vector of the i-th step of the random walk. X_i is uniformly chosen from $\{(1,0),(-1,0),(0,1),(0,-1)\}$. The position of random walk after i steps starting from the center of the grid is simply $P_i = X_1 + X_2 + \cdots + X_i$. By the central limit theorem, P_i is a Gaussian distribution with mean $(0,0)$ and variance $h/2\mathbb{I}$, where I is a 2×2 identity matrix. Thus the probability that P_i is outside a disk of radius r from the center is estimated as $e^{-r^2/h}$. Choose h to be $O(n^2)$ and r to be $\sqrt{n}$, the probability above is $1 - 1/n$. This means that the random walk of length $O(n^2)$ has a high probability to hit the network boundary at least once. This means that for a random walk to deliver the message to the sink, it must hit the boundary with high probability. This assures that the traffic analysis along the boundary could be performed.

Directed or Biased random walk In a standard random walk, the next node to visit is chosen *uniformly randomly* from all neighbors. This is the discrete analog of Brownian motion which is isotropic. The first variation to it is to define a non-uniform probability distribution on neighbors. In Phantom routing and a number of followup papers, a biased random walk is often adopted in which the neighbor that is farther away from the data source is chosen with higher probability, in order to quickly get to the regions far away

from the data source. For example, in sector-based directed random walk [72], a random walk from the west will be sent to a node to the east, chosen uniformly randomly. In hop-based directed random walk [72, 92], a random walk chooses the next hop uniformly randomly among only the nodes closer to the sink.

If the transition probability is non-uniform but determined (as in the two cases mentioned above), the harmonic measure as defined by the random walk will change. If the transition probability is known to the adversary, we can still calculate the harmonic measure under this change. Using the same idea presented in the paper one can still infer the source location. Therefore to make a biased random walk to be a countermeasure of the traffic analysis, we need to make the transition probability to be *unknown* to the adversary. One idea is to vary this transition probability randomly and periodically. However, in this case one should be careful about the transition probability configuration to make sure that the random walk is still ergodic[1] – otherwise there is no guarantee that the random walk covers the entire network and eventually delivers the message to the data sink.

[1] A random walk is ergodic when there is a unique stationary distribution. This requires the graph (implied by the edges with non-zero transitional probability) to be connected and non-bipartite.

6 Colon Flattening Using Heat Diffusion Riemannian Metric

6.1 Overview

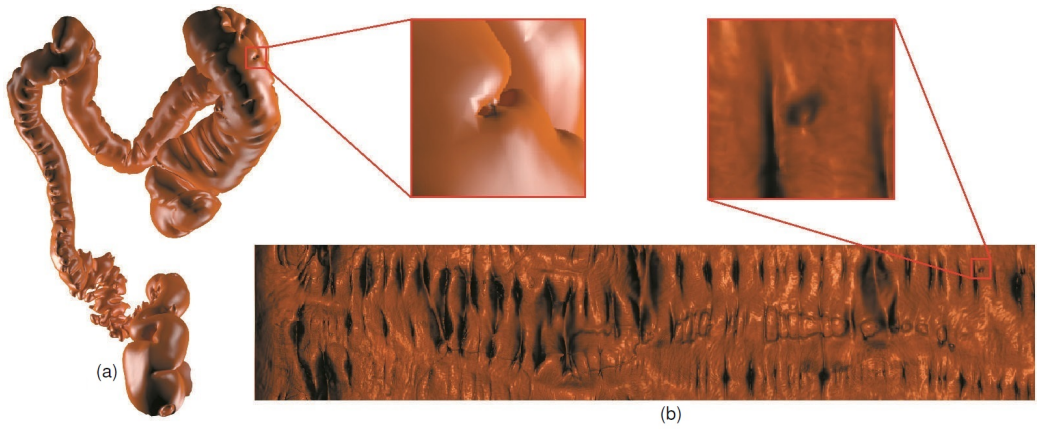

Figure 47: (a) A 3D colon model with topological noise, such as handles. A handle is shown in a close-up view. (b) The flattening of the 3D colon in (a) to a 2D rectangle using our method with heat diffusion Riemannian metric (flattening of only the transverse segment of the colon is shown). A colonic polyp (protrusion on colon wall) that is adjacent to a fold is shown in a close-up view.

Colorectal cancer is the second leading cause of cancer related mortality in the United States [61]. Optical colonoscopy (OC), whereby precancerous polyps (protrusions/bumps on the colon wall) can be located and removed, has been recommended for screening and has greatly reduced the mortality from colorectal cancer [21]. Virtual colonoscopy (VC) has been developed as viable non-invasive alternative to OC for screening purposes [58, 67]. VC is a non-invasive screening method, whereby a radiologist can explore a colon surface in a way similar to that of a gastroenterologist performing an OC. The radiologist is mainly interested in visualizing the inner surface of the colon where polyps might be

detected. VC uses computed tomographic (CT) scan of a patient's abdomen and provides a virtual fly-through visualization system through the virtual colon reconstructed from the CT scan [58]. VC has many advantages, including non-invasiveness, cheaper, faster, and higher patient tolerability [58]. However, VC has a fundamental problem, which it shares with OC. Due to the twisted nature of the colon and the numerous colonic haustral folds, the navigation using the inner endoluminal view is very challenging and sizable sections of the colon are not inspected, resulting in an incomplete examination. As a result, polyps hidden behind folds and sharp bends are missed. An efficient supplemental or alternative approach is flattening, where the colon is cut open and flattened onto a 2D plane. This not only facilitates comprehensive inspection of the colon but also reduces the time for inspection.

Several flattening techniques have been proposed for the colon surface, whereby the entire colon can be mapped from the 3D domain to a 2D rectangular domain. The colon mesh surface serves as the input. This mesh surface is extracted from the CT images by performing electronic cleaning, segmentation, and mesh extraction. However, the major problem here is that the extracted colon surface includes topological noise, such as handles, as shown in Fig. 47(a). A close-up view of a handle is also shown in Fig. 47(a). This topological noise is due to two reasons. The first is due to artifacts present in the CT scan. The second is due to the colon surface reconstruction method. Although many surface reconstruction methods are capable of generating water-tight surfaces from the CT data, the resulting models may still exhibit topological errors in the form of small handles. These high-frequency topological features unnecessarily increase the complexity of the colon model and make it unsuitable for subsequent processing tasks, such as colon flattening, 3D navigation, and polyp detection. Hence, in all previous methods for colon flattening, these unnecessary noisy features were either removed manually or by some topological denoising techniques. However, owing to the large surface of the colon, the use of these denoising methods is time-consuming and incurs high computational overhead.

In order to address this problem, we have introduced a new colon flattening algorithm using the heat diffusion metric, which is efficient, robust (insensitive to any topological noise) and shape-preserving. In our method, we use the extracted colon mesh directly without performing any topological denoising. To start, we compute the heat diffusion distances (HDDs) for the entire colon mesh (with noise). This HDD is used as a metric for the flattening. We compute this metric for an appropriate time step and replace the original Euclidean metric of the colon surface with this new metric. In the next step, we solve a Laplacian equation on the colon surface to obtain a harmonic form. By applying the Hodge star operator on this harmonic form, we obtain another form that is perpendicular to the harmonic form. Finally, we integrate these two metric forms on the colon surface to obtain the flattened colon. We render the flattened colon image using direct volume rendering to provide a view similar to that of the endoluminal view, as can be seen in Fig. 47(b). We demonstrate how the existing colon registration pipeline is turned more robust by using our method for colon flattening. Furthermore, we show that our method enhances the colon

navigation by preserving the important features, such as the polyps and folds. In addition, we also present an efficient handle detection and removal approach on the flattened colon using our method.

Our method has the following advantages: **1. Robustness:** Our method of using the heat diffusion metric for flattening is insensitive to topological noise, such as fake handles. As a result, by using our algorithm, the entire global shape is preserved after flattening in spite of having many handles. On the contrary, other methods, such as the Ricci flow, produce a highly distorted flattening result of the colon in the presence of noise. **2. Efficiency:** Our method is very efficient since we need to solve only one Laplacian equation for the entire colon surface. On the other hand, other methods, such as the holomorphic 1-form [59], require solving of $2g$ Poisson equations, where g is the number of handles on the colon surface. In case of a large number of handles (which is typical), our method performs far better than the other methods. **3. Shape preserving:** Our method is shape preserving. Even under the constraint of preserving the global shape, the local shape distortion is still under control. The final result obtained by using our method on a colon surface with noise is very similar to the one obtained by using other conformal based methods on the same colon surface with noise removed. Therefore, our method exhibits a good trade off between conformality and robustness.

The remainder of this work is organized as follows. Section 2 reviews the related literature and Section 3 provides the necessary theoretical background. The algorithm and its analysis is provided in Section 4. Section 5 compares our method with other well-known methods. Section 6 introduces a fast way to remove the handles on the flattened colon. Section 7 contains implementation and experimental results. Section 8 demonstrates the application of our colon flattening to polyp visualization and supine-prone colon registration. Section 9 contains concluding remarks and future work summary.

6.2 Related Work

Colon flattening is a method in which the entire inner surface of the colon is displayed as a succinct 2D image and has been used successfully for several medical imaging applications. Initial attempts to flatten the colon surface include iterative methods based on electrical field lines [7, 138, 139, 140], cartographic projection [102], and some others [8, 9, 85]. However, most of these methods deform the colon surface or do not preserve the local shapes well. Conformal geometry, an approach where the local angles are preserved, has been well established in the field of computer graphics, especially in the creation of texture maps [123]. Discrete Ricci flow is a more recent method of computing conformal maps of structures [65] and is very useful in the construction of geometric structures [64] and to obtain optimal surface parameterizations using inverse curvature maps [148]. Colon flattening techniques have been proposed using conformal mapping [53] and holomorphic 1-form parameterization [59]. The conformally flattened colon was used in the detection of colonic polyps [60] and supine-prone colon registration [150]. Further, surface parameteri-

zation using harmonic functions has also been used in graphics [133] and medical imaging of the brain [124] and blood vessels [156].

All the above methods require a mandatory pre-process of topological denoising because of the topological noise (fake handles), without which the flattening would be unsuccessful. While some of these methods use colon surfaces that have been manually denoised, the others utilize a topological denoising algorithm [52, 69, 155]. A fast topological denoising algorithm for conformal colon flattening has also been proposed [59]. Despite these attempts, topological denoising is still a time consuming and tedious process. On the other hand, our method does not require any topological denoising, as the heat diffusion metric utilized by our method is insensitive to topological noise. In addition, we propose an efficient way to detect and remove the handles on the flattened colon surface by using our approach.

Topologically robust diffusion geometry [18] has been mainly used for analysis of non-rigid shapes [10, 93, 97, 111] involving shape comparison, matching, and retrieval [99, 125]. The robust diffusion maps and diffusion distances [28, 79] have been proposed for shape matching [18], histogram comparison [86] and comparison of flexible molecular shapes [88]. However, it has never been used in a colon flattening pipeline. All the previous attempts of colon flatttening only consider the Euclidean metric and this is the first time a diffusion metric is used, by computing the HDD, thus making the colon flattening robust.

6.3 Theoretical Background

We present here brief theoretical fundamentals required to explain our colon flattening algorithm and to compare our method with the existing methods for colon flattening.

6.3.1 Conformal Mapping

Let S be a surface embedded in $\mathbb{R}^3$ and $\mathbf{g}$ be a Riemannian metric tensor that defines the inner products on tangent planes at every point on S. Let $\bar{\mathbf{g}}$ be another metric of S, such that

$$\bar{\mathbf{g}} = e^{2\varphi}\mathbf{g}, \tag{6.1}$$

where $\varphi : S \rightarrow \mathbb{R}$ is a scalar function defined on S. Then, by means of direct computation, it is easy to verify that $\bar{\mathbf{g}}$ preserves angles. Hence $\bar{\mathbf{g}}$ is said to be *conformal* (angle-preserving) to the original metric $\mathbf{g}$.

Given two surfaces with Riemannian metrics $(S_1, \mathbf{g_1})$ and $(S_2, \mathbf{g_2})$, consider a mapping $\phi : (S_1, \mathbf{g_1}) \rightarrow (S_2, \mathbf{g_2})$ between them. ϕ is said to be a *conformal mapping* if the pull back metric induced by ϕ satisfies the following relation:

$$\phi^* \mathbf{g_2} = e^{2\varphi}\mathbf{g_1}. \tag{6.2}$$

If a Riemannian surface $(S, \mathbf{g})$ is orientable, then for every point p on the surface, there exists a neighborhood $U(p)$ and a local coordinate system (u, v) on $U(p)$, such that the

metric $\mathbf{g}$ can be represented as: $\mathbf{g} = e^{2\varphi(u,v)}(du^2 + dv^2)$. Here the coordinates, (u, v) are called as *isothermal parameters* or *isothermal coordinates*. According to [25], we can cover the whole surface by a collection of isothermal coordinate charts. All isothermal coordinate charts form a *conformal structure* of the surface. The surface with a conformal structure is called a Riemann surface.

Theorem 6.1. *All oriented metric surfaces are Riemann surfaces.*

Conformal mapping, by definition is angle preserving. For example, if any two intersecting curves γ_1 and γ_2 are mapped to $f(\gamma_1)$ and $f(\gamma_2)$ by a conformal map f, then the intersection angle between γ_1 and γ_2 equals to the intersection angle between $f(\gamma_1)$ and $f(\gamma_2)$.

6.3.2 Hodge Theory

Let (x, y) be the isothermal (local) coordinates, then a differential 1-form denoted by ω has the local representation: $\omega = f(x, y)dx + g(x, y)dy$. Let d denote the *exterior differential operator*. If $f : S \to \mathbb{R}$ is a function defined on S, then the gradient of f, called the *exact 1-form*, is given by: $df = f_x dx + f_y dy$. The exterior differential operator acting on ω is given by:

$$d\omega = (g_x - f_y)dx \wedge dy. \tag{6.3}$$

If $d\omega = 0$, then ω is called a *closed 1-form*. Exact 1-forms must be closed. The space of all closed 1-forms is denoted as $Ker\ d^1$ and the space of all exact 1-forms is denoted by $Img\ d^0$. Then, the first dimensional cohomology group $H^1(S, \mathbb{R})$ is given by:

$$H^1(S, \mathbb{R}) = \frac{Ker\ d^1}{Img\ d^0} \tag{6.4}$$

Each element in $H^1(S, \mathbb{R})$ is a cohomological class. Two closed 1-forms are said to be in the same class if they differ by an exact 1-form.

Under isothermal parameters, the *Hodge star* operator is defined as:

$$^*(fdx + gdy) = -gdx + fdy, ^*f = fdx \wedge dy, ^*(gdx \wedge dy) = g. \tag{6.5}$$

The co-differential operator δ is defined as $\delta = *d*$. A differential 1-form ω is said to be a *harmonic 1-form*, if $d\omega = 0$ and $\delta\omega = 0$. All harmonic 1-forms form a group which is isomorphic to the first cohomology group based on the following Hodge theorem:

Theorem 6.2 (Hodge)**.** *Each cohomological class has a unique harmonic 1-form.*

Current work focuses on genus zero surfaces with mutiple boundaries, $\partial S = \gamma_0, \gamma_1 \cdots \gamma_n$. Then, the first cohomology is n dimensional. One can choose n harmonic 1-forms $\{\omega_k\}, 1 \leq k \leq n$, forming the basis of $H^1(S, \mathbb{R})$ by: $\int_{\gamma_j} \omega_i = \delta_i^j$, where δ_i^j is the Kronecker symbol.

6.3.3 Holomorphic Differentials

Suppose ω is a harmonic 1-form, then its Hodge dual ${}^*\omega$ is also a harmonic 1-form. The pair, $\eta = \omega + i^*\omega$ is called a *holomorphic 1-form*. On a Riemann surface, all the holomorphic 1-form form a group, which is isomorphic to the first cohomology group.

The holomorphic 1-form can be treated as the complex derivative of a conformal map $\phi : S \to \mathbb{C}$, and the conformal map ϕ can be recovered by integrating the holomorphic 1-form $\phi = \int \eta$. In practice, from the harmonic 1-form basis $\{\omega_k\}$, we can construct the holomorphic 1-form basis $\{\eta_k = \omega_k + i^*\omega_k\}, k = 1, 2, \cdots, n$. Then we can construct any holomorphic 1-form by linearly combining the basis, and obtain the conformal mapping by integration.

6.3.4 Heat Diffusion Distance

The *heat diffusion* process on the surface is governed by a partial differential equation defined as follows:

$$\frac{\partial u(p,t)}{\partial t} = -\Delta_{\mathbf{g}} u(p,t), \tag{6.6}$$

where $u(p,t)$ is the temperature or heat at a point $p \in S$ at time t and $\Delta_{\mathbf{g}}$ is the *Laplace-Beltrami Operator* (LBO) defined as:

$$\Delta_{\mathbf{g}} = e^{-2\varphi(x,y)}(\frac{\partial^2}{\partial x^2} + \frac{\partial^2}{\partial y^2}). \tag{6.7}$$

where $e^{-2\varphi(x,y)}$ represents the area term. The solution to Eq. 6.6 with the initial condition, $u(p,0) = \delta(p-q)$, is called the *heat kernel* and is denoted as $K_{\mathbf{g},t}(p,q)$. Intuitively, the heat kernel can be interpreted as the amount of heat transferred from a point p to a point q in a given time t.

The LBO has an eigendecomposition of the form: $\Delta_{\mathbf{g}}\Phi_k = \lambda_k \Phi_k$, $k = 0, 1, 2, \cdots$, where $0 = \lambda_0 < \lambda_1 \leq \lambda_2 \leq \lambda_3 \cdots$ are the eigenvalues and $\Phi_k : S \to \mathbb{R}$ are the corresponding eigen functions. Then, the heat kernel is defined as:

$$K_{\mathbf{g},t}(p,q) = \sum_{i=0}^{\infty} e^{-\lambda_i t}\Phi_i(p)\Phi_i(q) \tag{6.8}$$

Using the definition of the heat kernel, the *heat diffusion distance* (HDD) at a time t is then given by:

$$d_{\mathbf{g},t}(p,q) = K_{\mathbf{g},t}(p,p) + K_{\mathbf{g},t}(q,q) - 2K_{\mathbf{g},t}(p,q) \tag{6.9}$$

An equivalent spectral expression of the heat diffusion distance is:

$$d^2_{\mathbf{g},t}(p,q) = \int_S |K_{\mathbf{g},t}(p,r) - K_{\mathbf{g},t}(q,r)|^2 dr = \sum_{i=1}^{\infty} e^{-2\lambda_i t}(\Phi_i(p) - \Phi_i(q))^2 \tag{6.10}$$

where r is some point on the surface S. Eq. 6.10 shows that the diffusion distance is the L^2 distance between two probability distributions of Brownian motions (random walks),

$K_{\mathbf{g},t}(p,r)$ and $K_{\mathbf{g},t}(q,r)$. Essentially, the mapping, $p \rightarrow (e^{-\lambda_1 t}\Phi_1(p), e^{-\lambda_2 t}\Phi_2(p), \cdots)$ embeds the surface to an infinite dimensional functional space. The definition in Eq. 6.10 shows that the heat diffusion distance is the same as the classical Euclidean metric in this functional space. Therefore, the heat diffusion distance is a Riemannian metric.

Theorem 6.3 (Lafon and Coifman)**.** *The heat diffusion distance defined in Eq. 6.10 is a Riemannian metric.*

6.4 Algorithm

With the theory described above, we are ready to introduce our flattening algorithm using the heat diffusion metric. Let the original input surface with handles be approximated by a triangular mesh M. This mesh M has a number of handles varying from tens to hundreds. Let γ_0 be the outer boundary and $\gamma_k, 1 \leq k \leq n$ be n inner boundaries or holes (holes are not handles) of M with topological noise. A larger value of n (greater number of holes) indicates a more complicated topology of M. Let V be the vertex set and E be the edge set of the mesh M. We denote v_i as the i^{th} vertex, $[v_i, v_j]$ as the edge, $[v_i, v_j, v_k]$ as the face, and θ_i as the corner angle at vertex v_i. Let the functions on M be approximated by the piecewise linear functions defined on the vertices, $f(v_i)$.

6.4.1 Heat Diffusion Metric

The heat diffusion distance (HDD) given by Eq. 6.10, introduced by Lafon et al. [28, 79], is computed as an average of all paths connecting two points on the surface. The HDD (diffusion process) can be obtained by the convolution of the signal and its heat kernel. Consequently, the Laplacian surface smoothing is achieved by performing diffusion on the surface that filters out the high frequency components. However, as the surface changes during smoothing, the heat kernels are also evolving. The evaluation of HDD smooths out the small perturbations (e.g., handles) on the surface and hence makes the HDD insensitive to the topological noise. As a result, the flattening algorithm using the HDD is more robust.

Using the vertex positions, we compute the edge lengths directly as $l_{ij} = |v_i - v_j|$. We call this set of edge lengths the induced Euclidean metric. We compute the heat diffusion metric $\mathbf{g}$ by using the induced Euclidean metric. For every edge in the mesh we evaluate a new edge length value (HDD) and we call this set of new edge lengths the heat diffusion metric. For every face, $[v_i, v_j, v_k]$ of the mesh M, the corner angles are computed by using the Euclidean cosine law as $\theta_i = \cos^{-1}((l_{ij}^2 + l_{ki}^2 - l_{jk}^2)/(2l_{ij}l_{ki}))$. We evaluate the cotangent edge weight for every edge in M by using this corner angle to obtain a weighted adjacency matrix $W := (w_{ij})$, where w_{ij} is the cotangent edge weight of the edge $[v_i, v_j]$. The cotangent edge weight is defined as follows [106]:

Definition 6.1 (Cotangent Edge Weight)**.** *Suppose edge $[v_i, v_j]$ is adjacent to two faces $[v_i, v_j, v_k]$ and $[v_j, v_i, v_l]$, then the weight of the edge is given by:* $w_{ij} = (\cot\theta_k + \cot\theta_l)/2$.

In the next step, using W and the function values at the vertices, the LBO at each vertex is computed to obtain a Laplace-Beltrami matrix, L. In the discrete case, the LBO on a vertex is defined as follows:

Definition 6.2 (Discrete Laplace-Beltrami Operator)**.** *Suppose edge $[v_i, v_j]$ is adjacent to two faces $[v_i, v_j, v_k]$ and $[v_j, v_i, v_l]$, then the Laplace-Beltrami Operator, $\Delta_{\mathbf{g}}$ on vertex v_i is given by $\Delta_{\mathbf{g}} f(v_i) = \sum_{[v_i,v_j]\in E} w_{ij}(f(v_j) - f(v_i))$.*

We perform eigendecomposition of L and compute the eigenvalues and their corresponding eigen functions. Using these eigenvalues and eigen functions, we finally compute the HDD lengths of every edge in M using Eq. 6.10. The set of all new edge lengths forms the heat diffusion metric $\mathbf{g}$.

The number of eigenvalues and the number of time steps used have an effect on the heat diffusion metric. In our case, we have used the first 50 eigenvalues and the corresponding eigen functions to calculate the HDD for the edges. Also, we choose the value of time step t in Eq. 6.10 to be 8 for all our cases. These respective values have been chosen experimentally by assessing the quality of the mesh that is obtained by replacing the edge lengths with the HDD values. The quality of the mesh is assessed by measuring the "closeness" of each of its faces to an equilateral triangle. For each face of the mesh we compute the ratio of its circumradius to two times its inradius. For an equilateral triangle, this ratio is equal to 1. The faces with ratio > 0.6 are considered as good quality faces and < 0.6 are considered as bad quality faces. We obtain the histogram of the faces of the mesh based on their ratio values. Two meshes are said to be of similar quality if they have a comparable number of bad quality faces and also comparable histograms (using L^2-norm comparison). We have observed that by increasing the number of eigenvalues the quality of the obtained mesh improves. However, the quality did not change much after 50 eigenvalues.

The value of the time step represents the length of the path over which the heat diffusion metric is averaged. Each handle has two loops, the handle loop and the tunnel loop [31]. In general, their lengths are about 8 edges. Hence, we chose the value of t to be 8 so that only the handles are filtered out. If the value of t is too small, the heat diffusion metric becomes close to the induced Euclidean metric. On the other hand, if the value of t is too large, the heat diffusion metric will smooth out all the features on the surface that would make two different surfaces yield the same result.

We articulate the difference between the HDD and the geodesic distance by means of a simple experiment. For this, we consider a hand model as our input where the index finger is touching the thumb as shown in Fig. 48(a). In Fig. 48(b) we detached the two fingers, by manually cutting both the fingers at the location indicated by the red arrow, so that the topology in the two hand models is totally different. In both models, we choose two points p and q such that p is a point on the tip of the pinky finger and q is a point on the thumb nail. By using these two points as epicenters, for any point x on the surface, we compute the following distance function, f:

$$f(x) = d(p, x) + d(q, x) - d(p, q) \tag{6.11}$$

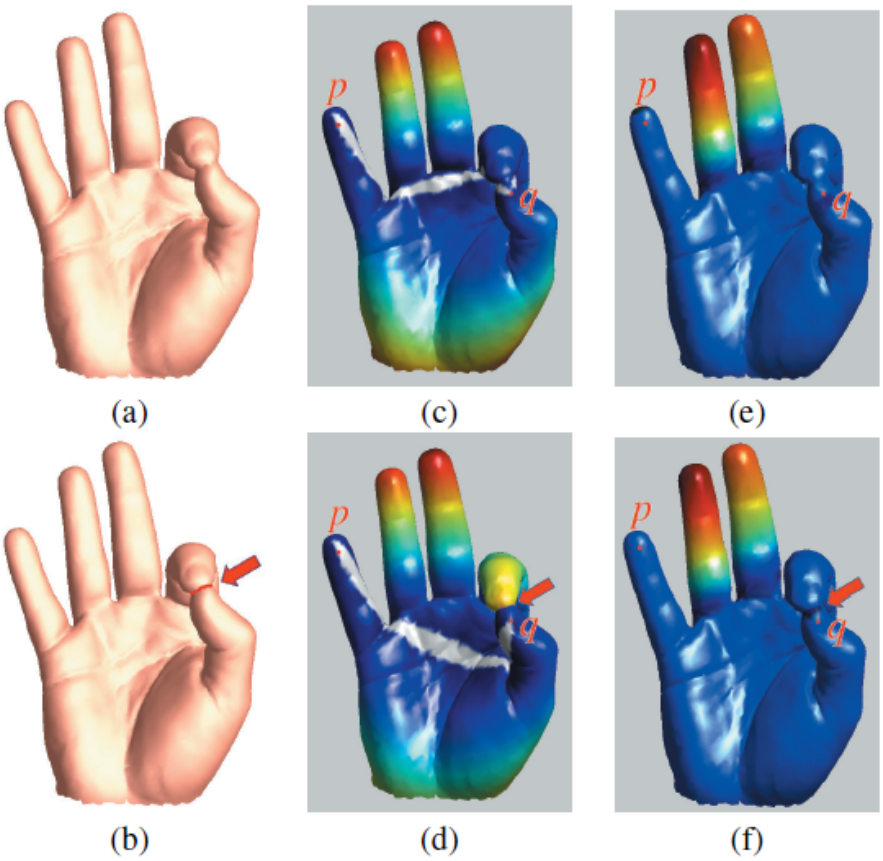

Figure 48: Comparison between geodesic distance and HDD using a hand model with (a) thumb and index finger touching, and (b) thumb and index finger detached by manually cutting at the location indicated by the red arrow. With points p and q as epicenters, color encoded (c) geodesic distance function of (a); (d) geodesic distance function of (b); (e) HDD function of (a); (f) HDD function of (b). When the topology changes in (b), (d) changes drastically (the geodesic path between p and q in white also changes), while (f) is not affected and is consistent.

Here, d can represent either the HDD or the geodesic distance. We evaluate f using both HDD and geodesic distance values for both hand models and color encode f. The color changes from blue to red with increasing f values. Figs. 48(c) and (d) show the color encoded distance function using geodesic distance values for the hand models in Figs. 48(a) and (b), respectively. It can be clearly seen that the distance function changes dramatically when the topology changes. We can also see that the geodesic distance between the points p and q, shown by a white path, has changed when the topology changed. On the other

hand, Figs. 48(e) and (f) show the color encoded distance function using HDD values for the hand models in Figs. 48(a) and (b), respectively. It can be seen that the results are more consistent, showing that the topological changes do not affect the HDD function. This experiment shows that HDD is more robust to topological noises, and hence a better choice as compared to geodesic distance.

In fact, the HDD of an edge $[p, q]$ and the original edge length are completely different. Theoretically, the HDD $d_{\mathbf{g},t}(p, q)$ is related to all paths starting from p and ending at q with length t. When t is large, the random paths cover large regions of the surface. Thus, HDD is a global concept. In contrast, the edge length of $[p, q]$ is local. In other words, the HDD is inversely related to the connectivity of points p and q, by paths of length t, hence insensitive to topological noises.

6.4.2 Conformal Flattening Algorithm Based on HDD

We map the surface M with the heat diffusion Riemannian metric $\mathbf{g}$ conformally onto $\mathbb{C}$ which represents a (u, v)-planar domain. For this, we first replace all the edge lengths in M with the edge lengths from the heat diffusion metric and denote the new mesh also by M. Since M has n inner boundaries, the cohomology group and therefore its harmonic 1-form basis are n dimensional (Theorem 3.2).

The first step of our algorithm is to compute the basis for exact harmonic 1-forms of M. To compute the exact harmonic 1-forms, we first compute the harmonic functions, $f_k : M \to \mathbb{R}$ by solving the following Dirichlet problem on M for each inner boundary component γ_k:

$$\begin{cases} \Delta_{\mathbf{g}} f_k &\equiv 0 \\ f_k|_{\gamma_k} &= 1 \\ f_k|_{\gamma_i} &= 0, 0 \leq i \leq n, i \neq k \end{cases} \tag{6.12}$$

The Laplace matrix $\Delta_{\mathbf{g}}$ in Eq. 6.12 is positive definite and thus, non-degenerate. The stability of the Laplace matrix, measured by its condition number [74], depends on the mesh triangulation quality. In our case, the triangles in the mesh are close to Delaunay (Laplace matrix has a good condition number) and thus the linear system is stable. In the discrete case, the harmonic function is defined as follows:

$$\Delta_{\mathbf{g}} f(v_i) = \sum_{[v_i, v_j] \in E} w_{ij}(f(v_j) - f(v_i)) = 0. \tag{6.13}$$

Eq. 6.13 is the discrete Laplacian equation. The discrete harmonic function satisfies the *mean value* property where a function value at a vertex $f(v_i)$ is equal to the mean of the function values of the neighboring vertices, $f(v_j)$'s. Thus, Eq. 6.13 is equivalent to:

$$f(v_i) = \sum_{[v_j, v_i] \in E} \frac{w_{ij}}{\sum_k w_{ik}} f(v_j), \tag{6.14}$$

The discrete harmonic function f_k on M is thus computed by using Eq. 6.14 and by solving the linear system in Eq. 6.12. For solving the linear system we use the publicly

available UMFPACK library. Once the harmonic function f_k is obtained, the exact harmonic 1-form df_k is computed as the gradient of the harmonic function as follows:

$$df_k([v_i, v_j]) = f_k \partial [v_i, v_j] = f(v_j) - f(v_i). \tag{6.15}$$

The n-dimensional exact harmonic 1-form basis is represented by $\{df_1, df_2, \cdots, df_n\}$. The next step of our algorithm is to compute the holomorphic 1-form basis. For this we compute the Hodge star of the exact harmonic 1-form $^*(df_k)$ using Eq. 6.5, which is called the conjugate harmonic 1-form. The conjugate harmonic 1-form is also harmonic (Section 3.3). Intuitively, the exact harmonic 1-form and its conjugate harmonic 1-form are orthogonal everywhere. While using the Hodge star operator, in general, a regularization step is performed based on Hodge decomposition to decompose $^*(df_k)$ into exact, coexact and harmonic components [128]. The exact and coexact components are discarded and only the harmonic component is retained. However, in our method, since we use a reasonably good resolution mesh the Hodge star operator is accurate enough to avoid the regularization step. Finally, by pairing each base exact harmonic 1-form with its conjugate, we obtain the set of basis for the holomorphic 1-form on M as $\eta_k = df_k + i^*(df_k)$. Then, the holomorphic 1-form basis is represented by $\{\eta_1, \eta_2, \cdots, \eta_n\}$.

In the final step, using the holomorphic 1-form basis, we compute the induced conformal mapping $\phi : M \rightarrow \mathbb{C}$ by integration that maps the surface M to a planar domain $\mathbb{C}$. To start with, for each of the inner boundaries γ_k, we find the corresponding shortest paths τ_k connecting γ_k to the outer boundary γ_0. We cut M along one of these τ_k's to obtain a simply connected mesh $\bar{M}$. Then, we compute a unique holomorphic 1-form $\eta = \sum_{k=1}^{n} \lambda_k \eta_k$, $\lambda_k \in \mathbb{R}$, as a linear combination of the holomorphic 1-form basis, such that it satisfies the following topological condition:

$$Img \int_{\gamma_0} \eta = 2\pi, Img \int_{\gamma_k} \eta = -2\pi, Img \int_{\gamma_i} \eta = 0, i \neq 0, k \tag{6.16}$$

where Img denotes the imaginary part. Here, λ_k's are a set of unknowns which are obtained by solving the linear system in Eq. 6.16. We then choose a base vertex $p \in \gamma_0$. For any vertex $q \in \bar{M}$, we choose an arbitrary integration path connecting p and q in $\bar{M}$. Finally, the conformal mapping is obtained by integrating η over this path as follows:

$$\phi(q) = exp(\int_{p}^{q} \eta) \tag{6.17}$$

Eq. 6.17 maps the surface M to a 2D annulus. Note that several conformal maps are possible by changing the topological conditions in Eq. 6.16. If we just compute the integral in Eq. 6.17 without the exponential, then the mapping computed will map M onto a rectangle.

Since the mesh $\bar{M}$ is simply connected and η is holomorphic, the integration result is independent of the choice of the path and hence any arbitrary path can be chosen for integration to obtain the conformal mapping. In fact, the results after integration by choosing

different paths are the same. In Eq. 6.17, we are effectively integrating df_k and $^*(df_k)$ to obtain the conformal mapping of the mesh. Both the fields df_k and $^*(df_k)$ are harmonic 1-forms and since any harmonic 1-form is closed (Section 3.2), it implies that both these fields are locally integrable. In our case, we assume that the fake handles on the surface are tiny (which is typical), which implies that the corresponding tunnel and the handle loops are short [31]. Hence, the integration of the conjugate harmonic 1-form $^*(df_k)$ (Hodge star of exact harmonic 1-form df_k) is very close to zero. In practice, the harmonic 1-forms corresponding to the tiny handles can be neglected. Since the complex derivative (η) in Eq. 6.17 is a holomorphic 1-form, it is equivalent to saying that the mapping obtained by integration satisfies the Cauchy-Riemann equation [82, 98] (Section 3.3). This proves that our mapping is indeed conformal with respect to the given heat diffusion metric.

We summarize our conformal mapping algorithm in Algorithm 9. Our flattening algorithm requires the input mesh to be a two dimensional manifold. In the entirety of our algorithm, we assume that the handles on the mesh surface are tiny. If the handles are large, then the harmonic 1-forms corresponding to the handles can no longer be ignored and it in turn affects the integration for computing the conformal maps. Moreover, we assume that the input mesh surface has good resolution so that the Hodge star regularization is unnecessary.

Algorithm 9 Heat diffusion metric based discrete conformal mapping.

Input: Surfaces M, heat diffusion metric $\mathbf{g}$.

Output: The conformal parameterization of M.

1. Replace the edge lengths in M with edge lengths from $\mathbf{g}$.
2. Compute the harmonic function by solving the linear system 6.12.
3. Compute exact harmonic 1-form, $df([v_i, v_j]) = f(v_j) - f(v_i)$ for each edge.
4. Compute the Hodge star of df by using Eq. 6.5.
5. Compute special holomorphic 1-form η satisfying the topological condition in Eq. 6.16.
5. Integrate η to get the final 2D coordinate for each vertex, using Eq. 6.17.

6.4.3 Generality of our Algorithm

As described above, our flattening algorithm is general and can handle flattening problems with complicated topologies containing any number of inner boundaries or holes. We now illustrate the different steps of our flattening algorithm using a genus zero surface with an arbitrary number of holes. For this, we use a complicated topology of a human face surface S with four boundary components, namely γ_0 is the outer boundary and γ_1, γ_2 and γ_3 are the inner boundaries. Thus, $n = 3$ in this case. We first evaluate the heat diffusion Riemannian metric $\mathbf{g}$ for the face surface. Then, we compute the corresponding exact harmonic 1-forms (df_1, df_2, df_3), conjugate harmonic 1-forms ($^*(df_1), ^*(df_2), ^*(df_3)$) using Hodge star, and holomorphic 1-forms (η_1, η_2, η_3), as described earlier. All the 1-forms can be visualized by using level sets. Figs. 49(d), (e) and (f) show the level set visualization of the exact harmonic 1-form (df_1), the conjugate harmonic 1-form ($^*(df_1)$), and the holomorphic 1-form (η_1), respectively, with respect to the inner boundary γ_1, that is $k = 1$ in Eq. 6.12. Similar results can be obtained with respect to the inner boundaries γ_2 and γ_3 as well.

Now, using the holomorphic 1-form basis, we construct a conformal mapping from the input surface $(S, \mathbf{g})$ to a planar annulus domain by integration using Eq. 6.17. This integration is carried out along an arbitrary path using the special holomorphic 1-form (linear combination of η_1, η_2 and η_3) satisfying Eq. 6.16. This method is popularly known as *slit mapping* [142, 149] where one of the inner boundaries of S is mapped to a circle and all the remaining boundaries are mapped to the concentric circular slits. Fig. 49(c) shows the flattening result of the face where γ_0 is mapped to the outer radius, γ_1 is mapped to the inner radius, and γ_2 and γ_3 are mapped to the slits using our algorithm. To obtain the flattening in Fig. 49(c), we cut the face along the shortest path connecting γ_1 and γ_0 and solve Eq. 6.16 also over γ_1. Two additional slit map results are possible with respect to the other two inner boundaries, γ_2 and γ_3. If we map a checker board pattern onto the flat annulus in Fig. 49(c) and have it correspondingly mapped back onto Fig. 49(a), the angles and shapes inside the checker board are preserved since our algorithm is conformal. This fact is confirmed in Fig. 49(b), illustrating that our algorithm is indeed angle (shape) preserving.

6.5 Experimental Results

6.5.1 Colon Flattening

The colon surface is a special case with a simple topology (cylindrical) having only two boundary components, namely γ_0 and γ_1 ($n = 1$). Thus, the colon surface has only one holomorphic 1-form base, η_1. Then, the unique holomorphic 1-form η for integration is obtained as $\eta = \lambda_1\eta_1$, satisfying the condition: $Img \int_{\gamma_0} \eta = 2\pi, Img \int_{\gamma_1} \eta = -2\pi$, which is a simpler form of Eq. 6.16. Finally, a conformal mapping of the colon surface is obtained by integration using Eq. 6.17. However, in the case of colon flattening, the common practice

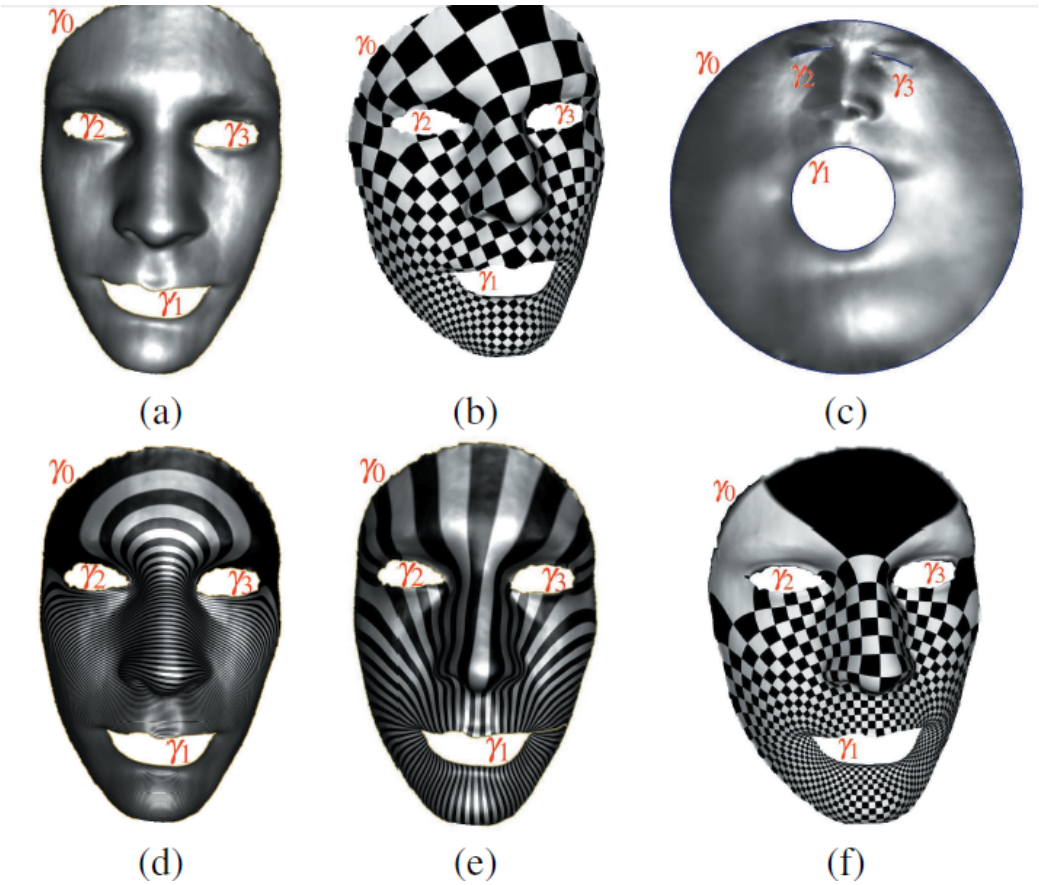

Figure 49: The flattening of (a) human face surface with outer boundary γ_0 and inner boundaries $\gamma_1, \gamma_2, \gamma_3$ using our algorithm. (b) Checker board mapping of (a), showing that angles are well preserved. (c) Slit map showing the flattening of (a). Level set visualization of: (d) exact harmonic 1-form, df_1 with respect to γ_1; (e) Hodge star of (d), ${}^*(df_1)$; (f) holomorphic 1-form, η_1 by combining (d) and (e).

is to map the colon onto a rectangle since it is the more intuitive way to visualize the colon surface. Hence, we compute the logarithm of the integral in Eq. 6.17 which now maps the colon to a rectangle instead of an annulus. In other words, we are effectively only computing the integral part of Eq. 6.17 without the exponential. Thus, the colon surface is conformally mapped to a planar rectangle to obtain a flattened rectangular map of the colon surface. We chose conformal mapping for the colon flattening due to the following main reason: In VC, after the colon surface is flattened, it is mandatory to preserve the local shapes. Conformal maps, by definition, are angle preserving (local shape preserving) (Section 3.1). Consequently, polyps can still be identified based on their circular shape on the flattened colon image.

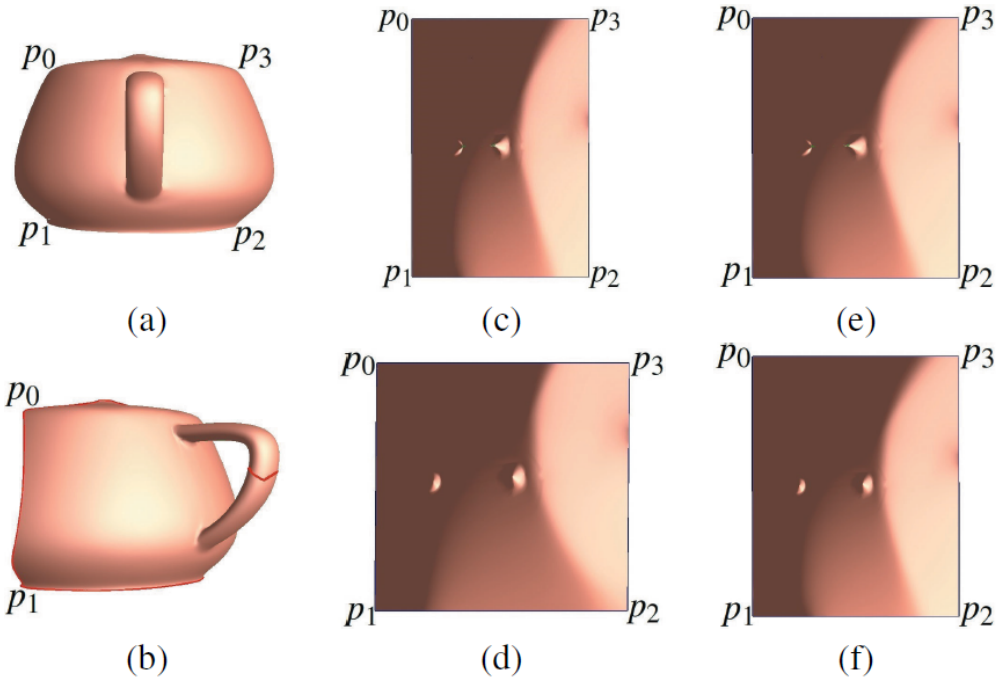

Figure 50: Comparison of our flattening algorithm using the original Euclidean metric and heat diffusion metric. (a) Teapot patch with handle; (b) Teapot patch with handle cut along a loop, shown in red; (c) Conformal module of (a) using Euclidean metric; (d) Conformal module of (b) using Euclidean metric; (e) Conformal module of (a) using heat diffusion metric; (f) Conformal module of (b) using heat diffusion metric.

Our conformal flattening algorithm can be used either with the heat diffusion metric or with the original Euclidean metric. We now show that our flattening algorithm is more robust using the heat diffusion metric (obtained using the HDD) when compared to using the original Euclidean metric. For this, we consider a patch of a teapot surface with the handle and p_0, p_1, p_2, p_3 being four corners on the boundary as shown in Fig. 50(a). We now manually cut the handle along a loop indicated by the red line in Fig. 50(b). We then use our flattening algorithm to map both the teapots in Figs. 50(a) and (b) to a planar rectangle by using the heat diffusion metric as well as the original Euclidean metric. The teapot handle is collapsed onto the plane after flattening. Figs. 50(c) and (d) show the conformal flattening results by using the original metric for Figs. 50(a) and (b), respectively. Figs. 50(e) and (f) show the conformal flattening results by using the heat diffusion metric for Figs. 50(a) and (b), respectively. When a surface is conformally mapped to a planar rectangle, the ratio between the height and the width of the rectangle is called the *conformal module* of the surface. It can be clearly seen that the conformal modules based on the original metric

changed much, due to the cutting of the handle (change in topology) whereas the conformal modules based on the heat diffusion metric are similar. These experimental results confirm that the heat diffusion metric is preferrable for our flattening algorithm than the original metric, due to its insensitivity to topological noise.

6.5.2 Comparison with Existing Methods

The current approach is much more efficient and robust to topological noise when compared to previous methods. Here, we compare our method to the well known conventional holomorphic 1-form method, the conventional topological denoising method, and the Ricci flow method and show that ours fairs better for colon surfaces with noise.

Conventional Holomorphic 1-form Method: In the conventional holomorphic 1-form method, the most time consuming part is solving the Poisson equations [59]. Every handle on the mesh corresponds to two cohomological classes. Since the harmonic 1-forms are computed for all the cohomological classes, if the colon surface has g handles, then the Poisson equations in the conventional holomorphic 1-form method need to be solved $2g$ times [59]. In practice, there may be more than a hundred fake handles and therefore the computation is very time consuming. Hence, though theoretically this method can also be used for flattening noisy colons, it is not efficient. On the contrary, in our method, we need to solve only a single Laplace equation. This is because we only consider the cohomological class corresponding to a cylinder and ignore all the other classes (the colon is roughly cylindrical). Hence we compute only one harmonic 1-form, by solving only one Laplace equation given by Eq. 6.12. Thus, our method is virtually independent of the number of handles, thereby increasing the efficieny.

Conventional Topological Denoising: In the conventional topological denoising method, initially, for each handle, two loops, namely the handle loop and the tunnel loop are computed [31]. Then, the handle is cut along one of these loops, which are then filled with two small disks to ultimately remove the handles. In this method, it is extremely challenging and time consuming to compute the two loops for each handle since there might be hundreds of handles. Moreover, the topological surgery on the meshes is also complicated. In our method, by virtue of the metric used, all the fake handles present on the colon surface are collapsed and flattened on the destination plane. Consequently, all the vertices near the handles have non-zero curvatures. Thus, by simply evaluating the Gaussian curvature of the vertices the handles can be easily located (handles occur at vertices with non-zero curvatures). The handles can then be removed by removing the neighborhood of these vertices with non-zero curvature and filling small disks into the holes. This provides a simpler and more efficient way to remove handles compared to the traditional denoising method. We provide more elaborate details of the handle detection and removal using our method in Section 6.

Ricci Flow Method: The Ricci flow method deforms the Riemannian metric to the constant curvature uniformization metric [65], which induces constant curvatures everywhere.

This constant is solely determined by the topology of the surface. The colon surface is a topological cylinder. Hence, the uniformization metric induces zero Gaussian curvature for the interior points, and a zero geodesic curvature along the boundaries. However, for colon surfaces with topological noise (fake handles), the Ricci flow converges to a negative constant curvature metric and hence they cannot be flattened onto the Euclidean plane. Therefore, the Ricci flow method is intrinsically vulnerable to topological noise. On the contrary, our method is insensitive to topological noise and a robust flattening is achieved.

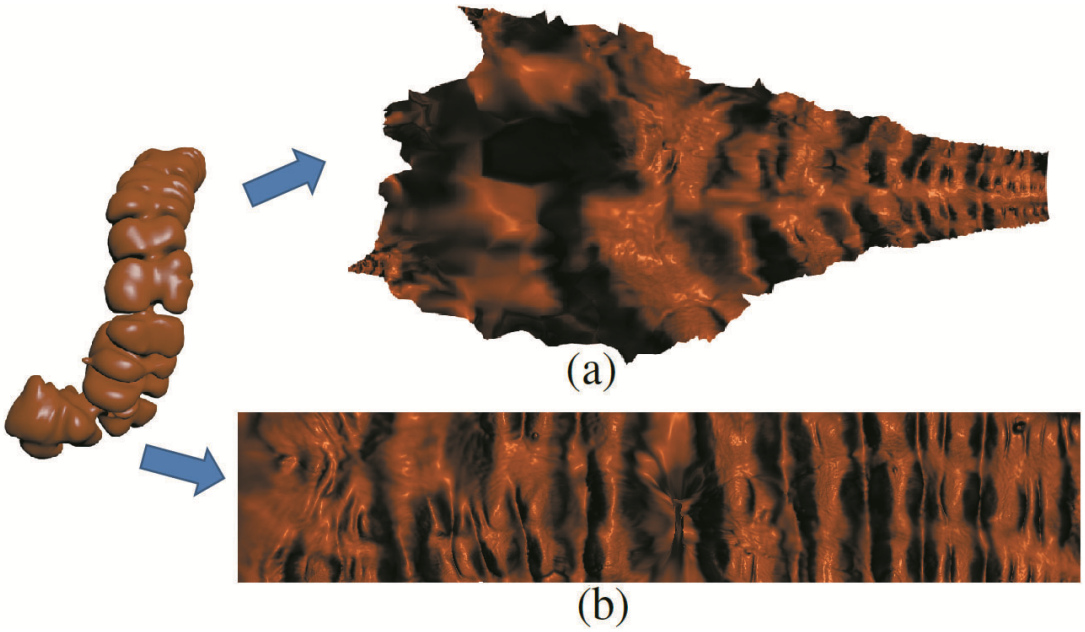

Figure 51: The flattening of the ascending segment of a colon using (a) Ricci flow, and (b) our method.

For comparison, we show in Fig. 51 a flattened result of the ascending colon segment, using both ours and the Ricci flow approach. Fig. 51(a) shows the flattening result of the colon segment using the Ricci flow method and Fig. 51(b) shows the flattening result of the colon segment using our method. It can be clearly seen that the Ricci flow flattening is non-regular and the global shape is lost. This is because the Ricci flow method is sensitive to noise, such as handles. On the other hand, the colon flattening using our approach is regular and the entire global shape is preserved.

Model Num.	#Faces	Time (sec) Ricci Flow	Time (sec) Our Method
192 (Supine)	56,800	125.7	11.2
192 (Supine A)	12,500	35.6	3.4
192 (Supine T)	23,100	62.2	5.2
192 (Prone)	52,900	112.5	12.3
192 (Prone A)	12,800	33.6	3.3
192 (Prone T)	22,700	57.2	5.4
241 (Supine)	55,900	121.5	11.4
241 (Prone)	53,100	110.8	11.3

Figure 52: Comparison of the running times of our colon flattening approach with the colon flattening using the Ricci Flow method.

We compared our method with the Ricci flow approach, in terms of the colon flattening running times. Table 52 shows the comparison results using different colon models and segments. The first column shows the number and segment of the colon model used. 192 and 241 are model numbers of the colon, A represents the ascending segment of the colon and T represents the transverse segment. The second column shows the number of faces in the colon model. The third column gives the time taken (in sec) for flattening the colon models using the Ricci flow method. Finally, the fourth column gives the time taken (in sec) for flattening using our method. Table 52 shows that for all the colon models, our method is an order of magnitude faster than the Ricci flow method. Note that the timing details provided in Table 52 only show the time taken for flattening and do not include the time taken for the metric evaluation. Since both methods use different metrics, for the sake of comparison we only use the time taken for flattening. All the experiments were conducted on a system equipped with an Intel(R) Xeon(R) CPU with a 1.87 GHz processor.

6.5.3 Handle Detection and Removal

Our method of colon flattening using the heat diffusion metric is insensitive to topological noise and hence the flattening process does not require any denoising as a mandatory pre-processing step. Nonetheless, it is important to remove these topological artifacts such as the tiny handles, so that they do not obstruct any further processing of the data, that is, if the user wants to perform any further simplification of the colon data for other applications. In all the previous methods, the handles were detected and removed directly on the 3D

model. Hence, only a limited visualization of the location of the handles was obtained. On the contrary, in our method, we detect the handles on the flattened colon surface and thus obtain a clear visualization of the handles. This helps us to know the location of the handles better.

By using the heat diffusion metric, the region around the handles is smoothed while flattening. As a result, a small overlapped region is formed at the location of the handles. In other words, a non-zero curvature is formed for all the vertices in the regions with handles. Thus, the problem of handle detection would simply boil down to the problem of finding all the vertices with non-zero curvature. Therefore, we calculate the Gaussian curvature for each vertex of the colon mesh. We then mark all the vertices which have a non-zero Gaussian curvature. These vertices are nothing but the vertices around the handles. In this way, all the handles can be detected in a fast and effective way.

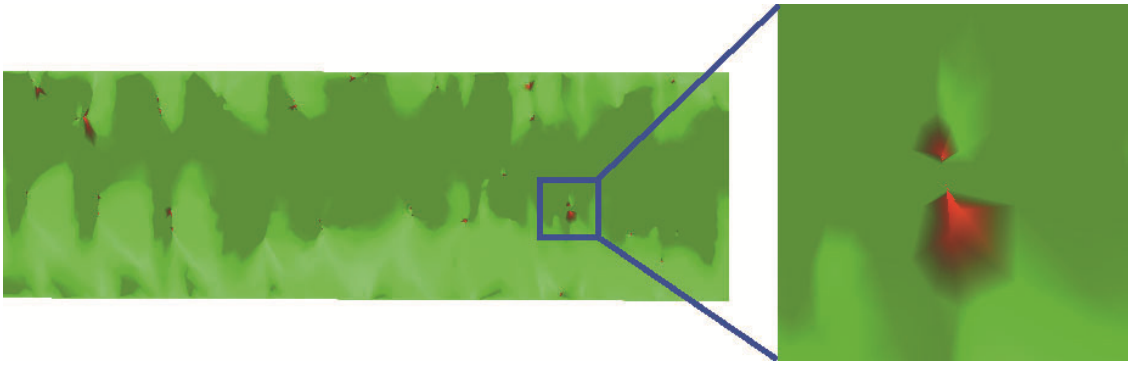

Figure 53: Handles detected by computing the Gaussian curvature for each vertex. Red areas indicate handles detected (one shown in close-up view) and the green area shows the zero Gaussian curvature region.

Fig. 53 shows the result obtained by using our approach to detect handles for one third segment of a flattened colon surface (starting from the cecum on the left). The green color represents the regions with zero Gaussian curvature and the red color represents the regions with non-zero Gaussian curvature. Hence, all the red regions on the colon surface in Fig. 53 show the handles detected using our approach. Fig. 53 also shows the close up view of a red-colored region, which confirms that it indeed is a handle (flipped triangles). Once all the handles have been detected, they can be easily removed. For this, we delete the faces

around the vertices with non-zero Gaussian curvature (red regions representing handles) and subsequently fill the resulting holes with small disks. Thus, all the handles are removed to obtain a flattened colon surface free of topological noise.

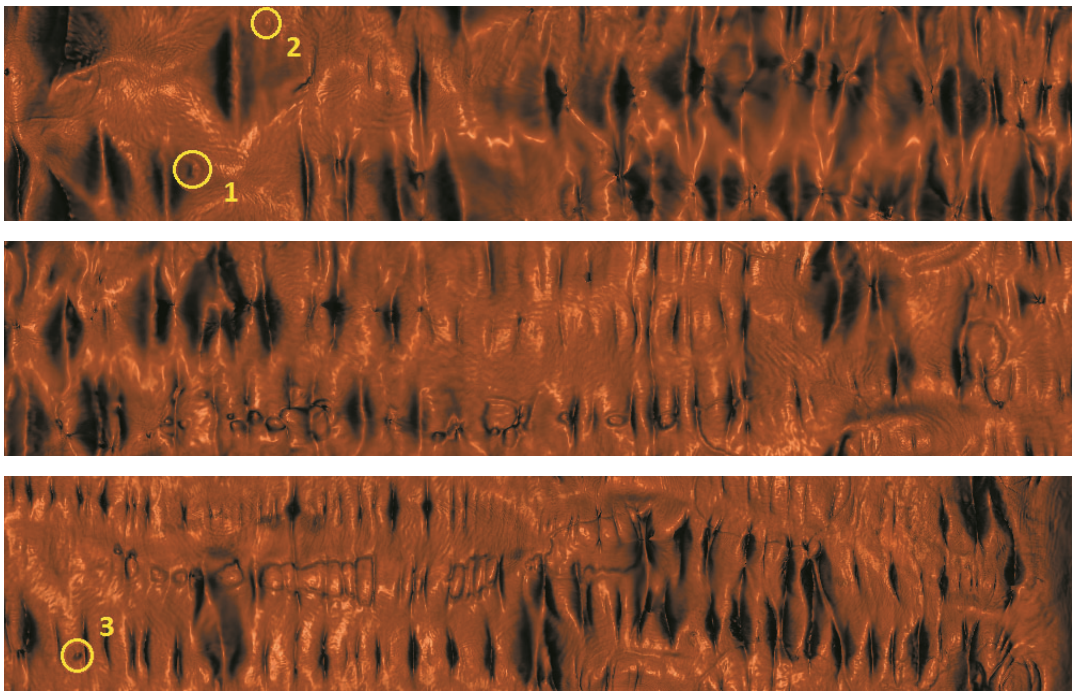

(a)

(b)

(c)

Figure 54: A flattened image for a whole colon dataset is shown in three images. The rectum of the colon is on the left of (a) and the colon stretches to the cecum, which is on the right of (c). The colonic polyps and the haustral folds are well preserved. Three polyps, 1 and 2 in (a) and 3 in (c) are shown within the yellow circles.

We compared the speed of our approach of handle detection and removal with a previous approach [59]. Using our approach, the average time for the entire process of handle detection and removal on the colon surfaces with around 55,000 faces was 2.8 secs. On the other hand, the previous approach took an average of 800 secs to detect and remove all the handles using the same colon surface. Thus, we have obtained more than two orders of magnitude gain in speed using our approach of noise removal. In total, there were 43 handles on the colon surface shown in Fig. 53. We tried our approach on four other colon

surfaces and all the handles in all cases were detected proving the accuracy and efficiency of our approach. We also verified the handle count obtained by our method with that obtained by the previous method [59] and the value matched in all cases.

6.5.4 Implementation and Results

Flat Colon Rendering: The result of our method is a colon surface flattened onto a 2D rectangle, which also results in polyps being flattened. The shape of the polyps is a good clue for polyp detection and hence the rendering of the flattened colon image is crucial for their detection. Volume rendering of flattened colons has been presented and suggested for use in VC navigation [59]. We perform the volume rendering of the flattened colon in the same way and obtain a high-quality image of the flattened colon. The volume rendered flattening result of a colon mesh model using our method is shown in Fig. 54. Since the colon is very long, we show the flattening result in three parts. The colon stretches from the rectum which is on the left of Fig. 54(a) to the cecum which is on the right of Fig. 54(c). We can clearly see how easy it is to examine the whole interior colon region using our method. Moreover, important features such as the polyps and the haustral folds are clearly visible and well preserved. We show the location of three polyps (1, 2 and 3) on the flattened colon surface, marked in yellow circles in Figs. 54(a) and (c). The resolution of the rendered image in Fig. 54 is 3000×200. The rendering was performed on a system equipped with an Intel Xeon E5620 CPU and NVIDIA GeForce GTX 480 graphics board.

Polyp 1 is a large polyp of size 6.1×9.6 mm and can directly be inspected in Fig. 54(a). However, polyp 2 of size 3.1×3.7 mm and polyp 3 of size 3.8×2.5 mm are relatively small and hard to recognize. Therefore, in a clinical application, the resolution should be at least four times higher than the one used in Fig. 54, such as shown in Fig. 55. The rendering using the GPU provides a real-time high-quality zoom-in functionality, which allows the physicians to interactively inspect suspicious regions. By having a flattened colon visualization, we are providing a better means of navigation so that no area of the colon is missed. This flattened colon visualization opens an additional option for the physician to improve the colon surface exploration.

We have also shown our results to a radiologist who was involved with the early conception of VC and has over ten years of experience in reading them. He noted that the flat rendering was realistic, and that the anatomical features such as folds, and especially significant polyps ($\geq$6 mm in diameter) are well preserved and easily noticeable (he had not been exposed to flattened rendering prior to viewing this work). In addition, we have cross-verified the location of the polyps on the flattened colon by checking with the VC and OC reports provided by the Walter Reed Army Medical Center. We plan to conduct in the near future a more comprehensive study with radiologists.

Implementation The pipeline was implemented in C++ in a Windows environment. The volumetric rendering was performed on the GPU using OpenGL and Cg. The colon data used in this work come from volumes with an approximate size of $512 \times 512 \times 400$ vox-

els. Preprocessing of the volumes includes electronic cleansing, segmentation, triangular mesh extraction, and skeleton extraction. The meshes obtained are very large (typically over 1.5 million faces) and are simplified to approximately 5% of their original size. We have successfully obtained flattening results for six different colon models. Apart from the flattening of the whole colon, we have also segmented the colon into three segments, namely ascending, transverse and descending segments. Thus, we have tested our colon flattening approach successfully with a total of 24 cases, including the segments and the whole colon surfaces. The whole process of colon flattening for an entire colon model with around 55,000 faces took an average of 23.93 sec, not including the time taken for the preprocessing of the colon. It took on average 12.38 sec to evaluate the heat diffusion metric using 50 eigenvalues and eigen functions and an average time of 11.55 sec to obtain the flattening using this heat diffusion metric.

6.5.5 Applications:

Our major focus is to achieve a robust colon flattening, thereby avoiding the time-consuming topological denoising step. Since the shape information is preserved in the flattened colon, we show its application for polyp visualization, especially in hidden regions such as behind the folds. We also show how the supine and prone colon registration pipeline becomes more robust by using our method. **P**olyp Visualization and Detection One of the important applications of colon flattening is to provide a better way for the physicians to visualize and even detect the polyps. Specifically, polyps behind haustral folds are hidden and missed during the VC fly through of a 3D model. The polyps are small protrusions or bumps on the colonic wall. By using our method, all the shapes on the colon surface are preserved even after flattening. Therefore, the polyps can be clearly seen as bumps and hence form an effective means of polyp visualization. Furthermore, the volume rendering of the flattened colon provides a realistic rendering of polyps. In addition, the physician can zoom-in at the suspicious regions to confirm the location of the polyps. Thus, even relatively small polyps can be seen, as shown by few examples in Fig. 55.

Fig. 55 shows a close up view of some of the polyps (protrusions) observed by navigating along the flattened colon surface. Fig. 55(a) shows a close up view of polyp 1 in Fig. 54(a), which is a large polyp. Fig. 55(b) shows a close up view of polyp 2 in Fig. 54(a) which is a relatively small polyp. Fig. 55(c) shows a close up view of polyp 3 in Fig. 54(c) that is hidden behind a fold (pointed to by the red arrow). It is difficult to find such polyps during navigation using a conventional VC system. However, when a flattened colon is available, even polyps hidden behind colonic folds can be observed, as seen in Fig. 55(c). Another example of a close up view of a polyp is shown in Fig. 47(b). These close up views help the physician to verify that the suspicious regions detected are indeed polyps and not some leftover stool. The shape of polyps can be identified and their sizes can be measured. Note that our technique does not provide an automatic method of polyp detection but rather makes it easy to locate, confirm, and visualize polyps, especially in areas which are oth-

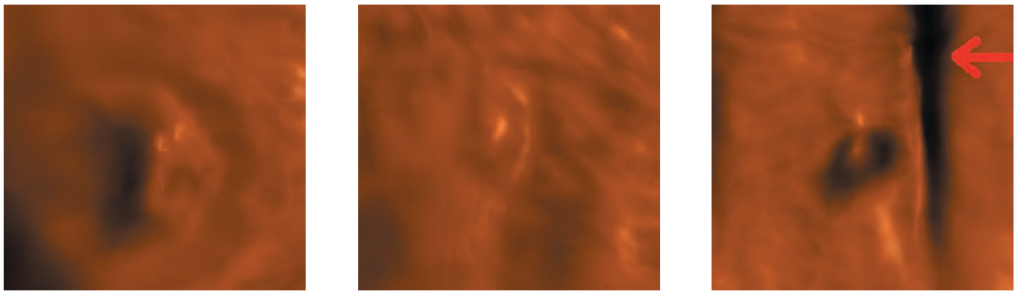

(a) (b) (c)

Figure 55: Close up view of the polyps (bumps on the colon wall). (a) Polyp 1 in Fig. 54(a); (b) Polyp 2 in Fig. 54(a); (c) Polyp 3 in Fig. 54(c), which is hidden behind a colonic fold indicated by the red arrow.

erwise hard to navigate. By performing size and shape analysis on the flat colon, we can detect the polyps automatically, which we plan to do in the future.

Colon Registration: Shape registration is very fundamental for shape analysis problems, especially for abnormality detection in medical applications. The colon deformation and the diverse shapes of polyps make it difficult to distinguish polyps from other non-threatening objects in the colon. Hence, for a VC procedure, CT scans of the abdomen are commonly acquired with the patient in both supine (facing up) and prone (facing down) positions to improve the visualization of the colon wall, reduce false positives, and improve sensitivity. Comparisons between the supine and prone colon surfaces can be facilitated by computerized registration between these scans.

Registration of supine and prone colon surfaces using quasi-conformal mapping has been described by Zeng et al. [150]. In their approach, a costly topological denoising step is performed on both supine and prone colon surfaces before the start of the registration pipeline. Using the same registration approach, we show the registration of noisy supine and prone colon surfaces. We use our colon flattening approach to obtain the rectangular maps of supine and prone colon surfaces with handles. By virtue of our method, the flattening is not affected by the handles. We then obtain the surface feature points on these supine and prone flattened maps. Finally, using these feature points as constraints, we register the supine to prone using quasi-conformal mapping steps [150]. Therefore, we improved the robustness of the supine and prone colon registration algorithm [150] by directly registering the supine and prone colon surfaces with handles, which otherwise was impossible without denoising.

We have analytically evaluated the quality of the registration by a distance measurement between corresponding features located on the registered colon surfaces [150]. Since our

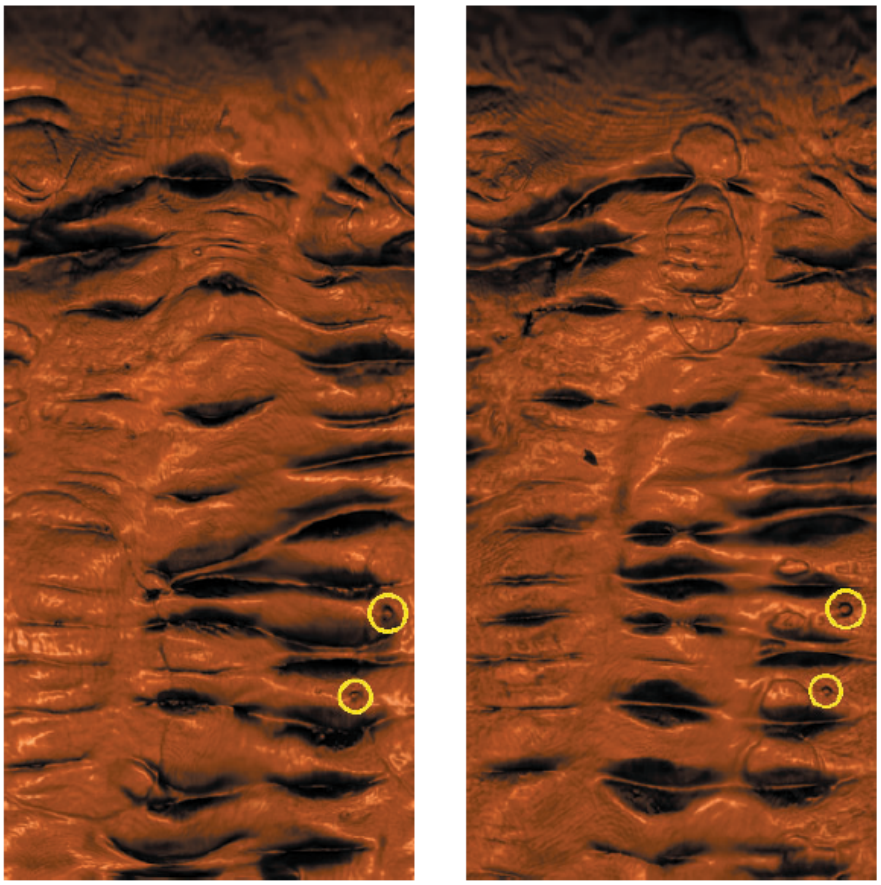

Figure 56: Registered flattened views of the ascending colon segments with handles of (a) supine and (b) prone colon surfaces. Two polyps found on (a) (shown in yellow circles) can be located on (b) (shown in yellow circles) at nearly the same position.

registration is in the 2D space using the flattened colon surfaces, a point in $\mathbb{R}^3$ on the original colon surface corresponds to a point in $\mathbb{R}^2$ on the registered surface. For two corresponding points (polyps or feature points used as constraints) on the supine and prone flattened colons, we compute the L^2 norm of their 2D coordinates with the width of the flattened images fixed to a unit length of 1. We also compute the 3D distance error by measuring the distance between the same two corresponding feature points on the supine and prone original colon surfaces (see [150] for details of the evaluation procedure). We have evaluated the registration using a total of 6 pairs on 2 datasets by considering 16 pairs of feature points. The average distance error is 0.0385 in $\mathbb{R}^2$ and 8.14 mm in $\mathbb{R}^3$, which is comparable to the error values of Zeng et al. [150]. Fig. 56 provides a visual

verification for supine-prone colon registration. Figs. 56(a) and (b) show the registered flattened views of the ascending colon segments of supine and prone colon surfaces with handles, respectively. Two polyps found on the flattened supine surface (yellow circles in Fig. 56(a)) can be located on the flattened prone surface (yellow circles in Fig. 56(b)) at nearly the same position. Moreover, the images of the registered segments in Fig. 56 show very good alignment of the supine and prone colon structures and a good correspondence between their features, such as folds and polyps.

7 Conclusion

In this dissertation, we reviewed the mathematical theories and algorithms of computational conformal geometry, then explored its applications in computer vision, wireless sensor network and medical imaging. One of the most powerful features of conformal geometry that it can build intrinsic mapping between 3D surface to 2D plane, thus solve complicated 3D problems by reduce the dimension of the problem. Another powerful feature is that conformal geometry can be used to design surface metrics, which often make the problems much easier under the new metric. In computer vision, we presented a method to changing the Riemannian metric on the target surface to a hyperbolic metric, so that the harmonic mapping is guaranteed to be a diffeomorphism under landmark constraints. The computational algorithms are based on the Ricci flow and nonlinear heat diffusion methods, it works for general topology surfaces with landmark constraints. In wireless sensor network, we show a myth in common understanding of the memoryless property of a random walk applied for protecting source location privacy in a wireless sensor network. We also proposed a simple algorithms to recover the location of the source in simple cases. We also develop a generic algorithm to reconstruct the source locations for various sources that have simple descriptions (e.g., k source locations, sources on a line segment, sources in a disk). This represents a new type of traffic analysis attack for invading sensor data location privacy and essentially re-opens the problem for further examination. In medical imaging, we proposes a new colon flattening algorithm that is efficient, shape-preserving, and robust to topological noise. Our method is shape-preserving and the shape of the polyps are well preserved. The flattened colon also provides an efficient way to enhance the navigation and inspection in virtual colonoscopy.

In this dissertation, we have demonstrated the power of computational conformal geometry, but the research on computational conformal geometry is far from complete. Hot topics include finding optimal quasi-conformal and area-preservation mappings between surfaces. In physical world, most surface deformations can be rigorously modeled as quasi-conformal maps, this is of great importance in computer vision and medical imaging field. The local deformation is characterized by a complex-value function, Beltrami coefficient, which describes the deviation from conformality of the deformation at each point. Effective algorithm to solve the quasi-conformal map from the Beltrami coefficient is under extensive

research. Another emerging topic is the area-preservation mapping/fattening method using the optimal mass transport technique, based on the Monge-Brenier theory. Area-preserving mapping can serve as a powerful tool for a broad range of applications in visualization and graphics, especially for medical imaging.

References

[1] Brain surface conformal parameterization with the slit mapping. *Biomedical Imaging: From Nano to Macro, 2008. ISBI 2008. 5th IEEE International Symposium on*, pages 448 – 451.

[2] L. Ahlfors. *Lectures in Quasiconformal Mappings*. Van Nostrand Reinhold, New York, 1966.

[3] M. Alexa. Recent advances in mesh morphing. *Comput. Graph. Forum*, 21(2):173–196, 2002.

[4] B. Allen, B. Curless, and Z. Popović. The space of human body shapes: reconstruction and parameterization from range scans. *ACM Trans. Graph.*, 22(3):587–594, Jul 2003.

[5] S. Angenent, S. Haker, A. Tannenbaum, and R. Kikinis. Conformal geometry and brain flattening. In *Med. Image Comput. Comput.-Assist. Intervention*, pages 271–278, 1999.

[6] O. K.-C. Au, C.-L. Tai, D. Cohen-Or, Y. Zheng, and H. Fu. Electors voting for fast automatic shape correspondence. *Comput. Graph. Forum*, 29(2):645–654, 2010.

[7] E. Balogh, E. Sorantin, L. G. Nyul, K. Palagyi, A. Kuba, G. Werkgartner, and E. Spuller. Colon unraveling based on electronic field: Recent progress and future work. *Proceedings SPIE*, 4681:713–721, 2002.

[8] A. V. Bartrol, R. Wegenkittl, A. Knig, E. Grller, and E. Sorantin. Virtual colon flattening. *VisSym Joint Eurographics - IEEE TCVG Symposium on Visualization*, pages 127–136, 2001.

[9] A. V. Bartrolí, R. Wegenkittl, A. König, and E. Gröller. Nonlinear virtual colon unfolding. *IEEE Visualization*, pages 411–420, 2001.

[10] M. Belkin and P. Niyogi. Laplacian eigenmaps for dimensionality reduction and data representation. *Neural Computing*, 15(6):1373–1396, June 2003.

[11] P. Besl and N. D. McKay. A method for registration of 3-d shapes. *Pattern Analysis and Machine Intelligence, IEEE Transactions on*, 14(2):239–256, 1992.

[12] P. J. Besl and N. D. Mckay. A Method for Registration of 3D Shapes. *IEEE Transactions on Pattern Analysis and Machine Intelligence*, 14(2), Feb. 1992.

[13] C. Bishop. The riemann mapping theorem. http://www.math.sunysb.edu/ bishop/classes/math401.F09/t.pdf.

[14] D. M. Boyer, Y. Lipman, E. S. Clair, J. Puente, B. A. Patel, T. Funkhouser, J. Jernvall, , and I. Daubechies. Algorithms to automatically quantify the geometric similarity of anatomical surfaces. *PNAS*, 2011.

[15] S. C. Brenner and L. R. Scott. *The Mathematical Theory of Finite Element Methods*. Springer, 2002.

[16] A. Bronstein, M. Bronstein, and R. Kimmel. *Numerical Geometry of Non-Rigid Shapes*. 2008.

[17] A. M. Bronstein, M. M. Bronstein, and R. Kimmel. Generalized multidimensional scaling: a framework for isometry-invariant partial surface matching. *Proc. Natl. Acad. Sci. U.S.A.*, 103(5):1168–1172, Jan 2006.

[18] A. M. Bronstein, M. M. Bronstein, R. Kimmel, M. Mahmoudi, and G. Sapiro. A Gromov-Hausdorff framework with diffusion geometry for topologically-robust non-rigid shape matching. *International Journal of Computer Vision*, 89(2-3):266–286, Sept. 2010.

[19] M. M. Bronstein and A. M. Bronstein. Shape recognition with spectral distances. *IEEE Trans Pattern Anal Mach Intell*, 33(5):1065–1071, May 2011.

[20] B. J. Brown and S. Rusinkiewicz. Global non-rigid alignment of 3-d scans. In *ACM SIGGRAPH 2007 papers*, SIGGRAPH '07, 2007.

[21] M. M. Center, A. Jemal, R. A. Smith, and E. Ward. Worldwide variations in colorectal cancer. *CA: A Cancer Journal for Clinicians*, 59(6):366–378, November/December 2009.

[22] D. L. Chaum. Untraceable electronic mail, return addresses, and digital pseudonyms. *Commun. ACM*, 24(2):84–90, 1981.

[23] I. Chavel. *Riemannian Geometry: A Modern Introduction*. Cambridge University Press, 2006.

[24] S.-S. Chern. An elementary proof of the existence of isothermal parameters on a surface. In *Proc. of AMS*, volume 6, pages 771–782, 1955.

[25] S.-S. Chern. An elementary proof of the existence of isothermal parameters on a surface. In *Proc. Amer. Math. Soc.*, pages 771–782, 1955.

[26] B. Chow and F. Luo. Combinatorial ricci flows on surfaces. *Journal Differential Geometry*, 63(1):97–129, 2003.

[27] B. Chow and F. Luo. Combinatorial ricci flows on surfaces. *Journal Differential Geometry*, 63(1):97–129, 2003.

[28] R. R. Coifman, S. Lafon, A. B. Lee, M. Maggioni, F. Warner, and S. Zucker. Geometric diffusions as a tool for harmonic analysis and structure definition of data: Diffusion maps. *Proceedings of the National Academy of Sciences*, pages 7426–7431, 2005.

[29] T. A. Davis. A column pre-ordering strategy for the unsymmetric-pattern multifrontal method. *ACM Trans. Math. Softw.*, 30(2):165–195, 2004.

[30] C. de Verdiere Yves. Un principe variationnel pour les empilements de cercles. *Invent. Math.*, 104(3):655–669, 1991.

[31] T. K. Dey, K. Li, J. Sun, and D. Cohen-Steiner. Computing geometry-aware handle and tunnel loops in 3D models. *ACM Transactions on Graphics*, 27(3):45:1–45:9, Aug. 2008.

[32] M. P. do Carmo. *Differential Geometry of Curves and Surfaces*. Prentice Hall, 1976.

[33] M. P. do Carmo. *Differential Geometry of Curves and Surfaces*. Prentice Hall, 1976.

[34] M. P. do Carmo. *Riemannian Geometry*. Prentice Hall, 1992.

[35] P. G. Doyle and J. L. Snell. *Random Walks and Electric Networks*. The Mathematical Association of America, 1984.

[36] A. Dubrovina and R. Kimmel. Approximately isometric shape correspondence by matching pointwise spectral features and global geodesic structures. *Advances in Adaptive Data Analysis*, 3(1-2):203–228, 2011.

[37] M. Eck, T. DeRose, T. Duchamp, H. Hoppe, M. Lounsbery, and W. Stuetzle. Multiresolution analysis of arbitrary meshes. In *Proceedings of the 22Nd Annual Conference on Computer Graphics and Interactive Techniques*, SIGGRAPH '95, pages 173–182, 1995.

[38] H. Edelsbrunner and J. L. Harer. *Computational Topology*. American Mathematical Society, 2009.

[39] H. M. Farkas and I. Kra. *Riemann Surfaces*. Springer, 2004.

[40] B. Fischl, M. I. Sereno, and A. M. Dale. Cortical surface-based analysis II: Inflation, flattening, and a surface-based coordinate system. *NeuroImage*, 9(2):195 – 207, 1999.

[41] J. Garnett and D. Marshall. *Harmonc Measure*. Cambridge University Press, 2005.

[42] D. Glickenstein. A combinatorial yamabe flow in three dimensions. *Topology*, 44(4):791–808, 2005.

[43] A. Golovinskiy and T. Funkhouser. Consistent segmentation of 3d models. In *Computers & Graphics, IEEE SMI 2009 proceedings, (33)3*, pages 262–269, 2009.

[44] X. Gu, Y. He, and H. Qin. Manifold splines. *Graphical Models*, 68(3):237–254, 2006.

[45] X. Gu, Y. Wang, T. F. Chan, P. M. Thompson, and S.-T. Yau. Genus zero surface conformal mapping and its application to brain surface mapping. *IEEE Trans. Med. Imag.*, 23(8):949–958, Aug. 2004.

[46] X. Gu, Y. Wang, and S. tung Yau. Multiresolution computation of conformal structures of surfaces. *Journal of Systemics, Cybernetics and Informatics*, 1:2004, 1996.

[47] X. Gu and S.-T. Yau. Global conformal parameterization. In *Symposium on Geometry Processing*, pages 127–137, 2003.

[48] X. Gu and S.-T. Yau. Global conformal surface parameterization. In *SGP '03: Proceedings of the 2003 Eurographics/ACM SIGGRAPH symposium on Geometry processing*, pages 127–137, Aire-la-Ville, Switzerland, Switzerland, 2003. Eurographics Association.

[49] X. Gu and S.-T. Yau. Global conformal surface parameterization. In *Proc. Eurographics/SIGGRAPH Symp. Geometry Processing*, pages 127–137. Eurographics Association, 2003.

[50] X. D. Gu and S.-T. Yau. *Computational Conformal Geometry*. Higher Education Press, first edition, 2008.

[51] X. D. Gu and S.-T. Yau. *Computational conformal geometry*, volume 3. International Press Somerville, 2008.

[52] I. Guskov and Z. J. Wood. Topological noise removal. *Graphics Interface*, pages 19–26, 2001.

[53] S. Haker, S. Angenent, and R. Kikinis. Nondistorting flattening maps and the 3D visualization of colon CT images. *IEEE Transactions on Medical Imaging*, 19:665–670, July 2000.

[54] R. S. Hamilton. The ricci flow on surfaces. *Mathematics and general relativity*, 71:237–262, 1988.

[55] A. Hatcher. *Algebraic Topology*. Cambridge University Press, 2002.

[56] Y. He, K. Wang, H. Wang, X. Gu, and H. Qin. Manifold t-spline. In *In Proceedings of Geometric Modeling and Processing*, pages 409–422, 2006.

[57] A. Hirani. Discrete exterior calculus. 2003.

[58] L. Hong, S. Muraki, A. E. Kaufman, D. Bartz, and T. He. Virtual voyage: interactive navigation in the human colon. *SIGGRAPH*, pages 27–34, 1997.

[59] W. Hong, X. Gu, F. Qiu, M. Jin, and A. Kaufman. Conformal virtual colon flattening. *ACM Symposium on Solid and Physical Modeling*, pages 85–93, 2006.

[60] W. Hong, F. Qiu, and A. Kaufman. A pipeline for computer aided polyp detection. *IEEE Transactions on Visualization and Computer Graphics*, 12(5):861–868, Sept. 2006.

[61] M. Horner, L. Ries, M. Krapcho, N. Neyman, R. Aminou, N. Howlader, S. Altekruse, E. Feuer, L. Huang, A. Mariotto, B. Miller, D. Lewis, M. Eisner, D. Stinchcomb, and B. Edwards (eds). Seer Cancer Statistics Review. 1975-2006.

[62] Q.-X. Huang, B. Adams, M. Wicke, and L. J. Guibas. Non-rigid registration under isometric deformations. In *Proceedings of the Symposium on Geometry Processing*, SGP 08, pages 1449–1457, 2008.

[63] V. Jain, H. Zhang, and O. van Kaick. Non-rigid spectral correspondence of triangle meshes, 2006.

[64] M. Jin, J. Kim, and X. D. Gu. Discrete surface Ricci flow: Theory and applications. *Proceedings of the 12th IMA International Conference on Mathematics of Surfaces XII*, pages 209–232, 2007.

[65] M. Jin, J. Kim, F. Luo, and X. Gu. Discrete surface Ricci flow. *IEEE Transactions on Visualization and Computer Graphics*, 14(5):1030–1043, 2008.

[66] M. Jin, Y. Wang, S.-T. Yau, and X. Gu. Optimal global conformal surface parameterization. In *IEEE Visualization 2004*, pages 267–274, 2004.

[67] C. D. Johnson and A. H. Dachman. CT colography: The next colon screening examination. *Radiology*, 216(2):331–341, 2000.

[68] A. Joshi, D. Shattuck, P. Thompson, and R. Leahy. Surface-constrained volumetric brain registration using harmonic mappings. *IEEE Trans. Med. Imag.*, 26(12):1657–1669, Dec. 2007.

[69] T. Ju, Q.-Y. Zhou, and S.-M. Hu. Editing the topology of 3D models by sketching. *ACM Transactions on Graphics*, 26(3):42, July 2007.

[70] O. V. Kaick, H. Zhang, G. Hamarneh, and D. Cohen-or. A survey on shape correspondence, 2011.

[71] S. Kakutani. On brownian motion in n-space. *Proc. Imp. Acad. Tokyo*, 20(9):648–652, 1944.

[72] P. Kamat, Y. Zhang, W. Trappe, and C. Ozturk. Enhancing source-location privacy in sensor network routing. In *Proceedings of the 25th IEEE International Conference on Distributed Computing Systems*, ICDCS '05, pages 599–608, 2005.

[73] V. G. Kim, Y. Lipman, and T. Funkhouser. Blended intrinsic maps. In *ACM SIGGRAPH 2011*, SIGGRAPH '11, pages 79:1–79:12, 2011.

[74] P. M. Knupp. Matrix norms and the condition number: A general framework to improve mesh quality via node-movement. *Eighth International Meshing Roundtable*, pages 13–22, 1999.

[75] V. Kraevoy and A. Sheffer. Cross-parameterization and compatible remeshing of 3d models. *ACM Trans. Graph.*, 23(3):861–869, Aug 2004.

[76] E. Kreyszig. *Differential Geometry*. Dover, New York, 1991.

[77] Y. kun Lai, M. Jin, X. Xie, Y. He, S. min Hu, and X. Gu. Metric-driven rosy field design and remeshing. *IEEE Transactions on Visualization and Computer Graphics*, 16(1):95–108, 2010.

[78] S. Kurtek, E. Klassen, J. C. Gore, Z. Ding, and A. Srivastava. Elastic Geodesic Paths in Shape Space of Parametrized Surfaces. *IEEE Trans Pattern Anal Mach Intell*, Nov 2011.

[79] S. Lafon. *Diffusion maps and geometric harmonics*. PhD thesis, Yale University, May 2004.

[80] G. Lawler. *Conformally Invariant Processes in the Plane*. Amer Mathematical Society, 2005.

[81] G. F. Lawler. Conformally invariant processes in the plane. *Mathematical Surveys and Monographs*, 114(2), 2008.

[82] M. Leif. *Stability, Riemann Surfaces, Conformal Mappings*. Ventus Publishing, 2010.

[83] N. Li, N. Zhang, S. K. Das, and B. Thuraisingham. Privacy preservation in wireless sensor networks: A state-of-the-art survey. *Ad Hoc Netw.*, 7:1501–1514, November 2009.

[84] Y. Li and J. Ren. Preserving source-location privacy in wireless sensor networks. In *Proceedings of the 6th Annual IEEE communications society conference on Sensor, Mesh and Ad Hoc Communications and Networks*, SECON'09, pages 493–501, 2009.

[85] S. Lim, H.-J. Lee, and B.-S. Shin. Surface reconstruction for efficient colon unfolding. *International Conference on Geometric Modeling and Processing*, pages 623–629, 2006.

[86] H. Ling and K. Okada. Diffusion distance for histogram comparison. *Proceedings of Computer Vision and Pattern Recognition*, 1:246–253, 2006.

[87] N. Litke, M. Droske, M. Rumpf, and P. Schröder. An image processing approach to surface matching. SGP '05, 2005.

[88] Y.-S. Liu, Q. Li, G.-Q. Zheng, K. Ramani, and W. Benjamin. Using diffusion distances for flexible molecular shape comparison. *BMC Bioinformatics*, 11:480, 2010.

[89] L. Lovasz. Random walks on graphs: A survey. *Bolyai Soc. Math. Stud.*, 2:353–397, 1996.

[90] F. Luo. Combinatorial yamabe flow on surfaces. *Commun. Contemp. Math.*, 6(5):765–780, 2004.

[91] F. Luo, X. Gu, and J. Dai. *Variational Principles for Discrete Surfaces*. Advanced Lectures in Mathematics. High Education Press and International Press, 2007.

[92] X. Luo, X. Ji, and M.-S. Park. Location privacy against traffic analysis attacks in wireless sensor networks. In *2010 International Conference on Information Science and Applications*, pages 1–6. Ieee, February 2010.

[93] M. Mahmoudi and G. Sapiro. Three-dimensional point cloud recognition via distributions of geometric distances. *Graphical Models*, 71(1):22–31, Jan. 2009.

[94] D. Mateus, R. Horaud, D. Knossow, F. Cuzzolin, and E. Boyer. Articulated shape matching using laplacian eigenfunctions and unsupervised point registration. In *Computer Vision and Pattern Recognition, 2008. CVPR 2008. IEEE Conference on*, pages 1–8, 2008.

[95] K. Mehta, D. Liu, and M. Wright. Protecting location privacy in sensor networks against a global eavesdropper. *IEEE Trans. Mob. Comput.*, 11(2):320–336, 2012.

[96] F. Mémoli. Spectral Gromov-Wasserstein distances for shape matching. In *Computer Vision Workshops (ICCV Workshops), 2009 IEEE 12th International Conference on*, pages 256–263. IEEE, 2009.

[97] F. Mémoli. Spectral Gromov-Wasserstein distances for shape matching. *Proceedings of NORDIA*, 2009.

[98] Z. Nehari. *Conformal Mapping*. New York:Dover, 1982.

[99] M. Ovsjanikov, A. M. Bronstein, L. J. Guibas, and M. M. Bronstein. Shape google: a computer vision approach to invariant shape retrieval. *Proceedings of NORDIA*, 2009.

[100] M. Ovsjanikov, Q. Mrigot, F. Mmoli, and L. J. Guibas. One point isometric matching with the heat kernel. *Comput. Graph. Forum*, 29(5):1555–1564, 2010.

[101] C. Ozturk, Y. Zhang, and W. Trappe. Source-location privacy in energy-constrained sensor network routing. In *Proceedings of the 2nd ACM workshop on Security of ad hoc and sensor networks*, SASN '04, pages 88–93, 2004.

[102] D. S. Paik, C. F. Beaulieu, R. B. J. Jeffrey, C. A. Karadi, and S. Napel. Visualization modes for CT colonography using cylindrical and planar map projections. *Journal of Computer Assisted Tomography*, 24:179–188, 2000.

[103] D. Pantazis, A. Joshi, J. Jiang, D. W. Shattuck, L. E. Bernstein, H. Damasio, and R. M. Leahy. Comparison of landmark-based and automatic methods for cortical surface registration. *Neuroimage*, 49(3):2479–2493, Feb 2010.

[104] M. Pauly, N. J. Mitra, J. Giesen, M. Gross, and L. J. Guibas. Example-based 3d scan completion. In *Proceedings of the third Eurographics symposium on Geometry processing*, SGP '05, 2005.

[105] P. Petersen. *Riemannian Geometry*. Springer Verlag, 1997.

[106] U. Pinkall, S. D. Juni, and K. Polthier. Computing discrete minimal surfaces and their conjugates. *Experimental Mathematics*, 2:15–36, 1993.

[107] E. Praun, W. Sweldens, and P. Schröder. Consistent mesh parameterizations. In *Proceedings of the 28th annual conference on Computer graphics and interactive techniques*, pages 179–184, 2001.

[108] Y. G. Reshetnyak. Two-dimensional manifolds of bounded curvature. In Y. G. Reshetnyak, editor, *Geometry IV*, Encyclopedia of Mathematical Sciences. Springer, 1993.

[109] G. Rong, Y. Liu, W. Wang, X. Yin, X. D. Gu, and X. Guo. Gpu-assisted computation of centroidal voronoi tessellation. *IEEE Transactions on Visualization and Computer Graphics, 2011*, 17:345 – 356.

[110] W. Rudin. *Principles of Mathematical Analysis*. McGraw-Hill, 1976.

[111] R. M. Rustamov. Laplace-Beltrami eigenfunctions for deformation invariant shape representation. *Eurographics Symposium on Geometry Processing*, pages 225–233, 2007.

[112] R. Sarkar, F. Luo, X. Yin, X. D. Gu, and J. Gao. Greedy routing with guaranteed delivery using ricci flows. In *In Proc. of the 8th International Symposium on Information Processing in Sensor Networks (IPSN09*, 2009.

[113] R. Sarkar, X. Yin, J. Gao, F. Luo, and X. D. Gu. Greedy routing with guaranteed delivery using ricci flows. In *Proc. of the 8th International Symposium on Information Processing in Sensor Networks (IPSN'09)*, pages 97–108, April 2009.

[114] R. Schoen. Conformal deformation of a riemannian metric to constant scalar curvature. *J. Differential Geom.*, 20(2):479–495, 1984.

[115] R. Schoen and S.-T. Yau. *Lectures on Harmonic Maps*. International Press, 1997.

[116] R. M. Schoen and S.-T. Yau. Lectures on harmonic maps. *International Press, 1997, Mathematics*.

[117] J. Schreiner, A. Asirvatham, E. Praun, and H. Hoppe. Inter-surface mapping. ACM SIGGRAPH, pages 870–877, 2004.

[118] J. A. Sethian. A fast marching level set method for monotonically advancing fronts. *Proc. Natl. Acad. Sci. U.S.A.*, 93:1591–1595, 1996.

[119] A. Sharma and R. Horaud. Shape matching based on diffusion embedding and on mutual isometric consistency. In *Computer Vision and Pattern Recognition Workshops (CVPRW), 2010 IEEE Computer Society Conference on*, pages 29–36, 2010.

[120] J. Shi, P. M. Thompson, B. Gutman, and Y. Wang. Surface fluid registration of conformal representation: Application to detect disease burden and genetic influence on hippocampus. *NeuroImage*, 2013, In Press.

[121] A. F. S.P. Novikov. *Basic elements of differential geometry and topology*. Springer, 1990.

[122] M. Spivak. *Calculus On Manifolds: A Modern Approach To Classical Theorems Of Advanced Calculus*. Westview Press, 1971.

[123] B. Springborn, P. Schröder, and U. Pinkall. Conformal equivalence of triangle meshes. *ACM Transactions on Graphics*, 27(3):77:1–77:11, Aug. 2008.

[124] M. Styner, I. Oguz, S. Xu, C. Brechbhler, D. Pantazis, J. Levitt, M. Shenton, and G. Gerig. Framework for the statistical shape analysis of brain structures using spharm-pdm. *Proceedings of Image Computing and Computer Assisted Intervention Open Science Workshop*, 2006.

[125] J. Sun, M. Ovsjanikov, and L. Guibas. A concise and provably informative multi-scale signature based on heat diffusion. *Symposium on Geometry Processing*, pages 1383–1392, 2009.

[126] P. F. Syverson, D. M. Goldschlag, and M. G. Reed. Anonymous connections and onion routing. *IEEE Journal on Selected Areas in Communications*, 16(4):482–494, 1997.

[127] P. F. Syverson, M. G. Reed, and D. M. Goldschlag. Onion routing access configurations. In *DISCEX 2000: Proceedings of DARPA Information Survivability Conference and Exposition*, pages 34–40, January 2000.

[128] M. E. Taylor. *Partial differential equations. I. , Basic theory*. Applied mathematical sciences. Springer, 2011.

[129] A. Tevs, M. Bokeloh, M. Wand, A. Schilling, and H. P. Seidel. Isometric registration of ambiguous and partial data. In *CVPR 2009.*, pages 1185–1192, 2009.

[130] P. M. Thompson, M. I. Miller, J. T. Ratnanther, R. A. Poldrack, and T. E. Nichols, editors. *NeuroImage, Special Issue on Mathematics in Brain Imaging*, volume 23. Elsevier, 2004.

[131] P. M. Thompson and A. W. Toga. A surface-based technique for warping 3-dimensional images of the brain. *IEEE Trans. Med. Imag.*, 15(4):1–16, 1996.

[132] W. P. Thurston. *Geometry and Topology of Three-Manifolds*. Princeton lecture notes, 1976.

[133] Y. Tong, P. Alliez, D. Cohen-Steiner, and M. Desbrun. Designing quadrangulations with discrete harmonic forms. *Eurographics Symposium on Geometry Processing*, pages 201–210, 2006.

[134] W. Trappe and L. C. Washington. *Introduction to Cryptography with Coding Theory*. Prentice Hall, 2002.

[135] N. S. Trudinger. Remarks concerning the conformal deformation of riemannian structures on compact manifolds. *Ann. Scuola Norm. Sup. Pisa*, 22(2):265–274, 1968.

[136] J. N. Tsitsiklis. Efficient algorithms for globally optimal trajectories. *Automatic Control, IEEE Transactions on*, 40(9):1528 –1538, sep 1995.

[137] C. Voisin and L. Schneps. *Hodge Theory and Complex Algebraic Geometry*. Cambridge University Press, 2008.

[138] G. Wang, S. B. Dave, B. P. Brown, Z. Zhang, E. G. Mcfarland, J. W. Haller, and M. W. Vannier. Colon unraveling based on electrical field: Recent progress and future work. *Proceedings SPIE*, 3660:125–132, 1999.

[139] G. Wang, E. G. Mcfarland, B. P. Brown, and M. W. Vannier. GI tract unraveling with curved cross section. *IEEE Transactions on Medical Imaging*, 17:318–322, 1998.

[140] G. Wang and M. W. Vannier. GI tract unraveling by spiral CT. *Proceedings SPIE*, 2434:307–315, 1995.

[141] Y. Wang, W. Dai, X. Gu, T. F. Chan, A. W. Toga, and P. M. Thompson. Studying brain morphology using Teichmüller space theory. In *ICCV*, pages 2365–2372, 2009.

[142] Y. Wang, X. Gu, T. F. Chan, P. M. Thompson, and S.-T. Yau. Conformal slit mapping and its applications to brain surface parameterization. *MICCAI*, pages 585–593, 2008.

[143] Y. Wang, X. Gu, and S.-T. Yau. Surface segmentation using global conformal structure. *Communications in Information and Systems*, 4(2):165–180, 2005.

[144] Y. Wang, M. Gupta, S. Zhang, S. Wang, X. Gu, D. Samaras, and P. Huang. High resolution tracking of non-rigid motion of densely sampled 3D data using harmonic maps. *Int. J. Comput. Vision*, 76(3):283–300, Mar. 2008.

[145] Y. Wang, J. Shi, X. Yin, X. Gu, T. F. Chan, S. T. Yau, A. W. Toga, and P. M. Thompson. Brain surface conformal parameterization with the Ricci flow. *IEEE Trans Med Imaging*, 31(2):251–264, Feb 2012.

[146] Y. Wang, L. Yuan, J. Shi, A. Greve, J. Ye, A. W. Toga, A. L. Reiss, and P. M. Thompson. Applying tensor-based morphometry to parametric surfaces can improve MRI-based disease diagnosis. *Neuroimage*, 74:209–230, Jul 2013.

[147] Y. Xi, L. Schwiebert, and W. Shi. Preserving source location privacy in monitoring-based wireless sensor networks. *Proceedings 20th IEEE IPDPS*, 06:1–8, 2006.

[148] Y.-L. Yang, J. Kim, F. Luo, S.-M. Hu, and X. Gu. Optimal surface parameterization using inverse curvature map. *IEEE Transactions on Visualization and Computer Graphics*, 14(5):1054–1066, Sep 2008.

[149] X. Yin, J. Dai, S.-T. Yau, and X. Gu. Slit map: Conformal parameterization for multiply connected surfaces. *Geometric Modeling and Processing*, pages 410–422, 2008.

[150] W. Zeng, J. Marino, K. Chaitanya Gurijala, X. Gu, and A. Kaufman. Supine and prone colon registration using quasi-conformal mapping. *IEEE Transactions on Visualization and Computer Graphics*, 16(6):1348–1357, Nov. 2010.

[151] W. Zeng, D. Samaras, and X. Gu. Ricci flow for 3d shape analysis. *IEEE TPAMI.*, 32:662–677, 2010.

[152] W. Zeng, X. Yin, Y. Zeng, Y. Lai, X. Gu, and D. Samaras. 3d face matching and registration based on hyperbolic ricci flow. In *CVPR 3D Face Processing Workshop*, 2008.

[153] Y. Zeng, C. Wang, Y. Wang, X. Gu, D. Samaras, and N. Paragios. Dense non-rigid surface registration using high-order graph matching. In *Computer Vision and Pattern Recognition (CVPR), 2010 IEEE Conference on*, pages 382–389, 2010.

[154] D. Zhang and M. Hebert. Harmonic maps and their applications in surface matching. In *Computer Vision and Pattern Recognition, 1999. IEEE Computer Society Conference on.*, volume 2, 1999.

[155] Q.-Y. Zhou, T. Ju, and S.-M. Hu. Topology repair of solid models using skeletons. *IEEE Transactions on Visualization and Computer Graphics*, 13(4):675–685, July 2007.

[156] L. Zhu, S. Haker, and A. Tannenbaum. Flattening maps for the visualization of multibranched vessels. *International Conference Image Processing*, 24:945–948, 2005.